

1982

Photoionization efficiency studies of some simple inorganic molecules

Steven Howard Linn
Iowa State University

Follow this and additional works at: <https://lib.dr.iastate.edu/rtd>

 Part of the [Physical Chemistry Commons](#)

Recommended Citation

Linn, Steven Howard, "Photoionization efficiency studies of some simple inorganic molecules " (1982). *Retrospective Theses and Dissertations*. 8362.
<https://lib.dr.iastate.edu/rtd/8362>

This Dissertation is brought to you for free and open access by the Iowa State University Capstones, Theses and Dissertations at Iowa State University Digital Repository. It has been accepted for inclusion in Retrospective Theses and Dissertations by an authorized administrator of Iowa State University Digital Repository. For more information, please contact digirep@iastate.edu.

INFORMATION TO USERS

This reproduction was made from a copy of a document sent to us for microfilming. While the most advanced technology has been used to photograph and reproduce this document, the quality of the reproduction is heavily dependent upon the quality of the material submitted.

The following explanation of techniques is provided to help clarify markings or notations which may appear on this reproduction.

1. The sign or "target" for pages apparently lacking from the document photographed is "Missing Page(s)". If it was possible to obtain the missing page(s) or section, they are spliced into the film along with adjacent pages. This may have necessitated cutting through an image and duplicating adjacent pages to assure complete continuity.
2. When an image on the film is obliterated with a round black mark, it is an indication of either blurred copy because of movement during exposure, duplicate copy, or copyrighted materials that should not have been filmed. For blurred pages, a good image of the page can be found in the adjacent frame. If copyrighted materials were deleted, a target note will appear listing the pages in the adjacent frame.
3. When a map, drawing or chart, etc., is part of the material being photographed, a definite method of "sectioning" the material has been followed. It is customary to begin filming at the upper left hand corner of a large sheet and to continue from left to right in equal sections with small overlaps. If necessary, sectioning is continued again—beginning below the first row and continuing on until complete.
4. For illustrations that cannot be satisfactorily reproduced by xerographic means, photographic prints can be purchased at additional cost and inserted into your xerographic copy. These prints are available upon request from the Dissertations Customer Services Department.
5. Some pages in any document may have indistinct print. In all cases the best available copy has been filmed.

**University
Microfilms
International**
300 N. Zeeb Road
Ann Arbor, MI 48106

8307765

Linn, Steven Howard

PHOTOIONIZATION EFFICIENCY STUDIES OF SOME SIMPLE
INORGANIC MOLECULES

Iowa State University

PH.D. 1982

University
Microfilms
International

300 N. Zeeb Road, Ann Arbor, MI 48106

Photoionization efficiency studies
of some simple inorganic molecules

by

Steven Howard Linn

A Dissertation Submitted to the
Graduate Faculty in Partial Fulfillment of the
Requirements for the Degree of
DOCTOR OF PHILOSOPHY

Major: Chemistry

Approved:

Signature was redacted for privacy.

In Charge of Major Work

Signature was redacted for privacy.

For the Major Department

Signature was redacted for privacy.

For the Graduate College

Members of the Committee:

Signature was redacted for privacy.

Iowa State University
Ames, Iowa

1982

TABLE OF CONTENTS

	Page
GENERAL INTRODUCTION	1
EXPERIMENTAL APPARATUS	7
GENERAL THEORY	18
SECTION I. MOLECULAR BEAM PHOTOIONIZATION STUDY OF HgCl_2	28
ABSTRACT	29
INTRODUCTION	30
EXPERIMENTAL	33
RESULTS AND DISCUSSION	35
SUMMARY AND CONCLUSION	52
REFERENCES	54
SECTION II. MOLECULAR BEAM PHOTOIONIZATION STUDY OF HgBr_2 and HgI_2	58
ABSTRACT	59
INTRODUCTION	60
DESIGNATION OF ELECTRONIC STATES FOR HgX_2^+	61
EXPERIMENTAL	62
RESULTS AND DATA ANALYSIS	66
DISCUSSION	89
SUMMARY	104
REFERENCES	105

	Page
SECTION III. PHOTOIONIZATION OF CO ₂ , N ₂ O DIMERS AND CLUSTERS	109
ABSTRACT	110
INTRODUCTION	111
EXPERIMENTAL	113
RESULTS AND DISCUSSION	115
REFERENCES	130
SECTION IV. MOLECULAR BEAM PHOTOIONIZATION STUDY OF CO, N ₂ , AND NO DIMERS AND CLUSTERS	134
ABSTRACT	135
INTRODUCTION	136
EXPERIMENTAL	138
RESULTS AND DISCUSSION	140
REFERENCES	157
SECTION V. A STUDY OF THE ION-MOLECULE HALF REACTIONS O ₂ ⁺ ($\alpha^4\Pi_u, v$)... (O ₂) _m + O ₂ ⁺ _{m+1} + 0, m = 1, 2, OR 3, USING THE MOLECULAR BEAM PHOTOIONIZATION METHOD	160
ABSTRACT	161
INTRODUCTION	162
EXPERIMENTAL	165
RESULTS AND DISCUSSION	167
SUMMARY	183
REFERENCES	184
GENERAL CONCLUSION	186
REFERENCES	188
ACKNOWLEDGMENTS	192

GENERAL INTRODUCTION

Photoionization occurs when ions are produced as a result of photoabsorption. The earliest studies of photoionization phenomena were done with line sources and by detecting the ions produced purely as a photocurrent.^{1,2} Later, studies were done by measuring the photoions formed as a function of energy, requiring monochromated light production systems,³⁻⁷ and mass spectrometers were incorporated to provide identification of the product ions.^{8,9} This made it possible to find the photoionization efficiency (PIE), which is the intensity of the ion signal divided by the intensity of the transmitted light signal at a given photon energy. If the fraction of photons absorbed by the target gas is small ($\leq 0.01\%$) and the number density of the target gas as well as the interaction volume remain constant, the PIE, plotted as a function of photon energy, can be viewed as relative photoionization cross sections.¹⁰

Possible processes observed in photoionization include direct ionization, autoionization, ion-pair formation, dissociative ionization, and predissociation.¹⁰ Among the different kinds of information which can be obtained by this technique are ionization energies (IE) and vibrational frequencies of molecular ions in various states, the appearance energies (AE) of fragment ions, and thermochemical information which can be derived from these values. This technique has proved to be a useful tool in the elucidation of the interaction of Rydberg states with continuum states. Information on potential energy surfaces can be explored by photoionization studies as well.^{10,12}

Much improvement has been made over early photoionization-mass spectrometric measurements, particularly with respect to optical resolution.^{3-9,11} The main difficulty in obtaining higher resolutions has been the low vacuum ultraviolet (VUV) light intensities available. For this reason, much of the experimental advancement in photoionization has centered around two areas: in improving light intensity, and in increasing the number density of the target molecules in the photoionization collision region. Much of the work on light sources has been reviewed recently by Ng.¹²

As a result of low light intensities, gas cells have been used to hold the target gases at relatively high pressures in order to obtain better signal to noise ratios in ion intensity measurements.^{10,13-15} In these cases, unfortunately, the obtainable resolution was often limited by the rotational population of the gases themselves. For example, for diatomic molecules at room temperature the average rotational energy is nearly 26 meV, and is even larger for polyatomic molecules.¹² Furthermore, the low frequency vibrational levels of target molecules will often be populated. In photoionization, the rotational and vibrational populations will broaden the features of the PIE spectra and make the interpretation difficult. To overcome this difficulty, one response has been to cool the gas cell to lower temperatures. However, this is not possible for gases having high condensation points.

An alternative to the gas cell method is the supersonic molecular beam technique. A supersonic beam involves the expansion of a gas through

a small orifice from a region of high pressure to a region of lower pressure, where the mean free path of molecules in the high pressure (stagnation) region is much shorter than the diameter of the orifice.¹⁶ The molecules undergo large numbers of collisions in the expansion, converting some random translational, rotational, and vibrational energies of the molecules into directed mass flow. When the expansion is complete, the molecules are no longer in a Maxwell-Boltzmann distribution of states. Instead:

- (1) the molecules are nearly unidirectional and are moving at essentially the same speed,
- (2) the number density in the direction of the flow is larger than in a effusive beam of the same initial temperature and pressure, and
- (3) the effective rotational and vibrational temperatures of the gas are substantially reduced.

The cooling of the expansion is more effective for some degrees of freedom than for others. The ultimate effective temperatures of a gas after expansion will usually be in the following order:

$$T_{\text{trans}} < T_{\text{rot}} < T_{\text{vib}} < T_0$$

where T_0 , T_{rot} , T_{vib} , and T_{trans} are the stagnation temperature, and the effective rotational, vibrational, and translational temperatures, respectively. In most cases, the translational temperature will reach nearly 0 K. Rotational temperatures as low as 0.17 K have been reported.¹⁷

Vibrational temperatures of typically 20-50 K are readily attained depending upon the vibrational spacing, initial temperature, and expansion conditions. Thus, in comparison to gas cell experiments, supersonic expansion of the target gas can greatly reduce the limits upon the ultimate achievable resolution while still providing a high constant flux of molecules at the ionization region. Further, if the gas is sampled downstream in a collisionless environment, interference effects, which often occur due to secondary collision processes in gas cell measurements, can be eliminated. For these reasons, the supersonic molecular beam method has been adapted for use in the photoionization-mass spectrometric studies presented in this dissertation. The advantages of this method have been demonstrated previously by Ng, Trevor, Trott, Dehmer, and coworkers.¹⁸⁻²⁹

Most supersonic beam-photoionization-mass spectrometric studies done to date have involved molecules which are gases at room temperature.¹⁰ This is because, in comparison to the construction of supersonic beam sources for nonvolatile target molecules, the construction of sample introduction systems for molecules having high vapor pressures is relatively simple. Of the previous studies on higher temperature vapors, the majority have been done using effusive beam sources.³⁰⁻³⁵ In an effusive beam, the molecules remain in essentially the same translational, rotational and vibrational distribution of states they occupied in the stagnation region. At the higher temperatures required to achieve usable beam fluxes of nonvolatile molecules, hot band effects are

particular severe. It is especially desirable to develop supersonic beam sources for the study of molecules which require higher temperatures to volatilize.¹⁶ Such a beam source has been constructed and used in the photoionization efficiency studies of HgCl_2 , HgBr_2 , and HgI_2 presented in Sections I and II.

Higher concentrations of cluster species can be formed as a result of the cooling effect of molecules in a supersonic expansion. The characteristics of cluster beams have been discussed in detail by Hagen³⁶ and Ng¹². Molecular beam-photoionization-mass spectrometric studies of these molecules can provide information not attainable by other techniques.³⁷⁻⁴³ Studies of the CO_2 , N_2O , CO , N_2 , NO , and O_2 dimers and clusters are presented in Sections III, IV and V. These studies have provided new insights on the bonding of cluster molecular ions, the relaxation of the Rydberg states of clusters, and, as illustrated in Section V, the effects of internal energy upon the reaction dynamics of ion-molecule reactions.

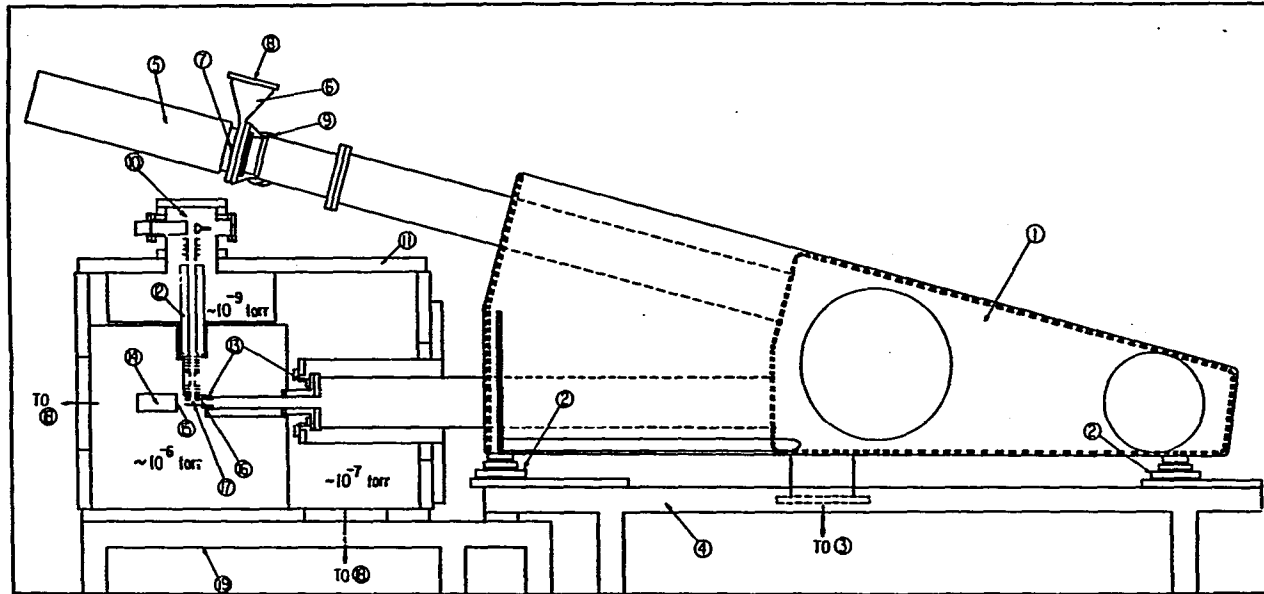


Figure 1. Side view of the photoionization apparatus, (1) monochromator, (2) X-Y translational bench, (3) liquid nitrogen trapped 6 in. diffusion pump, (4) monochromator stand, (5) light source, (6) differential pumping arm, (7) entrance slit, (8) to Roots blower pumping system, (9) to ejector pump, (10) Daly type particle detector, (11) scattering chamber, (12) quadrupole mass spectrometer, (13) flexible coupling bellows, (14) photo detector, (15) sodium salicylate coated quartz window, (16) exit slit, (17) photoionization center, (18) 10 in. diffusion pump system, and (19) stand for scattering chamber

EXPERIMENTAL APPARATUS

The experimental configuration and procedures used in this work have been described in detail previously.^{12,44} Briefly, the apparatus consists of three main parts. They are a vacuum ultraviolet (VUV) light source, a windowless three meter monochromator (McPherson, model 2253) system, a quadrupole mass spectrometer (QPMS) ion detection system, and a supersonic molecular beam production system.

Figure 1 shows the arrangement of the light source, the monochromator, the ion optics, and the QPMS ion detection system. Because no single laboratory light source can produce the necessary VUV light over the entire photon energy range of interest (6-21 eV), three different sources of light are used: the H₂ many-lined pseudocontinuum (850-2000 Å), the He Hopfield continuum (584-1100 Å) and the Ar Hopfield continuum (1050-1550 Å). The He and Ar continua are used in place of the H₂ pseudocontinuum in studies where higher resolution is required (≤ 0.28 Å FWHM) in order to avoid light modulation effects due to the rapidly changing intensities of light with energy in the pseudocontinuum.

Although at energies below 11.9 eV the light source may be coupled to the monochromator by the use of windows, at higher energies windows can seriously reduce the transmitted light intensity. In this apparatus, the lamp is coupled to the monochromator by a differential pumping arm, which steps down the pressure between the lamp and the monochromator. The gas from the lamp enters the pumping arm through an orifice which acts as the entrance slit of the monochromator, and passes through two

pumping stages, the first pumped by a Roots blower (300 CFM) and the second by an ejector pump (300 l/s). This arrangement allows the light source to be coupled to the monochromator without windows. For the He Hopfield continuum, the lamp is normally operated at 80-100 Torr, while the monochromator chamber can be maintained at pressures below 10^{-4} Torr.

The monochromator chamber is pumped by a liquid nitrogen trapped 6" diffusion pump. At pressures better than 10^{-4} Torr, backstreaming of the pump oil is negligible, maintaining an oil free environment for the grating. Two 1200 lines/mm aluminum gratings blazed at 1360 \AA are used. For maximum efficiency, an Os coated grating is used between $500-1100 \text{ \AA}$, while a MgF_2 coated grating is used between $1100-2000 \text{ \AA}$.

The light exiting the monochromator passes through the ionization region and is incident on a sodium salicylate coated window, the fluorescence of which is detected by a photomultiplier tube (PMT). The DC signal of the PMT is converted to a digital signal by a voltage to frequency converter and is then counted.

The positive ions produced by the photons incident on the ionization region are repelled upward and are focused by the ion lenses onto the aperture of the QPMS. Ions of the desired mass to charge ratio are then detected by a Daly type ion detector.⁴⁵ This device converts the ion signal to a light signal, which is in turn converted to a current by a photomultiplier tube. In order to reduce background ion signals and to avoid attenuation of the ion signal by background gases, this region

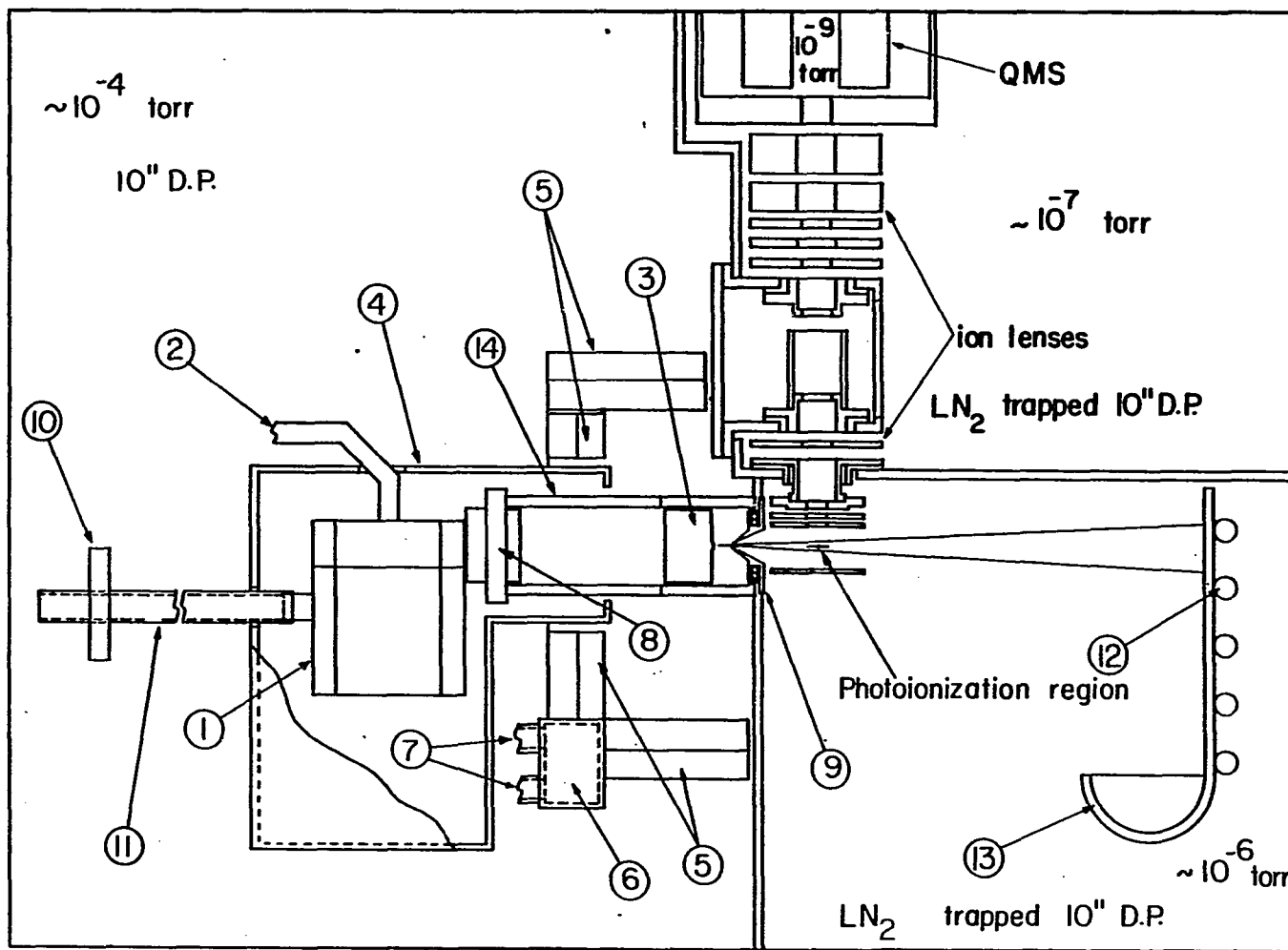
is maintained at $\sim 10^{-8}$ Torr by a liquid nitrogen (LN_2) trapped 4" diffusion pump. The ionization chamber and the ion focusing region are kept at 10^{-5} — 10^{-6} Torr and $\sim 10^{-7}$ Torr, respectively, by LN_2 trapped 10" diffusion pumps.

The basic concept of the supersonic beam production system has been touched on briefly in the GENERAL INTRODUCTION. Essentially, the subject molecules pass from a region of high pressure (100-1500 Torr) to a region of low pressure (10^{-3} — 10^{-4} Torr) through a small orifice. The orifices used in these studies ranged from 0.05 mm to 0.127 mm. The beam then passes through a conical skimmer and is intersected by the VUV photon beam at the ionization region. The nozzle-skimmer distance was maintained at approximately 0.64 cm, while the skimmer orifice was 0.76 mm in diameter.

Two beam sources were utilized in this study. The first is a high temperature oven-type supersonic beam source for the study of higher temperature vapors (Sections I and II). The other is a low temperature cryogenic source capable of producing high concentrations of cluster species (Sections III, IV and V).

Figure 2 shows the detailed cross-sectional view of the differential pumping arrangement of the oven-type supersonic beam production system, the ionization region, the ion optics, and the quadrupole mass spectrometer used in Sections I and II. The oven, having a capacity of approximately 17 cm^3 , was constructed of stainless steel. It essentially consists of the main oven and nozzle which can be heated independently

Figure 2. Cross-sectional view of the differential pumping arrangement of the oven-type supersonic beam production system, ionization region, ion optics, and quadrupole mass spectrometer. (1) main oven and oven heater, (2) carrier-gas inlet, (3) nozzle and nozzle heater, (4) water-cooled copper cold shield, (5) 45° optically dense copper chevrons, (6) LN₂ reservoir, (7) LN₂ inlet and outlet, (8) heated skimmer, (9) nozzle-stop collar, (10) X-Y translator, (11) thin-wall stainless steel tube, (12) LN₂ channels, (13) LN₂ cold trap, (14) alignment collar



by heating elements embedded in the bodies of the oven and nozzle. The main oven can be further separated into the upper and lower ovens which are sealed together by a Conflat metal gasket type seal during the experiment. This feature made it possible to open the oven for cleaning and reloading. By using copper or aluminum gaskets, reliable seals can be maintained at a temperature ≤ 675 K. Most of the data presented in Sections I and II were taken with the temperature ranges of the oven and nozzle between 465-500 K and 490-525 K, respectively. Maintaining a slightly higher temperature for the nozzle than that of the oven is necessary to prevent clogging of the nozzle by the sample material. In operation, the oven was wrapped by several layers of tantalum foil as radiation shields. The whole oven was further enclosed by a water cooled copper cold shield. In a typical run, the fluctuation in the nozzle and oven temperatures was less than ± 3 K as monitored with thermocouples.

At an oven temperature of 470 K, typical vapor pressures of HgX_2 were estimated to be ~ 80 -100 Torr. By maintaining the pressure of the helium or argon carrier gases (which entered the oven through the carrier-gas inlet) in the range of 250 to 650 Torr in this experiment, the back-streaming of the sample into the inlet was found to be negligible. The nozzle diameter used was 0.127 mm. Under these expansion conditions, the source can operate continuously for a period of 36 hrs on one sample charge.

The alignment of the nozzle was accomplished by the precise coaxial engagement of the nozzle with the alignment collar, the axis of which

intersects the photoionization center. The oven was also secured to an x-y translator by a thin wall stainless steel tubing in order to release the stress of the alignment collar exerted by the weight of the oven. The nozzle-stop collar, its position fixed by a set screw, stops the nozzle tip at a preset distance from the skimmer. In this experiment, the nozzle-skimmer distance was kept at 0.64 cm. The beam, thus aligned, passes through the skimmer and then through a collimation slit before reaching the photoionization region. The collimation slit, which was positioned between the skimmer and ion-optics, is not shown in Figure 2.

A heated skimmer was used in this study. By maintaining the skimmer at a temperature approximately equal to that of the main oven, it is possible to eliminate the condensation problem. However, in order to minimize the attack by the HgX_2 vapor on the skimmer heater, the heating wire was coated with ceramic cement and encased with a metal shield. The procedure also prevented any stray light emitted by the heating wire of the skimmer from reaching the photon detector.

Also shown in Figure 2 are two LN_2 traps. Due to the poisonous nature of the mercury halides, it was desirable to trap the sample gases. One of the traps, mounted directly in the path of the beam, was at about 160 K during the experiment. The other trap was constructed by soldering 45° optically dense copper chevrons to the LN_2 reservoir. A temperature of 110 K was maintained at this trap.

Sections III, IV and V deal primarily with the study of clusters. The concentration of clusters in a beam depends in part on the extent

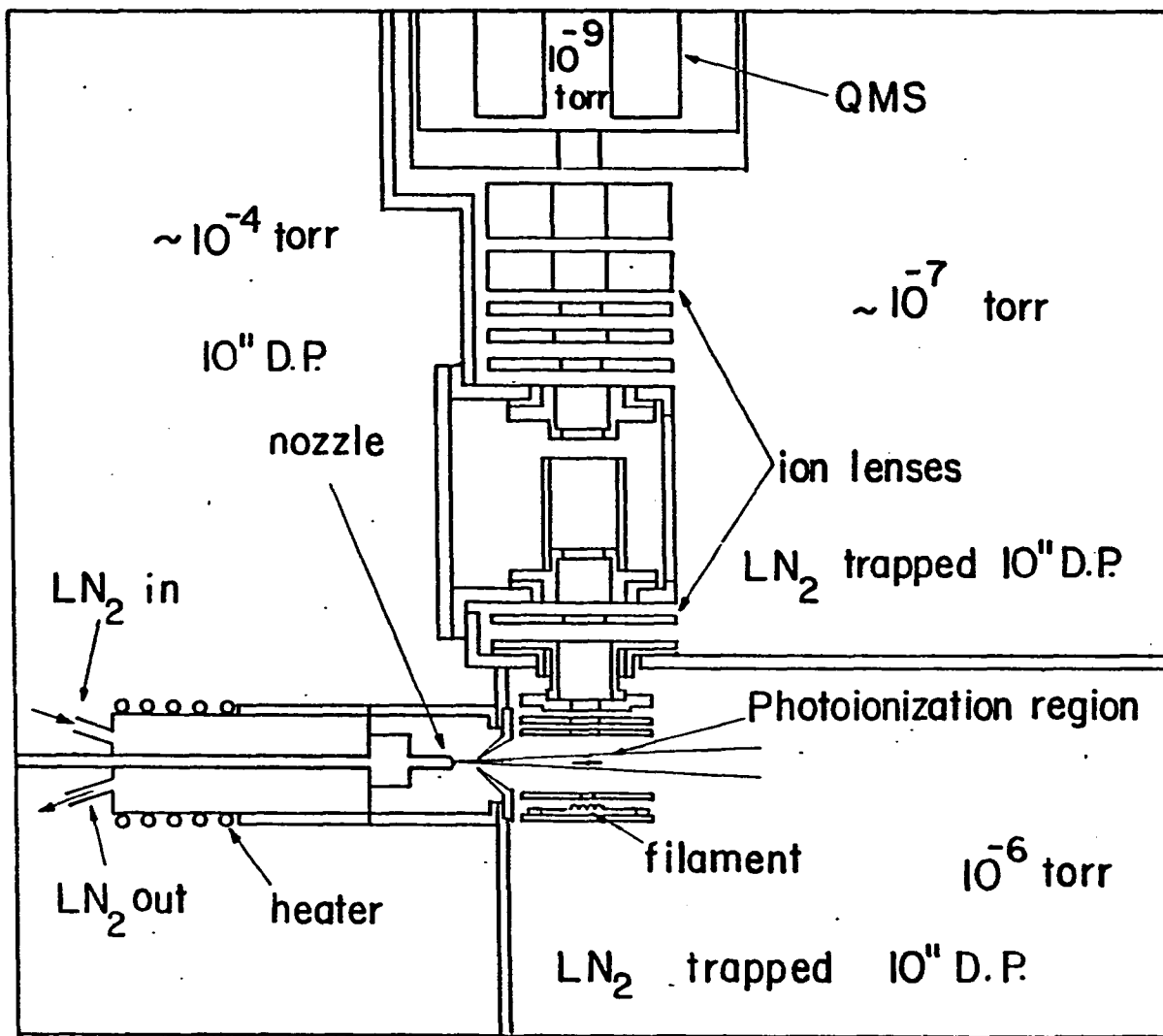
of cooling which takes place as a result of the expansion. Cluster formation can be increased by lowering the nozzle temperature, and by using larger nozzle diameters and higher stagnation pressures.

A diagram of a variable temperature nozzle is shown in Figure 3 with the rest of the molecular beam production system, the ionization region, the ion optics and the quadrupole mass spectrometer. The details of this beam source have been described previously.⁴⁰⁻⁴² The nozzle assembly is constructed of stainless steel and consists primarily of a stagnation region, which is surrounded by a cooling jacket.

The temperature of the nozzle can be lowered to ~90 K by cooling the nozzle with liquid nitrogen, and may be maintained at ± 5 K of the desired temperature by controlling the rate at which liquid nitrogen is fed to the cooling jacket. In many cases this makes it possible to cool the sample gases considerably before expansion. In addition, the pressure of the stagnation region may be carefully controlled by the use of pressure regulators. The combination of temperature and pressure controls made it possible to optimize the concentration of a particular cluster of interest in the beam. In some cases it was possible to minimize the interference of fragments from higher clusters by reducing the concentration of higher clusters in the beam. The cluster molecules studied in Sections III, IV and V were all produced in this fashion.

The data acquisition system is controlled by a Motorola 6800 microprocessor.⁴⁴ Basically, the monochromator scans to a wavelength determined by the microprocessor, and counts the light and ion signals

Figure 3. Cross sectional view of the differential pumping arrangement of the molecular beam production system, ionization region, ion optics, and quadrupole mass spectrometer



for a preset length of time. The microprocessor then computes the ratio of the ion signal to the light signal (i.e., the PIE) and stores it with the corresponding value of the wavelength, the light signal and the ion signal. The monochromator is then instructed to scan to the next wavelength and the cycle is repeated.

The data thus acquired are printed out and can be stored on a cassette tape. From these data, the PIE were plotted as functions of wavelength. The spectra presented in Sections I-V were recorded in this fashion and are representative of this process. Plots of the light intensity were used to calibrate the plots of the PIE, using the positions of known atomic resonances, and H₂ emission lines where necessary.

GENERAL THEORY

Direct Photoionization

Direct photoionization occurs when a molecule is excited directly from a neutral state into an ionic state. If Ψ_i is the initial state, Ψ_f is the final state (including the wavefunction of the electron), and $\sum_u P_u$ is the dipole moment operator, to a first approximation the transition moment can be written;^{10,15}

$$\langle \Psi_f | \sum_u P_u | \Psi_i \rangle \quad (1)$$

If the transition takes place in a time that is short compared to the vibrational period of the molecule, the wavefunctions can be separated into the electronic and nuclear parts according to the Born-Oppenheimer approximation:

$$\Psi(r,R) = \Psi_e(r,R) \Psi_n(R), \quad (2)$$

where r and R represent the electronic and nuclear coordinates, respectively. In addition, if the interaction between rotational and vibrational motion can be neglected, $\Psi_n(R)$ can be further broken down:

$$\Psi_n(R) = \frac{1}{R} \Psi_v(R) \Psi_t(R), \quad (3)$$

where $\Psi_t(R)$ represents the rotational wavefunction. Furthermore, the dipole operator $\sum_u P_u$ may be expressed as the summation of both the nuclear and electronic coordinates:

$$\sum_u P_u = \sum_j P_j^n + \sum_l P_l^e. \quad (4)$$

These results, when substituted into Eq. 1 yield:

$$\begin{aligned} \langle \Psi_f | \hat{U}^{\Sigma P} | \Psi_i \rangle & \quad (5) \\ &= \frac{1}{R^2} \int \Psi_{v,f}^*(R) \Psi_{t,f}^*(R) | \hat{U}_j^{\Sigma P} | \Psi_{v,i}(R) \Psi_{t,i}(R) dR \int \Psi_{e,f}^*(r,R) \Psi_{e,i}(r,R) dr \\ &+ \frac{1}{R^2} \int \Psi_{v,f}^*(R) \Psi_{t,f}^*(R) \Psi_{r,i}(R) \Psi_{v,t}(R) dR \int \Psi_{e,f}^*(r,R) | \hat{U}_e^{\Sigma P} | \Psi_{e,i}(r,R) dr. \end{aligned}$$

Since the first term in this expression must vanish due to the orthogonality of the electronic eigenfunctions, the transition matrix element can be written (ignoring rotation):

$$\langle \Psi_f | \hat{U}^{\Sigma P} | \Psi_i \rangle = \frac{1}{R^2} \int \Psi_{v,f}^*(R) \Psi_{v,i}(R) dR \int \Psi_{e,f}^*(r,R) | \hat{U}_e^{\Sigma P} | \Psi_{e,i}(r,R) dr \quad (6)$$

The transition probability from the initial to the final state is therefore proportional to the square of the matrix element:

$$\begin{aligned} \text{Probability} & \propto \left| \int \Psi_{e,f}^*(r,R) | \hat{U}_e^{\Sigma P} | \Psi_{e,i}(r,R) dr \right|^2 \quad (7) \\ & \times \left| \int \Psi_{v,f}^*(R) \Psi_{v,i}(R) dR \right|^2, \end{aligned}$$

where $\left| \int \Psi_{v,f}^*(R) \Psi_{v,i}(R) dR \right|^2$ is the Franck-Condon factor.

The direct photoionization cross section at a particular energy is proportional to the sum of Eq. 7 over all available initial and final states:

$$\sigma \propto \sum_i \sum_f \left| \int \Psi_{e,f}^*(r,R) | \hat{U}_e^{\Sigma P} | \Psi_{e,i}(r,R) dr \right|^2 \left| \int \Psi_{v,f}^*(R) \Psi_{v,i}(R) dR \right|^2 \quad (8)$$

Relative values of the cross section are recorded as a function of energy in a PIE curve. The manifestation of direct photoionization as a step function behavior near the threshold behavior of PIE curves has been discussed previously in more detail by Ng¹⁸ and Ono.⁴⁴

Autoionization

The removal of an electron from an atom or molecule which does not involve a transition directly into the continuum is known as autoionization. Autoionization is the result of configuration interactions of a discrete state with ionizing continuum states which are either degenerate or nearly degenerate in energy with the discrete state.

The theory of the interaction of one discrete state and one continuum has been developed by Fano.^{46,47} Beginning with a discrete state ψ and a set of continuum states $\psi_{E'}$, a new state $\bar{\psi}_E$ is written as a linear combination of ψ and the $\psi_{E'}$:

$$\bar{\psi}_E = a\psi + \int dE' b_{E'} \psi_{E'} \quad (9)$$

where a and b are determined by the following constraints:

$$\begin{aligned} (\psi | H | \psi) &= E_\psi \\ (\psi_{E'} | H | \psi) &= V_{E'} \\ (\psi_{E''} | H | \psi_{E'}) &= E' \delta(E'' - E') \end{aligned} \quad (10)$$

Solution for the coefficients a and b yields:

$$a = \frac{\sin \Delta}{\pi V_E} \quad (11)$$

$$b_{E'} = \frac{V_{E'}}{\pi V_E} \frac{\sin \Delta}{E - E'} + \cos \Delta \delta(E - E') \quad (12)$$

where Δ is the phase shift in $\psi_{E'}$ at large r due to configuration interaction and is equal to

$$\Delta = -\arctan \frac{\pi |V_E|^2}{E - E_\psi - F(E)} \quad (13)$$

$$F(E) = \frac{P \int dE' |V_{E'}|^2}{E - E'} \quad (14)$$

With these coefficients, the resonance energy of the state $\bar{\Psi}_E$ is $E = E_\psi + F(E)$, meaning it is shifted from the energy of the original discrete state by a function $F(E)$. Further, the state ψ is diluted through a continuum of states $\Psi_{E'}$, forming a set of stationary states $\bar{\Psi}_E$ of energy $E = E_\psi + F(E)$ which have a profile corresponding to a resonance of half width $\pi |V_E|^2$. This means that if the state could be prepared at some instant, it would decay with a half-life of $\pi/2\pi |V_E|^2$.

The matrix element representing the excitation of some initial state i to the state $\bar{\Psi}_E$ can be written as $(\bar{\Psi}_E | T | i)$ where T is some operator suitable to the excitation mechanism. Using the form of $\bar{\Psi}_E$ given by equations (9), (11), and (12),

$$\begin{aligned} (\bar{\Psi}_E | T | i) &= \frac{1}{\pi V_E^*} (\psi | T | i) \sin \Delta + \frac{1}{\pi V_E^*} P \int dE' V_{E'} \frac{(\Psi_{E'} | T | i)}{E - E'} \sin \Delta \\ &\quad - (\Psi_E | T | i) \cos \Delta \end{aligned} \quad (15)$$

$$\text{or} \quad = \frac{1}{\pi V_E^*} (\Phi | T | i) \sin \Delta - (\Psi_E | T | i) \cos \Delta, \quad (16)$$

$$\text{where} \quad \Phi = \psi + P \int dE' \frac{V_{E'} \Psi_{E'}}{E - E'}$$

and can be thought of as the pseudodiscrete state formed by the configuration interaction.

This result reveals a marked energy dependence of $(\bar{\Psi}_E | T | i)$ near

$E = E_\psi + F$. While $\sin\Delta$ is an even function centered at $E = E_\psi + F$, $\cos\Delta$ is an odd function, causing the contributions from $(\Phi|T|i)$ and $(\Psi_E|T|i)$ to interfere with opposite phase on one side of $E = E_\psi + F$, and with the same phase on the other.

The square of this matrix element represents the probability of a transition to the $\bar{\Psi}_E$ state. By introducing the variables

$$\epsilon = \frac{E - E_\psi - F(E)}{\pi |V_E|^2} = \frac{E - E_\psi - F}{1/2 \Gamma} \quad (17)$$

and

$$q = \frac{(\Phi|T|i)}{\pi V_E^* (\Psi_E|T|i)}, \quad (18)$$

where q is the Fano line shape parameter, the probability of the transition to $\bar{\Psi}_E$ can be written:

$$|(\bar{\Psi}_E|T|i)|^2 = |(\Psi_E|T|i)|^2 [1 + (q^2 - 1 + 2q\epsilon) / (1 - \epsilon^2)]. \quad (19)$$

$|(\bar{\Psi}_E|T|i)|^2$, which is proportional to the photoabsorption cross section, is plotted as a function of wavelength for various values of q in Figure 4. Typically, lines of high q are sharply peaked, while lines of q values of less than two are highly asymmetric. As q approaches zero, the resonance will appear as a dip in the spectra known as a window resonance.

Fano extended this treatment to the interaction of one discrete state with several continua.⁴⁷ The treatment begins with N continuum states at a given energy. Linear combinations of the N states are

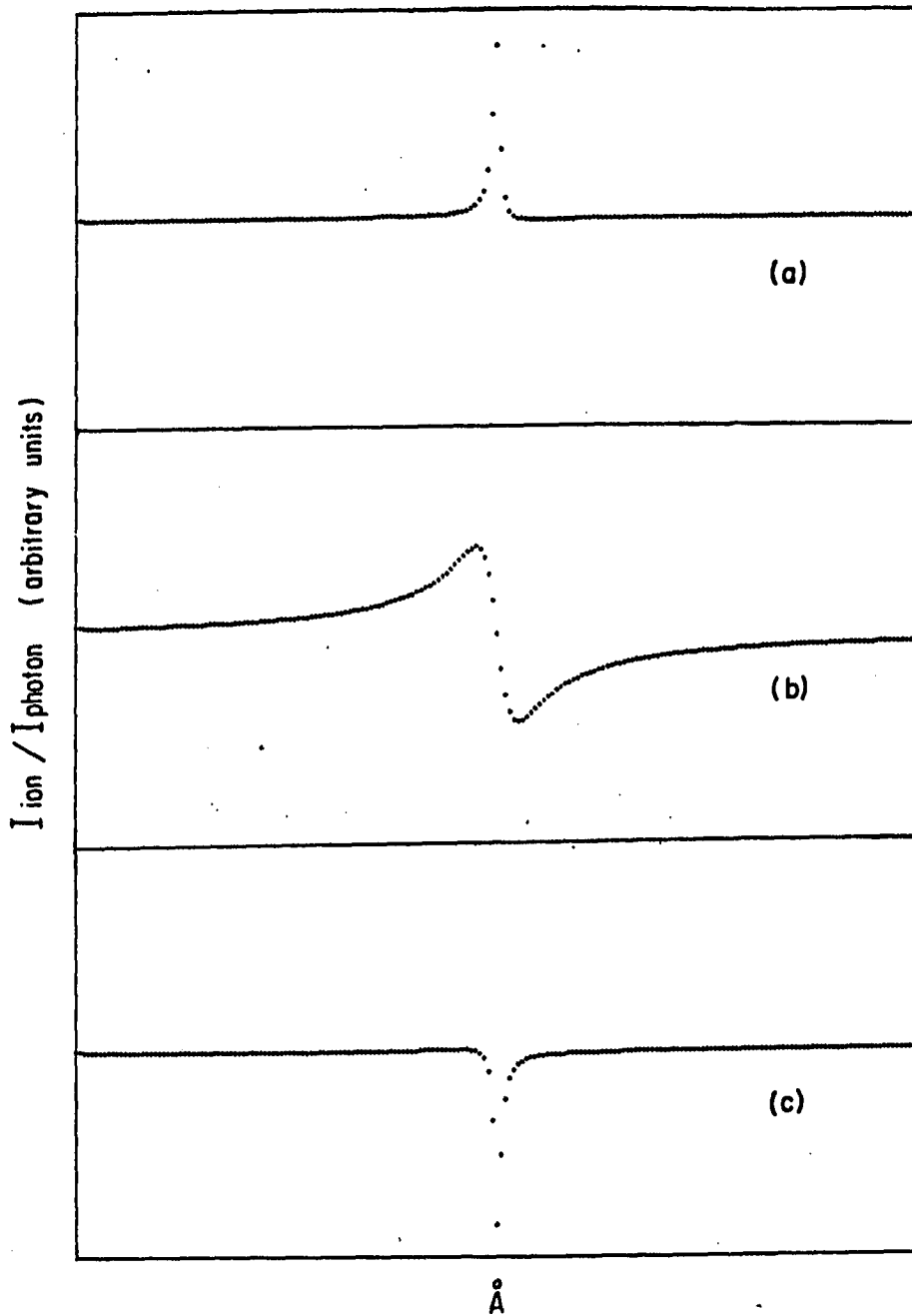


Figure 4. Resonance line shapes of $\Gamma = 1 \text{ \AA}$ at 900 \AA , where q equals (a) 10.0, (b) 1.0, and (c) 0.1. Points plotted every $.1 \text{ \AA}$

taken, forming a new set of N states. Of the N new states, one state interacts with the discrete state and the $N-1$ other states form a set of background states which are unaffected by the discrete state.

While these states are adequate for the description of the excitation process, there is no simple relationship linking them to the final observable states which result from the excitation. For example, in this treatment there would be no simple relationship between the eigenstates of the photoabsorption process and final states having a well-defined energy for the residual ion and the kinetic energy of the ejected electron, as are observed in autoionization.

Starace⁴⁸ solved this problem by writing the desired final states of a total energy E in terms of a linear combination of the eigenstates of the excitation process:

$$|0_K, E\rangle = \sum_{\lambda=1}^N |\bar{\Psi}_{\lambda}, E\rangle X_{\lambda}^{(K)} \quad (20)$$

where $|0_K\rangle$ is the observed state of channel K , the λ are the indices of the excitation eigenstates, and the $X_{\lambda}^{(K)}$ represent the coefficients, determined subject to the condition that the amplitude for all outgoing spherical waves in channels other than K vanish. The matrix element of the excitation from some state i to the final observed state was found and squared. The result, written in terms of the variables used by Fano⁴⁷ is:

$$\begin{aligned} |\langle 0_K | T | i \rangle|^2_{\text{total}} \\ = \frac{|\langle 0_K | T | i \rangle|^2_{\text{continuum}}}{1 + \epsilon^2} \end{aligned} \quad (21)$$

$$x\{\epsilon^2 + 2\epsilon[q\text{Re}\alpha(\mu E) + i\text{Im}\alpha(\mu E)] + [1 - 2q\text{Im}\alpha(\mu E) - 2\text{Re}\alpha(\mu E) + q^2 + 1|\alpha(\mu E)|^2]\}$$

The expression $\alpha(\mu E)$ represents the fraction of the dipole amplitude that passed through the only eigenchannel which interacts with the discrete state.⁴⁸

Eland et al.⁴⁹ have given this equation in a more intuitive form:

$$\sigma_K = \sigma_{cK} \left[1 + \frac{\rho_K^2}{\epsilon^2 + 1} (q^2 + 1 + \frac{2}{\rho_K} [(q\epsilon - 1)\cos\phi_K - (q + \epsilon)\sin\phi_K]) \right] \quad (22)$$

where $\sigma_K = |\langle 0_K | T | i \rangle|_{\text{total}}^2 = \text{Channel K Cross Section}$

$\sigma_{cK} = |\langle 0_K | T | i \rangle|_{\text{continuum}} = \text{Continuum Cross Section in Channel K}$

$\sigma_{rK} = \text{resonance cross of Channel K}$

$$e_K^2 = |\alpha(\mu E)|^2 = \frac{\sigma_{rK}}{\sigma_{cK}}$$

and ϕ_K is a phase angle difference.

In photoionization efficiency measurements without coincident measurement of the kinetic energy of the ejected electron, single channels of decay from the pseudodiscrete state are not observed. At a particular photon energy, all ions of the desired mass, m , are measured regardless of the number of channels, K , producing them. Therefore, the observed partial cross section is actually

$$\sigma_m = \sum_K^{(m)} \sigma_K, \quad (23)$$

where m denotes the ions of mass m . Eland et al.⁴⁹ has written this

expression in terms of Eq. 22:

$$(\sigma_m - \sigma_{cm})(\epsilon^2 - 1) = (q^2 + 1) \sum_K^{(m)} \rho_K^2 \sigma_{cK} \quad (24)$$

$$\begin{aligned} & -2 \sum_K^{(m)} \rho_K \sigma_{cK} (\cos \phi_K - q \sin \phi_K) \\ & - 2\epsilon \sum_K^{(m)} \rho_K \sigma_{cK} (q \cos \phi_K - \sin \phi_K) \end{aligned} \quad (25)$$

$$= A_m + B_m \epsilon$$

where

σ_m = cross section of fragment m,

σ_{cm} = cross section of the background continuum,

$A_m = (q^2 + 1) \sum_K^{(m)} \rho_K \sigma_{cK} - 2 \sum_K^{(m)} \rho_K \sigma_{cK} (\cos \phi_K + q \sin \phi_K),$

$B_m = \sum_K^{(m)} \rho_K \sigma_{cK} (q \cos \phi_K - \sin \phi_K).$

Since ρ_K , σ_K , σ_{cK} , and q contain no factors dependent on ϵ , the asymmetry of the resonant behavior in Eq. 24 is contained within the $\epsilon/\epsilon^2 - 1$ terms, as was the case in Fano's original treatment.⁴⁹ For a given resonant state, the resonance energy and line width is the same in all observed channels of decay: these values are the same as those observed for photoabsorption. This makes it possible to find the resonance energy by a simple parameterization procedure.⁵⁰

Given the resonance energies and the Rydberg equation^{10,15,51}

where

$$\frac{1}{\lambda} = IE - \frac{R}{(n-\delta)^2}, \quad (26)$$

λ = the resonance wavelength,

n = the principal quantum number,

δ = the quantum defect,

R = the Rydberg constant

the Rydberg structure in the PIE curves of molecular ions and ionic fragments can be analyzed. The details of this treatment have been given in part by Fano,⁴⁷ Berkowitz,¹⁰ and others.^{49,50}

SECTION I.

MOLECULAR BEAM PHOTOIONIZATION

STUDY OF HgCl_2

ABSTRACT

High resolution (0.14 Å FWHM) photoionization efficiency (PIE) data for HgCl_2^+ have been obtained in the region 730-1100 Å using an oven-type supersonic beam source. The ionization energies of the spin-orbit states $^2\Pi_{3/2g}$ and $^2\Pi_{1/2g}$ were determined to be 11.380 ± 0.003 and 11.505 ± 0.003 eV, respectively. The major fragment ions observed in the region 600-1300 Å are HgCl^+ , Hg^+ and Cl^+ having appearance energies of ≤ 11.041 , 12.594 ± 0.018 , and 16.721 ± 0.032 eV, respectively. The latter value allows the calculation of the bond dissociation energy for HgCl to be 21.1 ± 2.2 kcal/mol. This study further revealed members of autoionizing Rydberg series converging to the $^2D_{\pm 5/2}$ and $^2D_{\pm 3/2, \pm 1/2}$ states of 16.715 ± 0.003 and 18.65 eV, respectively, which exhibit highly asymmetric Beutler-Fano line profiles. The comparison of the PIE curve for Hg^+ from Hg and those for HgCl_2^+ and its fragments unambiguously shows that autoionizing Rydberg series resolved in this study can be assigned to transitions $[(5d)^{10} \sigma_g^2 \sigma_u^2 \pi_u^4 \pi_g^4] \rightarrow [(5d)^9 \sigma_g^2 \sigma_u^2 \pi_u^4 \pi_g^4 \ ^2D_{\pm 5/2}] np$ and $[(5d)^{10} \sigma_g^2 \sigma_u^2 \pi_u^4 \pi_g^4] \rightarrow [(5d)^9 \sigma_g^2 \sigma_u^2 \pi_u^4 \pi_g^4 \ ^2D_{\pm 3/2, \pm 1/2}] np$, $n \geq 6$, which are mainly associated with the mercury atom in HgCl_2 .

INTRODUCTION

Photoionization mass spectrometry is a versatile and accurate method for obtaining thermochemical data for gaseous molecules. Because of the relative simplicity in the construction of sample introduction systems for gases having high vapor pressures at room temperature, the preponderance of the photoionization studies done to date have been of this kind.¹ Due to complications involved in working at high temperatures, photoionization mass spectrometric studies of samples which are solid at room temperature are relatively scarce.

In the main body of previous photoionization work on high temperature vapors, the overwhelming majority has been performed using effusive-oven sources.²⁻⁷ The higher temperatures required to volatilize the sample materials will increase the rotational and vibrational populations of the subject molecules in comparison with those at room temperature. Therefore, the hot-band effects are expected to be more severe in high temperature experiments than in the studies of volatile compounds. In view of the efficient relaxation of the rotational and low-frequency vibrational excitations of molecules in a supersonic expansion,⁸ it is highly desirable to couple the supersonic molecular beam method to photoionization studies of high-temperature vapors. Although most of these vapors are extremely corrosive in nature, with proper selection of oven materials, it is possible to construct reliable supersonic molecular beam sources for many of these high-temperature systems. We believe that molecular beam photoionization studies of high temperature

compounds is a fruitful research area. Since only moderate temperatures are required to vaporize the mercury halides, HgX_2 , $X = \text{Cl}$, Br , and I , they were chosen to be the first system for study in this direction.

The study of the mercury halides is also motivated by the current interest in the vacuum-ultraviolet and ultraviolet chemistry of these compounds.⁹⁻¹² Mercury monohalides HgX are potential candidates for efficient high-power visible lasers.¹³⁻¹⁷ Lasing has been achieved by using electron beam,^{18,19} electric discharge,¹⁶ and photodissociation^{20,21} of the parent mercury dihalides as the pumping methods. In electron impact and electric discharge of the mercury dihalides, it is likely that ionic species will play a role in the kinetics for the formation of the excited lasing state of HgX . Thus, photoionization data for the mercury dihalides should be relevant to the detailed characterization of the kinetics and optimization in performance for the mercury halide laser systems.

The prominent structure resolved in the PIE curve for Hg^+ from Hg ^{22,23} was attributed to autoionizing Rydberg series corresponding to excitations of inner shell 5d electrons of Hg to np , $n \geq 6$, Rydberg orbitals. Since one expects that the 5d orbitals, especially the $5d_{x^2-y^2}$ and $5d_{xy}$ orbitals of Hg in HgX_2 only play a minor role in the bonding of the mercuric halides and remain mostly atomic in nature, the Rydberg transitions $5d \rightarrow np$, $n \geq 6$, should also be manifest as prominent structures in the photoabsorption spectrum of HgX_2 . Whether

these transitions will appear as autoionizing features in the PIE curves for HgX_2^+ and its fragment ions depends on the interactions of the discrete np Rydberg orbitals with continuum states of HgX_2^+ and HgX_2 . The extent of these interactions can be proved by the line shapes of the autoionizing Rydberg series.²⁴⁻³⁸ It should be interesting to compare the Beutler-Fano profiles²⁴⁻²⁶ of the autoionization structure resolved in the PIE curves for Hg^+ from Hg and that for HgX_2^+ .

The electronic structures of HgX_2 have been studied previously by photoelectron spectroscopy.³⁹⁻⁴⁴ An earlier study of the fragmentation of this system by electron impact ionization was reported by Kiser *et al.*⁴⁵ This report presents the results and an analysis of the photoionization experiment on HgCl_2 . Photoionization efficiency (PIE) data on HgBr_2 and HgI_2 will be discussed in a separate publication.⁴⁶

EXPERIMENTAL

The experimental arrangement and procedures are similar to those described previously.⁴⁷ Briefly, the apparatus consists of a windowless 3-m near normal incidence VUV monochromator (McPherson 2253 M), an oven supersonic beam production system, a capillary discharge light source, and a quadrupole mass filter for ion detection. The grating employed in this study was a Bausch and Lomb 1200 lines/mm MgF_2 coated aluminum grating blazed at 1360 \AA . Either the hydrogen many-lined pseudocontinuum or the helium Hopfield continuum was used as the light source depending on the wavelength region desired.

The HgCl_2 used in this study was obtained from Fisher Scientific Company. It was 99.99% pure and was used without further purification.

The major ions observed in the region 600-1150 \AA are HgCl_2^+ , HgCl^+ , Hg^+ , Cl^+ . Within the sensitivity of this apparatus, no Cl_2^+ ions were found. Fragment ions, Hg_2Cl_2^+ and Hg_2Cl_3^+ from $(\text{HgCl}_2)_2$ were also observed. However, the intensities of these ions were too low for the measurements of their PIE spectra. Since the mass of the $(\text{HgCl}_2)_2^+$ ion is beyond the mass range of our quadrupole mass spectrometer, its intensity could not be probed. After the operation of the oven source for about 10 hrs from a fresh sample charge, the measured spectrum for Hg^+ was found to resemble the PIE curve for Hg^+ from Hg. In order to avoid the accumulated effect of mercury due to the thermal dissociation of HgCl_2 , the PIE curve for Hg^+ from HgCl_2 was recorded immediately after a reloading of the oven.

The PIE curves for HgCl_2^+ , HgCl^+ , Hg^+ and Cl^+ from HgCl_2 obtained by using an optical resolution of 1.4 \AA (FWHM) in the region $\sim 620\text{-}1100 \text{ \AA}$ are shown in Figs. 1(b), 1(c), and 1(e), respectively. These spectra were taken and plotted at intervals of 0.5 \AA with the exception of the curve for Cl^+ , which was taken and plotted at intervals of 1 \AA . The high resolution (0.14 \AA FWHM) PIE data for HgCl_2^+ in the regions, $1030\text{-}1100$ and $735\text{-}995 \text{ \AA}$, which are shown in Figs. 2(a), 2(b), and 2(c), were accumulated at intervals of 0.1 \AA . The standard deviations for PIE data achieved in this experiment are in general $\leq \pm 5\%$.

All of the PIE spectra presented here are based on a minimum of two reproducible scans. The wavelength scales were calibrated by using known atomic resonance lines or H_2 emission lines⁴⁸ when the H_2 pseudocontinuum was used.

RESULTS AND DISCUSSION

The analysis of the 584 Å photoelectron spectra (PES) of HgX_2^0 shows that these linear, symmetric molecules have an orbital sequence of $\dots d^{10} \sigma_g^2 \sigma_u^2 \pi_u^4 \pi_g^4$.³⁹ Upon ionization from the four valence orbitals, the ionic states formed are the ${}^2\Pi_{3/2g}$, ${}^2\Pi_{1/2g}$, ${}^2\Pi_{3/2u}$, ${}^2\Pi_{1/2u}$, ${}^2\Sigma_u$, and ${}^2\Sigma_g$ states. The removal of an electron from the full $5d^{10}$ shell of the mercury atom gives rise to the ${}^2D_{5/2}$ and ${}^2D_{3/2}$ states for Hg^+ . Eland³⁹ points out that the interactions of the latter states with the molecular field in HgX_2 are similar to that expected of a weak field Stark effect. The ${}^2D_{5/2}$ state should be split into three components of equal statistical weight, $\pm 5/2$, $\pm 3/2$, $\pm 1/2$, and the ${}^2D_{3/2}$ state should be split likewise into $\pm 3/2$ and $\pm 1/2$. The designation of the states for HgCl_2^+ will follow those used by Eland.³⁹

The ionization energies (IEs) for states of HgCl_2^+ determined by photoelectron spectroscopy³⁹⁻⁴⁴ are indicated in the PIE curve for HgCl_2^+ in Fig. 1(b). No apparent structure correlating to the onsets of these states can be seen with the exception of those for the $\tilde{X}^2\Pi_{3/2g}$ and ${}^2\Pi_{1/2g}$ states where sharp step-like features were found. The positions of these two steps were located at 1089.5 and 1077.7 Å⁰ with an uncertainty of ± 0.3 Å⁰ in the high resolution PIE curve for HgCl_2^+ [Fig. 2(a)]. Therefore, the IEs of the $\tilde{X}^2\Pi_{3/2g}$ and ${}^2\Pi_{1/2g}$ states were determined to be 11.380 ± 0.003 and 11.505 ± 0.003 eV, respectively, yielding a value of 0.125 ± 0.004 eV for the spin-orbit

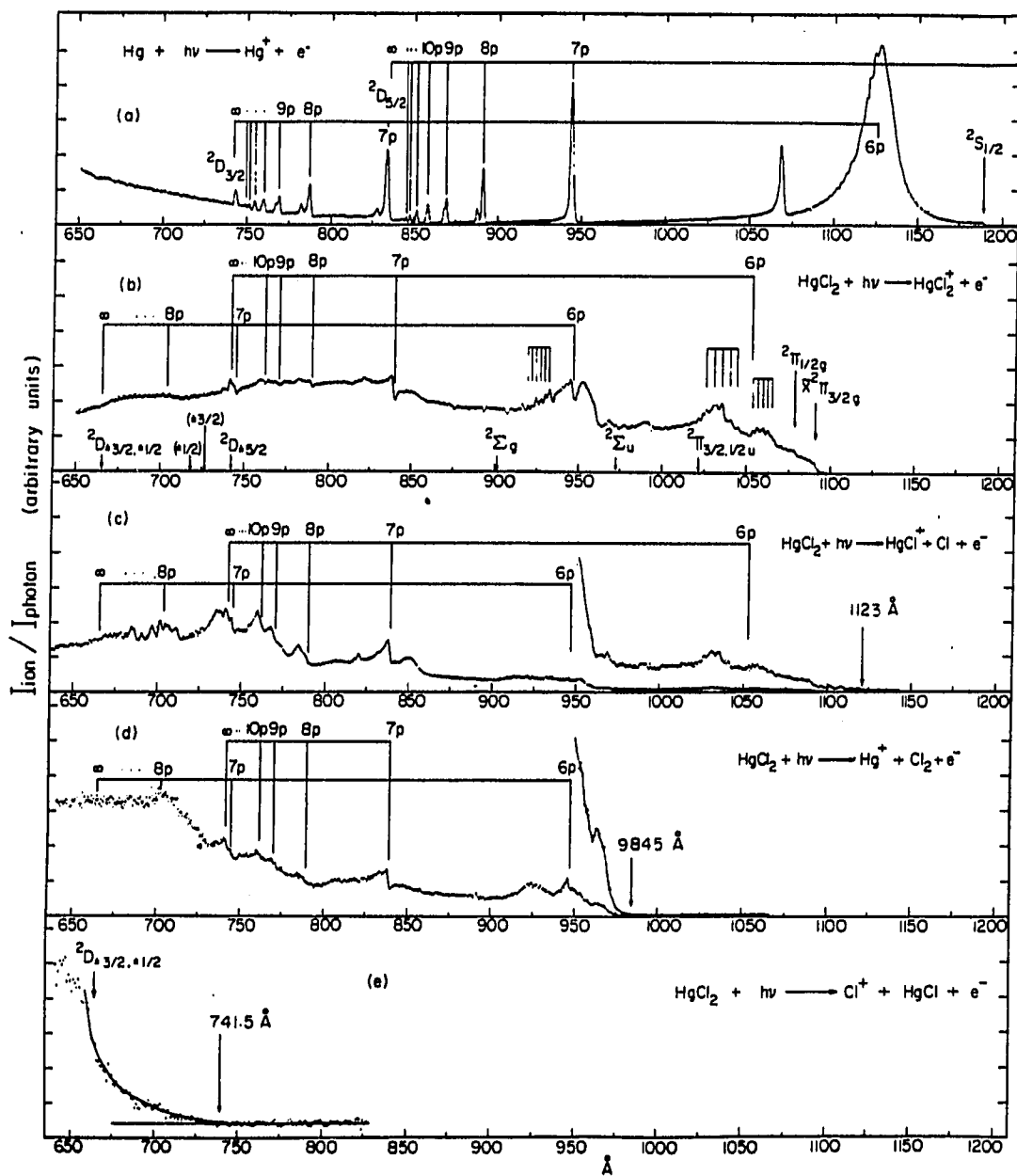


Figure 1. The PIE curves for (a) Hg^+ from Hg, (b) HgCl_2^+ , (c) HgCl^+ , (d) Hg^+ from HgCl_2 and (e) Cl^+ in the region 650-1200 Å

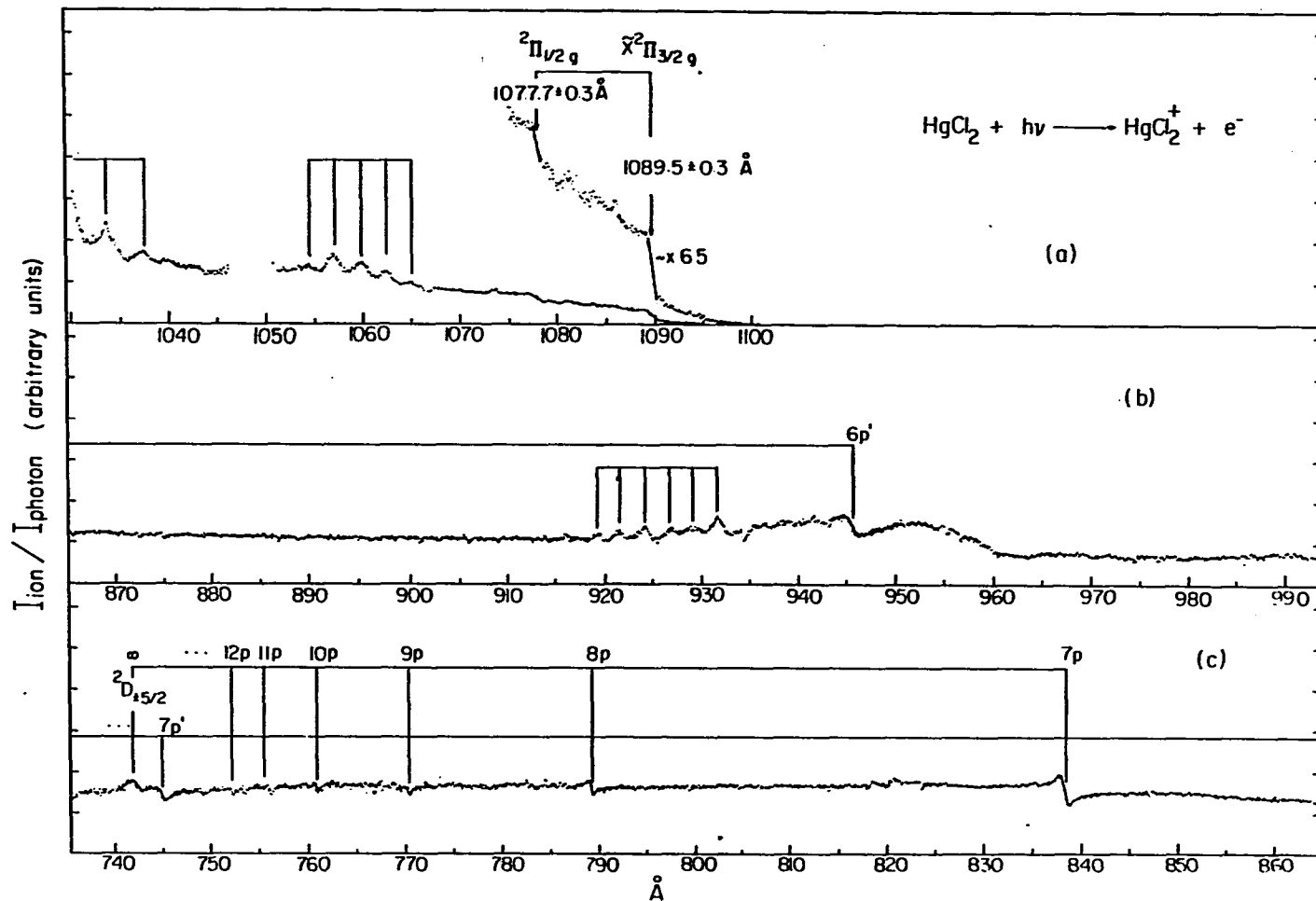


Figure 2. PIE curves (0.14 Å FWHM) for HgCl_2^+ in the regions (a) 1030-1100 Å, (b) 865-995 Å, and 745-865 Å

splitting of the ${}^2\Pi_g$ state. These values were found to be in good agreement with those reported by Eland.³⁹ The magnitude of the spin-orbit splitting is characteristic of the atomic orbital involved. The fact that the spin-orbit splitting for the ${}^2\Pi_g$ states is very close to that of the chlorine atom (0.11 eV)⁴⁹ indicates that the ${}^2\Pi_g$ states of HgCl_2^+ mainly involve the chlorine atoms. The sharp onsets for the spin-orbit states observed here and in the PES for HgCl_2 also show that the ground state of HgCl_2^+ probably has a linear geometry similar to that of HgCl_2 .

The tailing structure found below the IE of HgCl_2 can be attributed to the hot band effects. A break or a change in slope was clearly evident between this tailing structure and the rapidly rising onset for HgCl_2^+ . Since the rotational quanta for HgCl_2 are small and the PIE curve represents the integrated curve for the ionization from all the available rotational states, the effect of high rotational excitation should give rise to a smooth exponential tail at the threshold if a Boltzmann distribution is assumed.⁵⁰ The observed deviation of the threshold from exponential decay is consistent with the expectation that the rotational relaxation in the supersonic expansion is efficient and that the rotational temperature for HgCl_2 attained at the photoionization region is much lower than the nozzle temperature. From the sharpness of the onsets for the $\tilde{X}^2\Pi_{3/2g}$ and ${}^2\Pi_{1/2g}$ states, the rotational temperature for HgCl_2 was estimated to be ~ 35 K. Hence, the finite photoion yield below the IE is due mainly

to vibrational hot band effects. It is known that the relaxation in the supersonic beam for vibrational excitations is less effective than that for rotational excitations.⁵¹ The rapid expansion of a jet results in nonequilibrium between the translational, rotational, and vibrational degrees of freedom. The vibrational temperatures for the ν_1 , ν_2 , and ν_3 modes, which have the frequencies of 363, 75, and 413 cm^{-1} , respectively, should be different. From the ratio of the height of the first step to that of the vibrational hot bands measured in Fig. 2(a), the vibrational temperature for the ν_2 mode was estimated to be ~ 100 K.

Three vibrational progressions were resolved in the PIE curve for HgCl_2^+ [Figs. 1(b), 2(a), and 2(b)]. The positions and analysis of these progressions are summarized in Table I. The average vibrational separation $\Delta\nu_{\text{av}}$ for Progressions I, II, and III was found to be 238, 390, and 289 cm^{-1} , respectively. According to optical selection rules⁵² and by comparing these values with the vibrational frequencies for HgCl_2 in the ground electronic state,⁵² these vibrational progressions probably correspond to the excitation of the ν_1 symmetric vibrational mode of these autoionizing Rydberg states. The observation of long vibrational progressions also reveals that the geometries of the states involved are quite different from that of the ground state of HgCl_2 and might have a bent configuration.

To assist in the assignment of the autoionization structure observed in the PIE curves for HgCl_2^+ and its fragment ions, we have compared them

Table 1. Progressions of absorption bands of HgCl_2

Progression I		Progression II		Progression III	
$\nu(\text{cm}^{-1})$ ($\pm 10 \text{ cm}^{-1}$)	$\Delta\nu(\text{cm}^{-1})$	$\nu(\text{cm}^{-1})$ ($\pm 50 \text{ cm}^{-1}$)	$\Delta\nu(\text{cm}^{-1})$	$\nu(\text{cm}^{-1})$ ($\pm 120 \text{ cm}^{-1}$)	$\Delta\nu(\text{cm}^{-1})$
93889		95950		107339	
	238		417		300
94127		96367 \pm 12		107639	
	240		392		291
94367		96759 \pm 12		107930	
	241		376		303
94608		97135		108233	
	234		378		294
94842		97513		108527	
	---		---		260
---		---		108787	
	$\Delta\nu_{\text{av}} = 238$		$\Delta\nu_{\text{av}} = 390$		$\Delta\nu_{\text{av}} = 289$

with the PIE curve for Hg^+ from atomic mercury [shown in Fig. 1(a)] measured with an optical resolution of 1.4 \AA (FWHM). The latter spectrum, which was obtained in a separate study concerning the photoionization study of mercury clusters, was found to be in excellent agreement with those reported previously.^{22,23} Two of the prominent autoionizing Rydberg series $[(5d)^9(6s)^2 \ ^2D_{5/2}] np, \ ^1P^o$, and $[(5d)^9(6s)^2 \ ^2D_{3/2}] np, \ ^3P^o$, which converge to the $\ ^2D_{5/2}$ and $\ ^2D_{3/2}$ states of Hg^+ , respectively, are also indicated in the figure. The IEs for the $\ ^2D_{\pm 5/2, \pm 3/2, \pm 1/2}$ and $\ ^2D_{\pm 3/2, \pm 1/2}$ states of HgCl_2^+ are blue-shifted by approximately 2 eV with respect to those for the $\ ^2D_{5/2}$ and $\ ^2D_{3/2}$ states of Hg^+ , respectively. These shifts are due to the stronger electron withdrawing character of the chlorine atoms in comparison with the mercury atom in HgCl_2 . The difference in electronegativity between Cl and Hg is expected to give rise to a net positive charge at Hg and thus greater binding energies for electrons in the 5d shell of Hg in HgCl_2 .

Contrary to the sharp peak-like structures found in the PIE curve for Hg^+ from Hg, autoionization features resolved in the HgCl_2^+ spectrum exhibit highly asymmetric and dip-like line profiles. The separation in energy between the pronounced structure at 838.42 \AA (14.79 eV) in the HgCl_2^+ spectrum [Fig. 1(b)] and the peak at 944 \AA (13.13 eV) corresponding to the Rydberg level, $[(5d)^9(6s)^2 \ ^2D_{5/2}] 7p, \ ^1P^o$, of Hg is 1.66 eV. This value was found to be close to the difference (1.88 eV) between the IE of the $\ ^2D_{\pm 5/2}$ state of HgCl_2^+ (16.72 eV) and that of the $\ ^2D_{5/2}$

state of Hg^+ (14.84 eV). As was mentioned earlier, since the $^2D_{\pm 5/2}$ state involves electrons in the $5d_{x^2-y^2}$ and $5d_{xy}$ orbitals lying in a plane perpendicular to the molecular axis of HgCl_2 , which are only slightly perturbed by the ligand field, one expects to find similar Rydberg transitions originating from these orbitals in HgCl_2 . Thus, the structure at 838.42 \AA was fit to the Rydberg equation using the IE of $^2D_{\pm 5/2}$ as the convergence limit. This gives a value of 2.655 for the effective principal quantum number n^* of this autoionizing level as compared to $n^*=2.821$ for the $[(5d)^9(6s)^2 \ ^2D_{5/2}] \ 7p, \ ^1P^o$, atomic Rydberg level. Assuming the principal quantum number n for both levels is 7, one obtains the quantum defects δ equal to 4.34 and 4.18 for the molecular and atomic Rydberg levels, respectively. The slightly larger δ values for Rydberg levels in HgCl_2 can also be explained by the deshielding of the Rydberg electron and increase in the effective positive charge of Hg in HgCl_2 induced by the strong electron withdrawing nature of the chlorine atoms. By using similar δ values, several weaker resonance structures resolved in Figs. 1(b) and 2(c) were identified as members, $n=8, 9$, and 10 of the same Rydberg series converging to the $^2D_{\pm 5/2}$ state. The strength of these resonances diminishes rapidly with the increase of the principal quantum number. This observation is in accordance with the prediction that the width of each resonance is proportional to n^{*-3} . The analysis of this Rydberg series, which is called series I here, is summarized in Table II. Since all autoionizing features have highly asymmetric line profiles which are the results of

Table II. Rydberg Series of HgCl_2 observed in the region 620-1100 \AA

n (p)	E(n) (eV)		n*	δ
	Series I	Series II		
6	11.763 (1054 \AA)	13.117 (945.25 \AA)	1.569	4.431
7	14.788 (838.42 \AA)	16.646 (744.84 \AA)	2.658 2.606	4.342 4.394
8	15.709 (789.24 \AA)	...	3.679	4.321
9	16.095 (770.34 \AA)	...	4.686	4.314
10	16.294 (760.94 \AA)	...	5.687	4.313
Series limit	IE($^2D_{\pm 5/2}$) 16.715 \pm 0.003	IE($^2D_{\pm 3/2, \pm 1/2}$) 18.65 ^a

^aReference 39.

configuration interactions, the resonance energies needed for term series analysis in this paper were obtained by a fitting procedure to be described below. The identification of higher members of series I allows us to deduce a more accurate value for the IE of the ${}^2D_{\pm 5/2}$ state. The value of 16.715 ± 0.003 eV determined in this study is in excellent agreement with that obtained by Eland. Assuming the δ value for the $n=6$ member to be equal to that of the $n=7$ member, the position of the 6p Rydberg level is calculated to be 1054 \AA (11.762 eV). The broad peak-like structure in the vicinity of 1050 \AA observed in the PIE curve for HgCl_2^+ is most likely related to the 6p Rydberg level.

The other prominent structure in the PIE curve for HgCl_2^+ is the dip located at 945.25 \AA (13.117 eV). This dip is superimposed on a strong, broad peak and was found to be blue-shifted by 2.13 eV relative to the strong peak at 1129 \AA (10.98 eV) in the Hg^+ spectrum [Fig. 1(a)]. If one uses arguments similar to those discussed above, because this shift is close to the separation (1.94 eV) between the IEs of the ${}^2D_{\pm 3/2, \pm 1/2}$ states (18.65 eV) of HgCl_2^+ and that of the ${}^2D_{3/2}$ state (16.71 eV) of Hg^+ , the asymmetric dip at 945.25 \AA can be attributed to a member of a Rydberg series converging to the ${}^2D_{\pm 3/2, \pm 1/2}$ state. Including this feature, only two members of this series (series II) are recognizable in the spectrum of HgCl_2^+ . The resonance energies of these members are also listed in Table III. The values for the quantum defects of series I and II were found to decrease gradually as the principal number increases. The observed trend for δ is consistent with the fact that the electron in a high Rydberg orbital is less penetrable to

Table III. Resonances in the PIE curve for HgCl_2^+

Resonances	Γ (eV)	q	E_0 (\AA)
$6p(^2D_{\pm 3/2, \pm 1/2})$	0.022	0.94	945.25
$7p(^2D_{\pm 5/2})$	0.016	0.88	838.42

the ion core than that in a lower member of the same Rydberg series. The good fit attained for series I and II by comparing autoionizing features in the PIE curves for HgCl_2^+ and Hg^+ from Hg show that series I and II can be assigned to transitions

$$[(5d)^{10} \sigma_g^2 \sigma_u^2 \pi_u^4 \pi_g^4] \rightarrow [(5d)^9 \sigma_g^2 \sigma_u^2 \pi_u^4 \pi_g^4 \ ^2D_{\pm 5/2}] np \text{ and}$$

$$[(5d)^{10} \sigma_g^2 \sigma_u^2 \pi_u^4 \pi_g^4] \rightarrow [(5d)^9 \sigma_g^2 \sigma_u^2 \pi_u^4 \pi_g^4 \ ^2D_{\pm 3/2, \pm 1/2}] np, n \geq 6,$$

respectively, which are associated mainly with the mercury atom in HgCl_2 .

This study has not identified autoionizing Rydberg structures corresponding to transitions from the 5d orbitals to f orbitals of Hg in HgCl_2 . The weakness of these structures can be rationalized by the observation that the 5d \rightarrow nf autoionizing Rydberg features found in the PIE curve for Hg^+ from Hg are much weaker than those originating from the 5d \rightarrow np transitions.

An attempt was made to fit the resonance profiles using the Fano line shape formula

$$\sigma(E) = \sigma_c + \sigma_r \frac{(q^2 + 2\epsilon q - 1)}{1 + \epsilon^2} \quad (1)$$

where $\epsilon = (E - E_0)/(\Gamma/2)$, E_0 is the energy of the resonance after perturbation by the continuum, Γ is the width of the resonance, q is the shape parameter, and σ_c and σ_r show the strength of the resonance and the continuum, respectively. The validity and limitation in physical significance of the fitting to resonances observed in molecular photoionization according to Eq. (1) has been discussed extensively by Eland

et al.⁵³ and will not be substantiated here. In accordance with theory and the empirical analysis of resonances resolved in other linear triatomic molecules,⁵³ the values for E_0 and Γ derived by fitting a resonance to Eq. (1) should be the same, irrespective of the ionization channels. Since only the PIE curve for HgCl_2^+ has been obtained in high resolution, the 7p and 6p levels converging to the $^2D_{\pm 5/2}$ and $^2D_{\pm 3/2, \pm 1/2}$ states, respectively, were chosen for careful fittings. The other members of the same series are expected to have the same shape parameter provided the resonances observed arise from effectively single, noninteracting resonances. The values for E_0 , Γ , and q obtained for the $7p(^2D_{\pm 5/2})$ and $6p(^2D_{\pm 3/2, \pm 1/2})$ levels are listed in Table III. Taking the width Γ to be a measure of the lifetime through the uncertainty relationship, the lifetime for the $7p(^2D_{\pm 5/2})$ and $6p(^2D_{\pm 3/2, \pm 1/2})$ levels are estimated to be $\sim 10^{-14}$ s.

Table IV lists the relative intensities of the ions observed in the region 600-1050 Å at 50 Å intervals. The Hg^+ ion is the strongest fragment. The low intensity observed for Cl^+ is partly due to the fact that the measurements made here are in the threshold region of Cl^+ . In this wavelength region, the total intensity of the fragment ions constitutes less than 35% of the HgCl_2^+ parent ion.

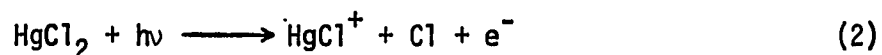
The positions of the resonances for series I and II listed in Table II were used to correlate structures observed in the PIE curves for HgCl^+ and Hg^+ . In general, the correlations are satisfactory. The origin of some new features resolved in the PIE spectra for HgCl^+ and

Table IV. Relative intensities of the fragment ions from HgCl_2

λ (Å)	$I(\text{HgCl}^+)/I(\text{HgCl}_2^+)$	$I(\text{Hg}^+)/I(\text{HgCl}_2^+)$	$I(\text{Cl}^+)/I(\text{HgCl}_2^+)$
1050	0.0038
1000	0.0037
950	0.0145	0.0378	. . .
900	0.0169	0.0366	. . .
850	0.0354	0.0495	. . .
800	0.0276	0.0454	. . .
750	0.0575	0.0823	. . .
700	0.0546	0.1741	0.0039
650	0.0596	0.2287	0.0308
600	0.0668	0.2422	0.0423

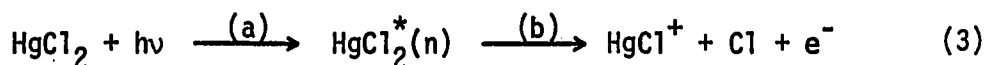
Hg^+ in the regions close to 700 and 740 Å are not known. The shapes of the resonances that appear in the HgCl^+ and Hg^+ spectra are different from those found in the HgCl_2^+ spectrum. Although careful fittings of the resonances observed in the HgCl^+ and Hg^+ spectra have not been carried out, the peak-like appearance of the structures show that the shape parameters, q , for these resonances are greater than one. The larger q values for resonances found in the weaker fragment channels than that in the HgCl_2^+ channel are in agreement with the conclusion arrived at in a systematic examination of resonances found in the PIE curves for other linear molecular ions and their fragments.⁵³ This observation has also been rationalized by Eland *et al.*

The PIE for HgCl^+ was found to decrease dramatically in the region 955-975 Å. Weak signals persist beyond the IE of HgCl_2 . The value of 1123 Å (11.04 eV) indicated in Fig. 1(c) is just the upper bound for the appearance of HgCl^+ . The structures appearing in the region 975-1100 Å in the HgCl_2^+ and HgCl^+ spectra are almost identical. Since the photoionization sampling region is situated in a chamber maintained at a vacuum of $\sim 5 \times 10^{-6}$ Torr, secondary collisional effects should be small. If the weak signals were due to secondary collisional effects and the HgCl^+ formed at wavelengths shorter than ~ 960 Å can be attributed to the reaction

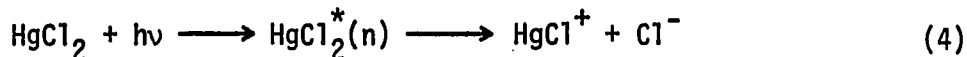


the relative intensities measured at the regions below and above ~ 960 Å should vary as the background pressure at the photoionization region

changes. The PIE curves for HgCl^+ observed in this region at different oven temperatures and carrier gas pressures were found to bear the same relative intensities. Therefore, we believe that secondary processes are not responsible for the formation of HgCl^+ in this region. We note that the PIE curve for HgCl^+ at energies below the IE of HgCl_2^+ displays peak-like structures. If the other fragment involved in the HgCl^+ channel at energies below the IE of HgCl_2^+ is Cl, the reaction can be visualized as a two-step process:



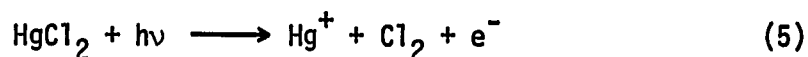
Step 4(a) represents the formation of excited HgCl_2 in some high Rydberg levels followed by a unimolecular dissociation to form $\text{HgCl}^+ + \text{Cl} + e^-$ in step 4(b). The feasibility of process (4) below the IE of HgCl_2 would also imply that the interaction between $\text{HgCl}^+ + \text{Cl}$ in the ground state is repulsive. To the author's knowledge, dissociation processes which involve three particles such as reaction (4) have not been observed previously. The other possible process which may be responsible for the formation of HgCl^+ below the IE of HgCl_2^+ is the ion-pair process



In an electron ionization study by Kiser *et al.*,⁴⁵ they reported that no negative ions observed were identified as being formed in ion-pair processes. The positive identification of the process for HgCl^+ formation near the threshold has to await future studies.

Assuming the rapidly decreasing structure in the region 955-975 Å⁰ to be the threshold region of Reaction (2), an upper bound for the appearance energy (AE) of HgCl⁺ by Reaction (2) is estimated at ~975 Å⁰ (12.72 eV). By using the latter value, together with the known values, -34.0±1.5 and 28.52±0.03 kcal/mol^{54,55} for the heats of formation for HgCl₂ and Cl at 0 K, respectively, the heat of formation for HgCl⁺ is calculated to be ~231 kcal/mol.

The AE for the formation of Hg⁺ from HgCl₂ was determined to be 12.59±0.02 eV (984.5 Å⁰). This value is in excellent agreement with the calculated thermochemical threshold (12.58±0.2 eV) from known thermodynamical data^{54,55} from the reaction



As shown in Fig. 1(e), the AE for the Cl⁺ formation from HgCl₂ was found to be 16.72±0.07 eV (941.5±3 Å⁰). Assuming the neutral fragment involved is HgCl, the latter value, along with known thermochemical data for Cl⁺ ($\Delta H_{f0}^\circ = 328.7 \pm 0.5$ kcal/mol)⁵⁵ and HgCl₂, allows the calculation of a value of 22.8±2.2 kcal/mol for $\Delta H_{f0}^\circ(\text{HgCl})$. This value is also in agreement with the literature value [$\Delta H_{f0}^\circ(\text{HgCl}) = 19.7 \pm 2.3$ kcal/mol].⁵⁴ Using $\Delta H_{f0}^\circ(\text{HgCl})$ determined in this study and the known $\Delta H_{f0}^\circ(\text{Hg})$ (15.41±0.15 kcal/mol)⁵⁴ and $\Delta H_{f0}^\circ(\text{Cl})$, the bond dissociation energy for HgCl was deduced to be 21.1±2.2 kcal/mol, which was found to be consistent with those reported previously.^{9,56,57}

SUMMARY AND CONCLUSION

The energetics of the photoionization and photodissociative ionization processes of HgCl_2 determined in this study are summarized and compared with those reported previously in Table V. With proper optimization of experimental conditions, we have successfully operated a supersonic oven source for HgCl_2 and obtained high resolution PIE data for HgCl_2^+ and its fragments. Although the study of the fragmentation processes from HgCl_2 dimers has not been included here because of the limitation in the mass range of our mass spectrometer, the photoionization study of dimer and clusters of metal compounds synthesized in a supersonic expansion is a potentially useful method to obtain energetic and bonding information for metal cluster compounds.

Table V. Summary of photoionization data for HgCl₂

Ion	AE or IE (eV)	Process
HgCl ₂ ⁺ ($\tilde{X}^2\Pi_{3/2g}$)	11.38±0.003 ^a 11.37 ^b	HgCl ₂ + hν → HgCl ₂ ⁺ ($\tilde{X}^2\Pi_{3/2g}$) + e ⁻
HgCl ₂ ⁺ ($^2\Pi_{1/2g}$)	11.504 ₅ ±0.003 ^a 11.50 ^b	HgCl ₂ + hν → HgCl ₂ ⁺ ($^2\Pi_{1/2g}$) + e ⁻
HgCl ₂ ⁺ ($^2D_{\pm 5/2}$)	16.715±0.003 ^a 16.72 ^b	HgCl ₂ + hν → HgCl ₂ ⁺ ($^2D_{\pm 5/2}$) + e ⁻
HgCl ⁺	< 12.72 ^a 12.06±0.26 ^c	HgCl ₂ + hν → HgCl ⁺ + Cl + e ⁻
Hg ⁺	12.59±0.020 ^a	HgCl ₂ + hν → Hg ⁺ + Cl ₂ + e ⁻
Cl ⁺	16.72±0.030 ^a 17.7±0.3 ^c	HgCl ₂ + hν → Cl ⁺ + HgCl + e ⁻

^aThis work.

^bReference 39.

^cReference 45.

REFERENCES

1. J. Berkowitz, "Photoabsorption, Photoionization, and Photoelectron Spectroscopy" (Academic, New York, 1979).
2. J. Berkowitz and W. A. Chupka, J. Chem. Phys. 45, 1287 (1966).
3. J. Berkowitz and T. A. Walter, J. Chem. Phys. 49, 1184 (1968).
4. J. Berkowitz and C. Lifshitz, J. Chem. Phys. 48, 4346 (1968).
5. J. Berkowitz and W. A. Chupka, J. Chem. Phys. 50, 4245 (1968).
6. J. Berkowitz, J. Chem. Phys. 50, 3503 (1969).
7. J. Berkowitz, Adv. High Temp. Chem. 3, 123 (1971).
8. H. Pauly and J. P. Toennies in "Methods of Experimental Physics", Vol. 7A, edited by B. Bederson and W. L. Fite (Academic, New York, 1968), p. 227.
9. W. R. Wadt, J. Chem. Phys. 72, 2469 (1980).
10. J. Maya, J. Chem. Phys. 67, 4976 (1977).
11. H. Hofmann and S. R. Leone, J. Chem. Phys. 68, 3819 (1978).
12. J. Husain, J. R. Wiesenfeld, and R. N. Zare, J. Chem. Phys. 72, 2479 (1980).
13. J. H. Parks, App. Phys. Lett. 31, 192 (1977).
14. J. G. Eden, App. Phys. Lett. 31, 448 (1977).
15. J. H. Parks, Appl. Phys. Lett. 31, 297 (1977).
16. E. J. Schimitschek and J. E. Celto, Opt. Lett. 2, 64 (1978).
17. R. L. Burnham, Appl. Phys. Lett. 33, 156 (1978).
18. W. T. Whitney, Appl. Phys. Lett. 32, 239 (1978).

19. K. Y. Tang, R. O. Hunter, Jr., J. Oldenettel, C. Howton, D. Huestis, D. Eckstrom, B. Perry, and M. McCusker, *Appl. Phys. Lett.* 32, 226 (1978).
20. E. J. Schimitschek, J. E. Celto, and J. A. Trias, *Appl. Phys. Lett.* 31, 608 (1977).
21. J. G. Eden, *Appl. Phys. Lett.* 33, 495 (1978).
22. J. Berkowitz and C. Lifshitz, *J. Phys. B* 1, 438 (1968).
23. B. Brehm, *Z. Naturforsch.* 212, 196 (1966).
24. U. Fano, *Nuovo Cimento* 12, 156 (1935).
25. H. Beulter, *Z. Phys.* 93, 177 (1935).
26. U. Fano, *Phys. Rev. A* 1, 1976 (1961).
27. U. Fano and J. W. Cooper, *Phys. Rev. Sect. A* 137, 1364 (1965).
28. U. Fano and J. W. Cooper, *Rev. Mod. Phys.* 40, 441 (1968).
29. J. N. Bardsley, *Chem. Phys. Lett.* 2, 329 (1968).
30. A. L. Smith, *J. Quant. Spectrosc. Radiat. Transfer* 10, 1129 (1970).
31. A. F. Starace, *Phys. Rev. A* 16, 231 (1977).
32. P. C. Kemeny, J. A. R. Samson, and A. F. Starace, *J. Phys. B* 10, L201 (1977).
33. D. L. Ederer, *Phys. Rev. A* 4, 2263 (1971).
34. D. L. Ederer, *Phys. Rev. A* 14, 1936 (1976).
35. M. J. Seaton, *Proc. Phys. Soc. London* 88, 801 (1966).
36. K. T. Lu, *Phys. Rev. Lett.* 33, 123 (1974).
37. U. Fano, *J. Opt. Soc. Am.* 65, 979 (1975).
38. F. H. Mies, *Phys. Rev.* 175, 164 (1968).

39. J. H. D. Eland, *Int. J. Mass Spectrom. Ion Phys.* 4, 37 (1970).
40. R. G. Egde11, A. F. Orchard, D. R. Lloyd, and N. Y. Richardson, *J. Electron Spectros. Rel. Phenom.* 12, 415 (1977).
41. K. Witte1, B. S. Mohanty, and R. Manne, *J. Electron Spectrosc. Rel. Phenom.* 5, 1115 (1974).
42. L. C. Cusachs, F. A. Grimm, and Geo. K. Schweitzer, *J. Electron Spectrosc. Rel. Phenom.* 3, 229 (1974).
43. S. Evans and A. F. Orchard, *J. Electron Spectrosc. Rel. Phenom.* 6, 207 (1975).
44. J. Berkowitz, *J. Chem. Phys.* 61, 407 (1974).
45. R. W. Kiser, J. G. Dillard, and D. L. Dugger, "Advances in Chemistry Series", Vol. 72 (American Chemical Society, Washington, D.C., 1968), p 153.
46. S. H. Linn and C. Y. Ng, Iowa State University, Ames, IA, to be published.
47. Y. Ono, S. H. Linn, H. F. Prest, M. E. Gress, and C. Y. Ng, *J. Chem. Phys.* 73, 2523 (1980).
48. K. E. Schubert and R. D. Hudson, "A Photoelectric Atlas of the Intense Lines of the Hydrogen Molecular Emission Spectrum from 1025 to 1650 Å at a Resolution of 0.10 Å", Report Number ATN-64 9233)-2, Aerospace Corp., Los Angeles, 1963.
49. C. E. Moore, "Atomic Energy Levels", Vol. 1, Natl. Bur. Std. Circular No. 467 (U. S. Government Printing Office, Washington D. C., 1949).
50. P. M. Guyon and J. Berkowitz, *J. Chem. Phys.* 54, 1814 (1971).

51. J. B. Anderson in "Molecular Beams and Low Density Gasdynamics", edited by P. P. Wegener (Marcel Dekker, New York, 1974), p. 1.
52. G. Herzberg, "Molecular Spectra and Molecular Structure III: Electronic Spectra and Electronic Structure of Polyatomic Molecules" (Van Nostrand, Princeton, N.J., 1966).
53. J. H. D. Eland, J. Berkowitz, and J. E. Monohan, J. Chem. Phys. 72, 253 (1980).
54. "JANAF Thermochemical Tables", Natl. Stand. Ref. Data Ser. 37, Natl. Bur. Stand., June 1971.
55. H. M. Rosenstock, K. Draxl, B. W. Steiner, J. T. Heron, J. Phys. and Chem. Ref. Data 6, Suppl. 1 (1977).
56. K. P. Huber and G. Herzberg, "Molecular Spectra and Molecular Structure IV: Constants of Diatomic Molecules" (Van Nostrand Reinhold, New York, 1979).
57. R. E. Wilcomb and R. B. Bernstein, J. Mol. Spectrosc. 62, 442 (1976).

SECTION II.

MOLECULAR BEAM PHOTOIONIZATION STUDY
OF HgBr_2 AND HgI_2

ABSTRACT

Photoionization efficiency (PIE) data for HgBr_2^+ and HgI_2^+ and their fragment ions have been obtained in the region 600-1350 Å using an oven-type supersonic beam source. The ionization energies (IE) for the $\chi^2\Pi_{3/2g}$ states of HgBr_2^+ and HgI_2^+ were determined to be 10.560 ± 0.003 and 9.5088 ± 0.0022 eV, respectively. The analyses of the Rydberg series converging to the $^2\Pi_{1/2g}$ states of HgBr_2^+ and HgI_2^+ yield a value of 10.8846 ± 0.0012 eV for the IE of the $^2\Pi_{1/2g}$ state of HgBr_2^+ and 10.1953 ± 0.0025 eV for that of HgI_2^+ . The major fragment ions from HgBr_2 were identified to be HgBr^+ , Hg^+ , Br_2^+ , and Br^+ and those from HgI_2 were found to be HgI^+ , I_2^+ , and I^+ . The measured appearance energies for HgBr^+ and HgI^+ allow the calculation of the bond dissociation energies for HgBr^+ and HgI^+ to be 55 ± 2 and 59 ± 1 kcal/mol, respectively. Similar to the observation in the PIE curves for HgCl_2^+ and its fragment ions, the PIE spectra for HgBr_2^+ , HgI_2^+ and their fragment ions are dominated by autoionization structures exhibiting asymmetric Beutler-Fano line profiles. The comparison of the PIE curves of HgCl_2^+ , HgBr_2^+ , HgI_2^+ , and Hg^+ from Hg confirms the previous conclusion that these autoionizing Rydberg series can be assigned to transitions $[(5d)^{10}\sigma_g^2\sigma_u^2\pi_u^4\pi_g^4] \rightarrow [(5d)^9\sigma_g^2\sigma_u^2\pi_u^4\pi_g^4 \ ^2D_{\pm 5/2}] np$ and $[(5d)^{10}\sigma_g^2\sigma_u^2\pi_u^4\pi_g^4] \rightarrow [(5d)^9\sigma_g^2\sigma_u^2\pi_u^4\pi_g^4 \ ^2D_{\pm 3/2, \pm 1/2}] np$, $n \geq 6$, which are mainly associated with the mercury atom in HgX_2 , $X = \text{Cl}, \text{Br}, \text{and I}$.

INTRODUCTION

The electronic structures of the mercuric halides, HgX_2 , $X = \text{Cl}$, Br , and I , have been studied by photoelectron spectroscopy.¹⁻⁶ An early electron impact study of HgX_2 was reported by Kiser et al. in 1966.⁷ Extensive investigations concerning the photoabsorption, photo-fragmentation, and emission processes induced by irradiating the mercuric halides with vacuum ultraviolet (VUV) and ultraviolet (UV) light were performed over fifty years ago mostly by Terenin⁸ and Wieland.^{9,10} The current interest¹¹⁻¹⁴ in the understanding of the UV and VUV chemistry of HgX_2 is motivated by the development of the mercury halide lasers.¹⁵⁻¹⁹

All the previous photoabsorption and photofragmentation work on HgX_2 was limited to wavelengths longer than 1500 \AA . Recently, in our laboratory, in an effort to obtain high resolution photoionization spectra of higher temperature vapors, Linn et al.²⁰ have determined the relative cross sections for the formations of HgCl_2^+ , HgCl^+ , Hg^+ , and Cl^+ from HgCl_2 in the region $600\text{-}1300 \text{ \AA}$. From the measured appearance energies (AE) of HgCl and HgCl^+ , they have been able to estimate the bond dissociation energies of HgCl and HgCl^+ . This report presents the results and analysis of a similar study on HgBr_2 and HgI_2 . The comparison of PIE data of the HgCl_2 , HgBr_2 , and HgI_2 has been instructive in the assignments of Rydberg features resolved in the PIE spectra in the region $600\text{-}1350 \text{ \AA}$.

DESIGNATION OF ELECTRONIC STATES FOR HgX_2^+

According to the HeI (584 Å) photoelectron spectroscopic study of HgX_2 , these linear, symmetric molecules have an orbital sequence $\cdots 5d^{10} \sigma_g^2 \sigma_u^2 \pi_u^4 \pi_g^4$.¹ Upon ionization from the four valence orbitals, the ionic states formed are the ${}^2\Pi_{3/2g}$, ${}^2\Pi_{1/2g}$, ${}^2\Pi_{3/2u}$, ${}^2\Sigma_u^+$, and ${}^2\Sigma_g^+$ states. The removal of an electron from the full $5d^{10}$ shell of the mercury atom gives rise to the ${}^2D_{5/2}$ and ${}^2D_{3/2}$ states for Hg^+ . Eland¹ points out that since the spin-orbit splitting in Hg^+ is large, the interactions of the ${}^2D_{5/2}$ and ${}^2D_{3/2}$ states with the cylindrical symmetry molecular field in HgX_2 are similar to the expected of a weak field Stark effect. The ${}^2D_{5/2}$ state should be split into three components of equal statistical weight, $\pm 5/2$, $\pm 3/2$, and $\pm 1/2$, and the ${}^2D_{3/2}$ state should be split into $\pm 3/2$ and $\pm 1/2$. The designation of electronic states of HgX_2^+ will follow those used by Eland.

EXPERIMENTAL

The experimental procedures and arrangement are similar to those described previously.^{20,21} Briefly, the apparatus consists of a windowless 3-m near normal incidence VUV monochromator (McPherson 2253 M), an oven-type supersonic beam production system, a capillary discharge light source, and a quadrupole mass filter for ion detection. The grating employed in this study was a Bausch and Lomb 1200 lines/mm MgF_2 coated aluminum grating blazed at 1360 \AA . The hydrogen many-lined pseudocontinuum, the argon continuum or the helium Hopfield continuum was used as the light source depending on the wavelength region desired.

In principle, the oven beam source used is a two-stage oven.²⁰ By maintaining the second stage (the nozzle) at a slightly higher temperature than that of the first stage (the main oven), a stable beam of HgX_2 could be obtained. Most of the data presented in this work were taken with the temperatures of the main oven and nozzle at ~ 470 and 510 K , respectively. In a typical run, the fluctuation in the oven and nozzle temperatures was less than $\pm 3 \text{ K}$ as monitored with thermocouples. Due to the corrosive nature of the gaseous HgX_2 sample, the clogging of the nozzle became a serious problem when the oven and nozzle were operated at higher temperatures. To maintain the oven and nozzle at the lowest possible temperature for the experiment was also desirable in some runs to minimize the effect of thermal dissociations of HgBr_2 and HgI_2 .

The HgBr_2 and HgI_2 used in this study were obtained from Fisher Scientific Company and Alfa Products. Both compounds are stated to be $\geq 99\%$ pure and were used without further purification. Helium was used as the carrier gas. The carrier gas pressure, which was maintained in the range of ~ 150 to 400 Torr, was higher than the vapor pressure of the sample at a given oven temperature.

The major ions from HgBr_2 were found to be HgBr_2^+ , HgBr^+ , Hg^+ , Br_2^+ , and Br^+ . Table I lists the relative intensities of these ions observed in the range 600–1050 Å at 50 Å intervals. At wavelengths longer than 750 Å, HgBr^+ is the strongest fragment. However, at wavelengths shorter than 650 Å, Br^+ becomes the dominant species. In the case of HgI_2 , HgI_2^+ , HgI^+ , I_2^+ , and I^+ were observed. A careful search for the Hg^+ ion was made. The PIE curve obtained for Hg^+ was found to be characteristic of that for the mercury atom, possibly produced by the thermal dissociation of HgI_2 . The wavelength dependence measurements of the relative intensities of HgI_2^+ , HgI^+ , I_2^+ , and I^+ were not made. The branching ratio at 850 Å for HgI_2^+ : HgI^+ : I_2^+ : I^+ was found to be $\sim 70:9:1.7:1$.

With the exception of a small section of the Br_2^+ spectrum in the range 600–725 Å, which was taken and plotted at intervals of 1 Å, all the low resolution (1.4 Å FWHM) spectra were taken and plotted at intervals of 0.5 Å. The high resolution (0.14 Å FWHM) spectra for HgBr_2^+ and HgI_2^+ were taken and plotted at intervals of 0.1 Å. The standard deviations for PIE data obtained in this experiment are in general better than $\pm 10\%$.

Table I. Relative intensities of the fragment ions from HgBr_2

$\lambda(\text{\AA})$	$I(\text{HgBr}^+)/I(\text{HgBr}_2^+)$	$I(\text{Hg}^+)/I(\text{HgBr}_2^+)$	$I(\text{Br}_2^+)/I(\text{HgBr}_2^+)$	$I(\text{Br}^+)/I(\text{HgBr}_2^+)$
1000	0.019	0.013
950	0.059	0.018	0.002	...
900	0.114	0.022	0.007	...
850	0.105	0.023	0.005	...
800	0.138	0.048	0.004	0.002
750	0.145	0.090	0.005	0.010
700	0.130	0.158	0.006	0.092
650	0.129	0.158	0.007	0.160
600	0.250	0.185	0.016	0.320

All of the PIE spectra presented here are based on a minimum of two reproducible scans. The wavelength scales were calibrated by using known atomic resonance lines or H₂ emission lines²² when the H₂ pseudocontinuum was used.

RESULTS AND DATA ANALYSIS

Mercuric Bromide



Figure 1(a) shows the PIE curve for HgBr_2^+ in the range 600-1200 Å obtained using a wavelength resolution of 1.4 Å (FWHM). The high resolution (0.14 Å) data in the ranges 1035-1190 Å and 695-995 Å obtained using the argon and helium Hopfield continua, respectively, as the light sources, are plotted in Figs. 2(a), 2(b), and 2(c). The IE's for the electronic states of HgBr_2^+ in this region determined by photoelectron spectroscopy¹ are indicated by arrows in the PIE curve for HgBr_2^+ in Fig. 1(a). No apparent structure correlating to the onsets of these states can be seen with the exception of that for the $\tilde{X}^2\Pi_{3/2g}$ state where a sharp steplike feature was found. The position of this step was located at 1174.1 Å with an uncertainty of 0.3 Å in the high resolution PIE curve for HgBr_2^+ [Fig. 2(a)]. Accordingly, the IE of the $\tilde{X}^2\Pi_{3/2g}$ state was determined to be 10.560 ± 0.003 eV. This value was found to be slightly lower than that reported by Eland.¹

The tailing structure found below the IE can be attributed to vibrational hot band effects. Similar to the observation in the high resolution PIE spectrum for HgCl_2^+ , a break or change in slope is clearly evident between this tailing structure and the rapidly rising onset for HgBr_2^+ .²⁰ As was pointed out previously, the observed deviation of the threshold from exponential decay is consistent with the

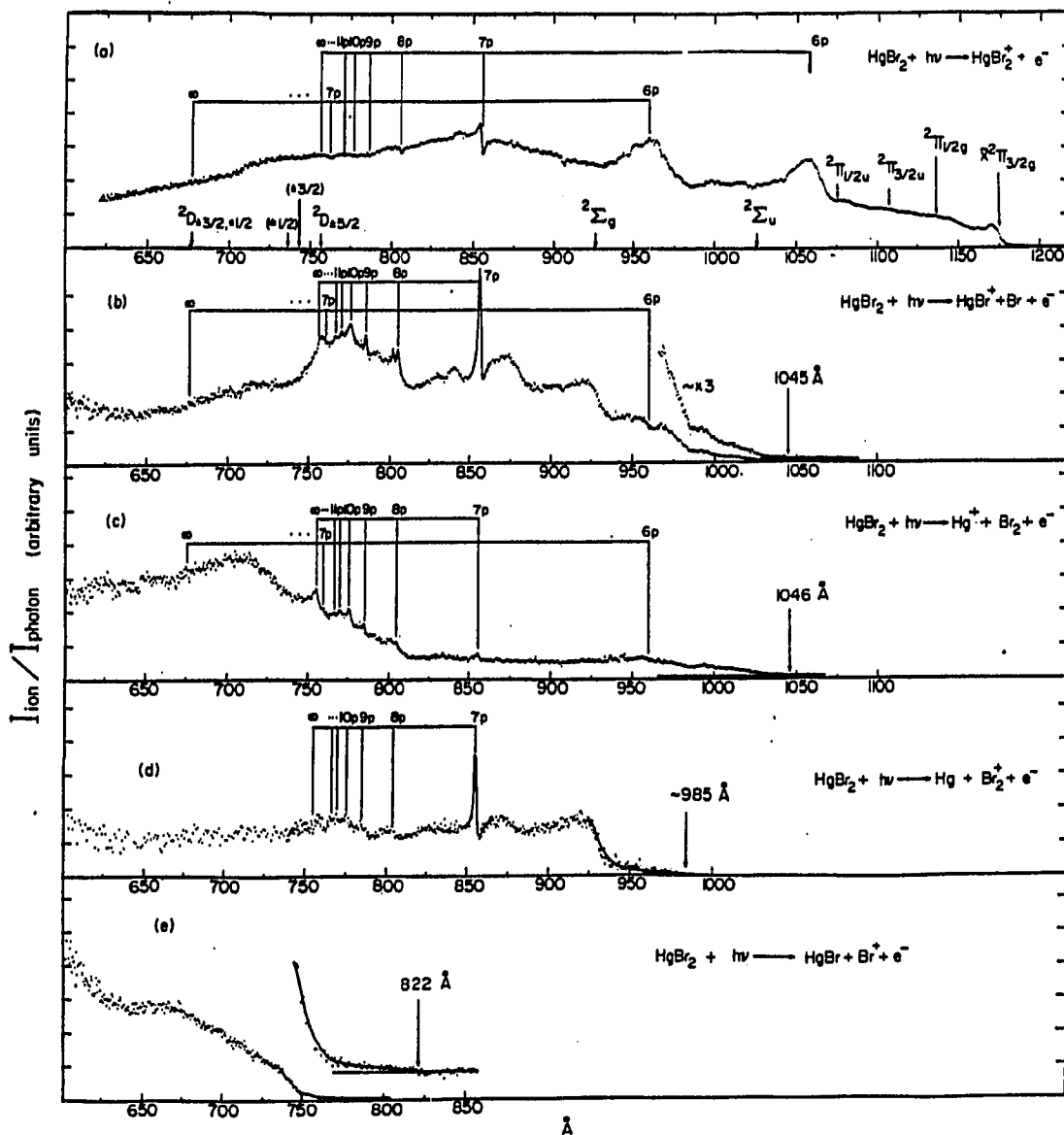


Figure 1. PIE curves for (a) HgBr_2^+ , (b) HgBr^+ , (c) Hg^+ , (d) Br_2^+ , and (e) Br^+ in the region 600-1200 Å

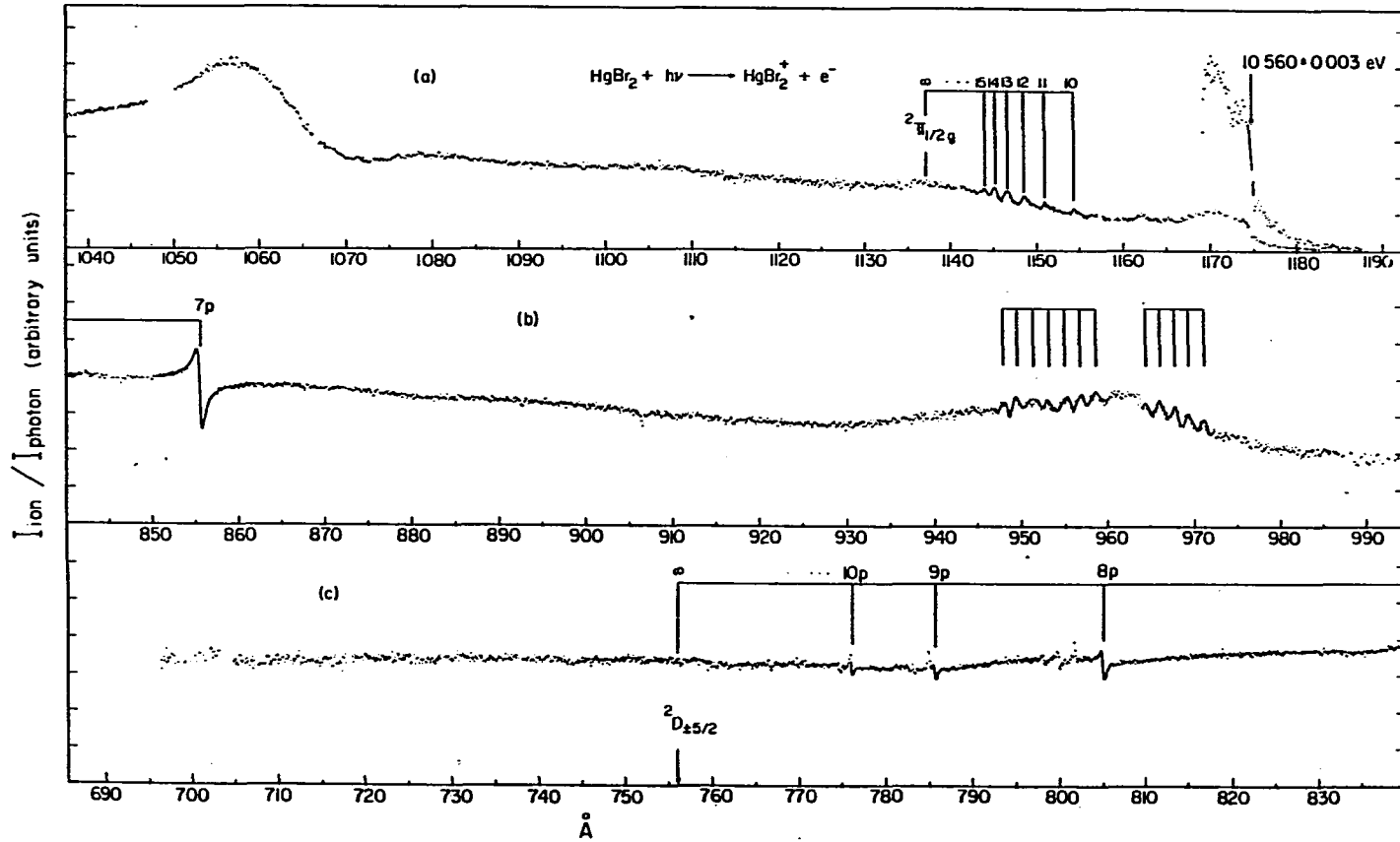


Figure 2. PIE curves (0.14 \AA FWHM) for HgBr_2^+ in the regions (a) $1037\text{-}1190 \text{ \AA}$, (b) $840\text{-}995 \text{ \AA}$, and (c) $690\text{-}840 \text{ \AA}$

expectation that the rotational temperature for HgBr_2 attained at the photoionization region after the supersonic expansion is much lower than the nozzle temperature (~ 510 K). From the sharpness of the onset for the $\tilde{X}^2\Pi_{3/2g}$ state, the rotational temperature was estimated to be ~ 35 K.

Instead of a sharp steplike structure found at the IE for the $^2\Pi_{1/2g}$ state of HgCl_2^+ ,²⁰ only a small kink can be seen [Fig. 1(a)] at the onset of the $^2\Pi_{1/2g}$ state of HgBr_2^+ . The high resolution spectrum for HgBr_2^+ [Fig. 2(a)] reveals autoionizing features in the region between the onsets of the $\tilde{X}^2\Pi_{3/2g}$ and $^2\Pi_{1/2g}$ states. The observed positions (ν_{obs}) of these autoionizing Rydberg structures were found to be in excellent agreement with the positions (ν_m) calculated by the Rydberg equation

$$\nu_m = \left[87990 - \frac{R}{(m-0.809)^2} \right] \text{ cm}^{-1} \quad (1)$$

where R and m are the Rydberg constant and the nominal principal quantum number, respectively. The observed and calculated positions of this series are compared in Table II. The maximum deviation of ν_m from ν_{obs} is less than 10 cm^{-1} . Since the convergence limit, $87990 \pm 10 \text{ cm}^{-1}$ ($10.8846 \pm 0.0012 \text{ eV}$) was found to be close to the vertical IE (10.96 eV)¹ for the $^2\Pi_{1/2g}$ state obtained by Eland, it was assigned to be the adiabatic IE for the $^2\Pi_{1/2g}$ state of HgBr_2^+ .

Two vibrational progressions were resolved in the high resolution PIE curve for HgBr_2^+ [Fig. 2(b)]. The positions of these autoionizing

Table II. Rydberg series converging to the $^2\Pi_{1/2g}$ threshold of HgBr_2^+

$$\nu_m = 87990 - \frac{R}{(m-0.809)^2}$$

n	$\nu_{\text{obs}} (\text{cm}^{-1}) (\pm 10 \text{cm}^{-1})$	$\nu_m (\text{cm}^{-1})$
10	86685 (1153.6 Å)	86691
11	86934 (1150.3 Å)	86934
12	87116 (1147.9 Å)	87114
13	87252 (1146.1 Å)	87252
14	87367 (1144.6 Å)	87359
15	87451 (1143.5 Å)	87445

$\text{IE}(^2\Pi_{1/2g}) = 87790 \pm \text{cm}^{-1}$

Rydberg vibrational levels are listed in Table III. The average vibrational separations $\Delta\nu_{av}$ for Progression I and II were found to be 176 and 200 cm^{-1} , respectively. According to optical selection rules,²³ these vibrational progressions probably correspond to the excitation of the ν_1 symmetric stretching vibrational mode of the autoionizing Rydberg states. We note that the frequency (229 cm^{-1})²⁴ of the ν_1 mode of HgBr_2 in the ground electronic state is slightly higher than the values of $\Delta\nu_{av}$.

Except for minor details, the PIE curve for HgBr_2^+ is very similar to that for HgCl_2^+ .²⁰ Rydberg structures observed in the PIE spectrum for HgBr_2^+ were found to be red-shifted by ~ 0.3 eV with respect to the corresponding structures appearing in the HgCl_2^+ spectrum. The red-shift of ~ 0.3 eV is approximately equal to the corresponding differences between the IEs of the $^2D_{\pm 5/2}$ and $^2D_{\pm 3/2, \pm 1/2}$ states of HgBr_2^+ and those of HgCl_2^+ . Therefore, using similar arguments to those discussed previously, these Rydberg structures were assigned to members of Rydberg series converging to the $^2D_{\pm 5/2}$ (16.40 eV) and $^2D_{\pm 3/2, \pm 1/2}$ (18.34 eV) states of HgBr_2^+ . Analysis of these Rydberg series, which are called series I and II here, are summarized in Table IV.

Most of the autoionizing features exhibit highly asymmetric Beulter-Fano line profiles^{25,26} which are the results of configuration interactions.²⁷⁻⁴⁰ When possible, the resonance energies listed in Table IV were determined by a fitting procedure used previously by Eland *et al.*⁴¹ to parameterize resonances observed in PIE curves of some linear

Table III. Progressions of absorption bands of HgBr₂

Progression I		Progression II	
ν (cm ⁻¹) (± 11 cm ⁻¹)	$\Delta\nu$ (cm ⁻¹)	ν (cm ⁻¹) (± 12 cm ⁻¹)	$\Delta\nu$ (cm ⁻¹)
102986		104307	
	180		196
103166		104503	
	171		197
103337		104700	
	180		231
103517		104931	
	173		187
103690		105118	
	...		209
...		105327	
	...		179
...		105506	
	$\Delta\nu_{av} = 176$		$\Delta\nu_{av} = 200$

Table IV. Rydberg series converging to the ${}^2D_{\pm 5/2}$ and ${}^2D_{\pm 3/2, \pm 1/2}$ limits of HgBr_2^+

n(p)	E(n) (eV)		n* ^c	δ^d
	Series I	Series II		
6	~ 11.719 (1059 Å)		~ 1.70	4.30
		12.93 (959 Å)	1.59	4.41
7	14.498 (855.2 Å)		2.678	4.322
		16.29 (761 Å)	2.58	4.42
8	15.404 (804.9 Å)		3.702	4.298
	
9	15.780 (785.7 Å)		4.699	4.301
	
10	15.978 (776.0 Å)		5.700	4.300
	
11	16.092 (770.5 Å) ^a		6.68	4.32
	
12	16.165 (767.0 Å) ^a		7.66	4.34
	
Series limit	IE (${}^2D_{\pm 5/2}$) = 16.397 \pm 0.003	IE (${}^2D_{\pm 3/2, \pm 1/2}$) = 18.34 ^b		

^aThe positions of these two resonances were determined by peak-line structures observed in the PIE curves for HgBr^+ and Hg^+ .

^bReference 1.

^cEffective principal quantum number.

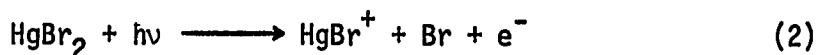
^dQuantum defect.

triatomic molecular systems. The assignment of the principal quantum number (n) for these Rydberg levels follows from the conclusion of the analysis of photoionization data for HgCl_2^{+20} and will be discussed in a later section. The resonance energies for the members, $n = 6$, of series I and II were only estimated by their peak positions. Members $n = 11$ and 12 are not evident in the PIE curve for HgBr_2^+ . The positions of these two resonances were determined by peaklike structures observed in the PIE curves for HgBr^+ and Hg^+ . The precise identification of higher members, $n = 7, 8, 9$, and 10 of series I allows the deduction of a more accurate value for the IE of the $^2D_{\pm 5/2}$ state of HgBr_2^+ . The value of 16.397 ± 0.003 eV determined in this study is in excellent agreement with that obtained in a photoelectron spectroscopic study.¹

HgBr^+

The PIE curve for HgBr^+ from HgBr_2 in the region 600-1100 Å obtained using a wavelength resolution of 1.4 Å is shown in Fig. 1(b). The positions of autoionizing resonances (Table IV) identified in the PIE curve for HgBr_2^+ were used to correlate the structures appearing in the HgBr^+ spectrum. The correlation was found to be excellent. However, other than a diplike line profile found at the $n = 6$ member of series II, all the resonances have sharper peaklike profiles than those observed in the HgBr_2^+ spectrum.

The AE for HgBr^+ from HgBr_2 was determined to be $1045 \pm 3 \text{ \AA}$ ($11.86 \pm 0.03 \text{ eV}$). Assuming the reaction

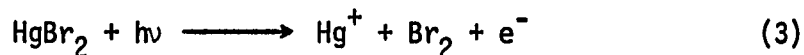


to be responsible for the formation of HgBr^+ and by using the known values for the heats of formation of HgBr_2 [$\Delta H^\circ_{f0}(\text{HgBr}_2) = 16.07 \pm 2 \text{ kcal/mol}$]⁴² and Br [$\Delta H^\circ_{f0}(\text{Br}) = 28.20 \pm 0.07 \text{ kcal/mol}$]⁴², the AE of HgBr^+ determined here makes possible the calculation of a value for $\Delta H^\circ_{f0}(\text{HgBr}^+)$ of $229 \pm 2 \text{ kcal/mol}$.⁴³ Since $\Delta H^\circ_{f0}(\text{HgBr}^+)$ is equal to the sum of the IE and the heat of formation of HgBr [$\Delta H^\circ_{f0}(\text{HgBr}) = 27.6 \pm 9 \text{ kcal/mol}$]⁴², a value for the IE of HgBr was estimated to be $8.73 \pm 0.39 \text{ eV}$. Using the known value for the heat formation of Hg^+ [$\Delta H^\circ_{f0}(\text{Hg}^+) = 256.1 \pm 0.23 \text{ kcal/mol}$]⁴⁴, $\Delta H^\circ_{f0}(\text{Br})$, and $\Delta H^\circ_{f0}(\text{HgBr}^+)$, the bond dissociation energy of HgBr^+ [$D_0(\text{HgBr}^+)$] was deduced to be $55 \pm 2 \text{ kcal/mol}$ ($2.39 \pm 0.09 \text{ eV}$).

Hg^+

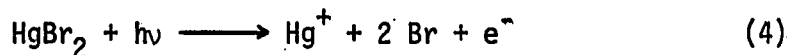
The PIE curve for Hg^+ from HgBr_2 in the region $600\text{-}1070 \text{ \AA}$ obtained using a wavelength resolution of 1.4 \AA (FWHM) is shown in Fig. 1(c). As in the PIE curve of HgBr^+ , autoionizing features observed in the Hg^+ spectrum also have peaklike appearances. In general, these structures seem to be weaker than those found in the PIE curve for HgBr^+ .

The AE for Hg^+ from HgBr_2 was determined to be $1046 \pm 3 \text{ \AA}$ ($11.85 \pm 0.03 \text{ eV}$). This value was found to be in good agreement with the thermochemical threshold ($11.80 \pm 0.09 \text{ eV}$) for the process



calculated by using the known values of $\Delta H^\circ_{f0}(\text{HgBr}_2)$ and $\Delta H^\circ_{f0}(\text{Hg}^+)$. Since the fragmentation of HgBr_2 to form $\text{Hg}^+ + \text{Br}_2$ is likely to be preceded by the ionization of HgBr_2 , this observation may mean the activation energy for the unimolecular decomposition of HgBr_2^+ to form $\text{Hg}^+ + \text{Br}_2$ is zero.

The thermochemical threshold for the process

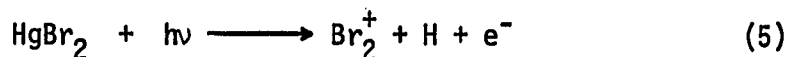


is 14.25 eV (870 \AA). This process may be responsible for the dramatic increase in PIE for Hg^+ at wavelengths shorter than $\sim 810 \text{ \AA}$.

Br_2^+

The Br_2^+ ion is the weakest fragment ion from HgBr_2 . The PIE curve for Br_2^+ in the region $\sim 600\text{--}1000 \text{ \AA}$ obtained using a wavelength resolution of 1.4 \AA (FWHM) is shown in Fig. 1(d). The autoionizing features appearing in the Br_2^+ spectrum are similar to those observed in the PIE curve for HgBr^+ . The rise in the threshold of Br_2^+ is very gradual. At approximately 985 \AA (12.59 eV), the Br_2^+ signal was found to drop within the noise level. Thus, the upper bound for the AE of Br_2^+ from HgBr_2 was determined to be 12.59 eV . This value is slightly

higher than the thermochemical threshold (12.34 ± 0.09 eV) for the process



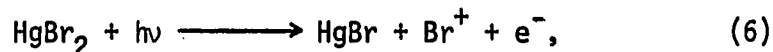
calculated by using known thermodynamical data for $\text{Br}_2^+[\Delta H^\circ_{f0}(\text{Br}_2^+) = 253 \text{ kcal/mol}]^{44}$, Hg, and HgBr_2 .

We note that an abrupt rise in the PIE for Br_2^+ at $\sim 925 \text{ \AA}$ was found to coincide with the IE of the $^2\Sigma_g^+$ state of HgBr_2^+ . A similar observation was also found in the PIE spectrum for HgBr^+ . In view of the observation that there seems to be no autoionizing structure in the vicinity of the step at $\sim 925 \text{ \AA}$, this feature can be taken as evidence that the formations of HgBr^+ and Br_2^+ are more favorable when HgBr_2^+ ions are prepared in the $^2\Sigma_g^+$ state. This interpretation is consistent with the previous conclusion that the σ_g orbital of HgBr_2 has some bonding character.¹

Br^+

Figure 1(e) shows the PIE curve for Br^+ from HgBr_2 in the region 600-850 \AA obtained using a wavelength resolution of 1.4 \AA (FWHM).

There are two possible processes which can produce Br^+ :

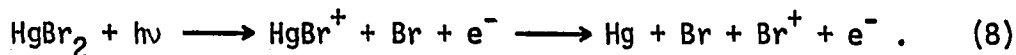


and



The thermochemical thresholds for processes (6) and (7) are 14.93 ± 0.4 eV ($830 \pm 21 \text{ \AA}$) and 15.62 ± 0.09 eV ($793 \pm 5 \text{ \AA}$), respectively. Due to the

gradually rising threshold behavior of the Br^+ ion, the AE of Br^+ ($822 \pm 10 \text{ \AA}$) determined here is likely to be an upper bound. Nevertheless the experimental AE of Br^+ from HgBr_2 is within the limit of uncertainty of the thermochemical threshold for process (6). When the AE of Br^+ and the known values for $\Delta H^\circ_{f0}(\text{Br}^+)$ and $\Delta H^\circ_{f0}(\text{HgBr}_2)$ are used, a value of $31.1 \pm 4.7 \text{ kcal/mol}$ was calculated for $\Delta H^\circ_{f0}(\text{HgBr})$. This value is also in agreement with the literature value [$\Delta H^\circ_{f0}(\text{HgBr}) = 27.6 \pm 9 \text{ kcal/mol}$].⁴² Using $\Delta H^\circ_{f0}(\text{HgBr})$ determined in this study and $\Delta H^\circ_{f0}(\text{Br})$ and $\Delta H^\circ_{f0}(\text{Hg})$, the bond dissociation energy for HgBr was deduced to be $0.54 \pm 0.20 \text{ eV}$. At higher energy, process (7) may also contribute to the formation of Br^+ . We note that the rapid rise in PIE for Br^+ at $\sim 750 \text{ \AA}$ coincides with a sharp decrease in yield for HgBr^+ . It is likely that process (7) is a two-step process



The energetics for the fragment channels from HgBr_2 determined in this study are summarized and compared with values obtained in previous studies in Table V.

Mercuric Iodide

HgI_2^+

Figure 3(a) shows the PIE curve for HgI_2^+ in the region $600\text{--}1350 \text{ \AA}$ obtained using a wavelength resolution of 1.4 \AA (FWHM). The IEs for the electronic states of HgI_2^+ determined by photoelectron spectroscopy¹ are marked by arrows in the PIE spectrum for HgI_2^+ . Similar to the

Table V. Summary of photoionization data for HgBr₂

Ion	AE or IE (eV)	Process
HgBr ₂ ⁺ ($\tilde{\chi}^2\Pi_{3/2g}$)	10.560±0.003 10.62 ^a	HgBr ₂ + hν → HgBr ₂ ⁺ ($\tilde{\chi}^2\Pi_{3/2g}$) + e ⁻
HgBr ₂ ⁺ ($^2\Pi_{1/2g}$)	10.8846±0.0012 10.96 ^a	HgBr ₂ + hν → HgBr ₂ ⁺ ($^2\Pi_{1/2g}$) + e ⁻
HgBr ₂ ⁺ ($^2D_{\pm 5/2}$)	16.397±0.003 16.40 ^a	HgBr ₂ + hν → HgBr ₂ ⁺ ($^2D_{\pm 5/2}$) + e ⁻
HgBr ⁺	11.83±0.03 12.09 ^b	HgBr ₂ + hν → HgBr ⁺ + Br + e ⁻
Hg ⁺	11.85±0.03	HgBr + hν → Hg ⁺ + Br ₂ + e ⁻
Br ₂ ⁺	12.59±0.03	HgBr ₂ + hν → Br ₂ ⁺ + Hg + e ⁻
Br ⁺	15.08±0.18 16.7 ^b	HgBr ₂ + hν → HgBr + Br ⁺ + e ⁻

^aReference 1.

^bReference 7.

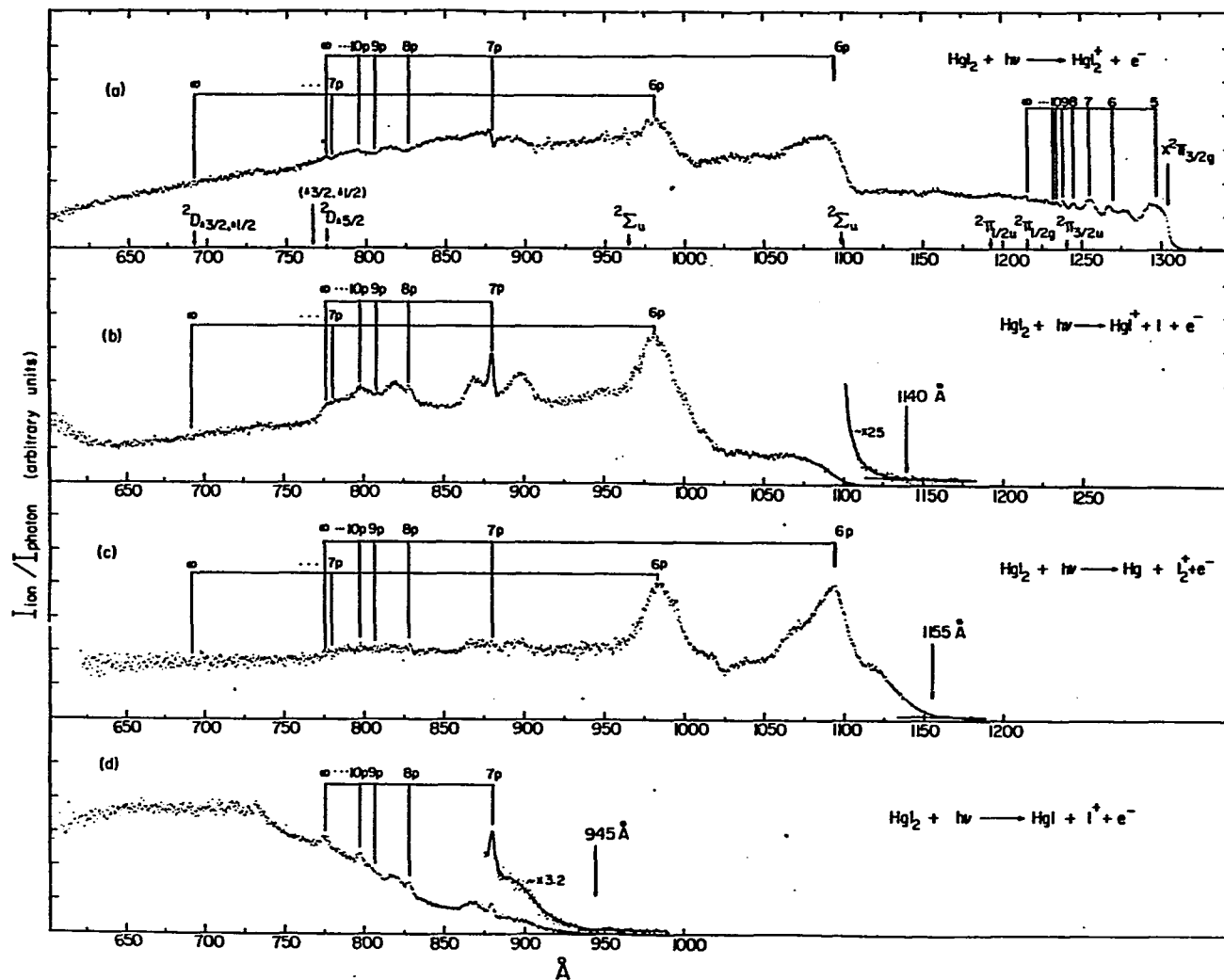


Figure 3. PIE curves for (a) HgI_2^+ , (b) HgI^+ , (c) I_2^+ , and (d) I^+ in the region 600-1350 \AA

observation in the PIE spectrum for HgBr_2^+ , a sharp steplike feature and a small kink were found at the onsets of the $\tilde{X}^2\Pi_{3/2g}$ and $^2\Pi_{1/2g}$ states, respectively. The high resolution (0.14 Å FWHM) PIE spectrum for HgI_2^+ obtained in the region 600-1350 Å does not reveal any additional structures other than those already resolved in the low resolution spectrum. The high resolution (0.14 Å FWHM), PIE curve for HgI_2^+ near the threshold (1215-1310 Å) obtained using the argon continuum as the light source is shown in Fig. 4. The IE for the $\tilde{X}^2\Pi_{3/2g}$ state of HgI_2^+ was determined to be 1303.9 ± 0.3 Å (9.5088 ± 0.0022 eV) which is consistent with that reported previously.¹

The autoionization peaks appearing in the region between the onsets of the $\tilde{X}^2\Pi_{3/2g}$ and $^2\Pi_{1/2g}$ states are associated with members of a Rydberg series converging to the $^2\Pi_{1/2g}$ state. The best fit to the positions of these peaks can be represented by the Rydberg equation:

$$\nu_m = \left[82230 - \frac{R}{(m-0.37)^2} \right] \text{ cm}^{-1}. \quad (9)$$

Table VI lists the observed peak positions (ν_{obs}) and predicted positions (ν_m) according to Eq. (9). The positions of the two lower members, $m = 6$ and 5 , as marked in Fig. 3(a) and 4 were calculated by using Eq. (9). The analysis of this Rydberg series gives a more accurate value for the IE of the $^2\Pi_{1/2g}$ state of HgI_2^+ . The value of 10.1953 ± 0.0025 eV (82230 ± 20 cm^{-1}) determined here for the IE of the $^2\Pi_{1/2g}$ state for HgI_2^+ is slightly higher than that obtained by Eland.¹

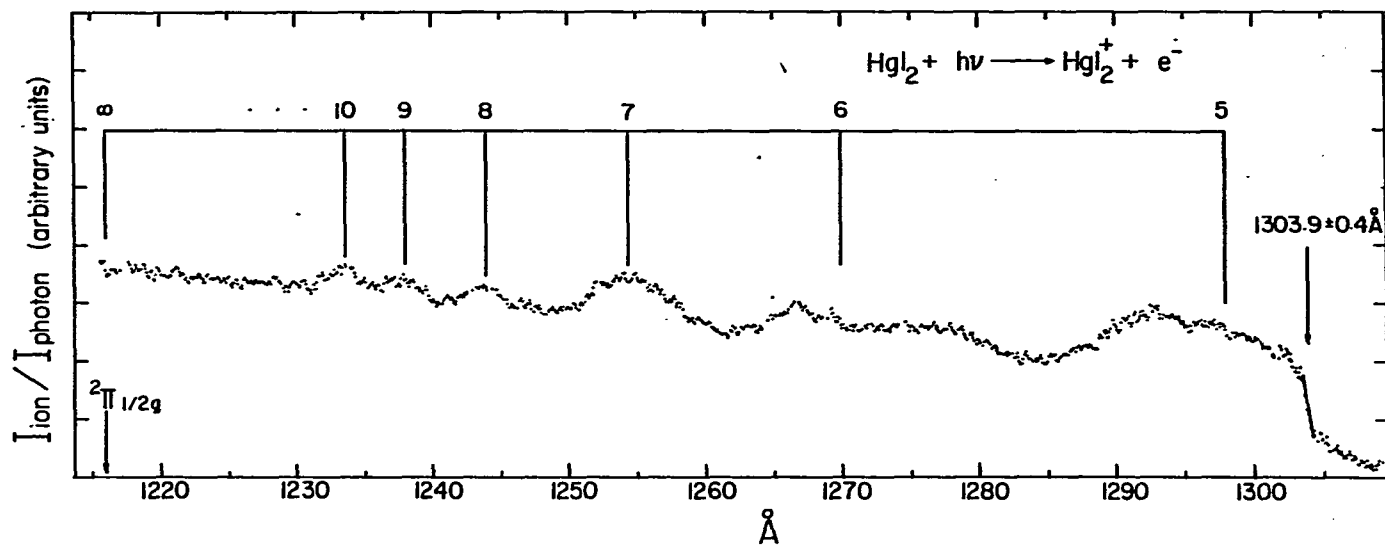


Figure 4. PIE curve (0.14\AA FWHM) for HgI_2^+ in the region 1215-1310 \AA

Table VI. Rydberg series converging to the $^2\Pi_{1/2g}$ threshold of HgI_2^+

$$\nu_m = 82230 - \frac{R}{(m-0.37)^2}$$

n	$\nu_{\text{obs}}(\text{cm}^{-1})$	$\nu_m(\text{cm}^{-1})$
7	79713 (1254.5 Å)	79733
8	80366 (1244.3 Å)	80345
9	80755 (1238.3 Å)	80756
10	81037 (1234.0 Å)	81046
$\text{IE}(^2\Pi_{1/2g}) = 82230 \pm 20 \text{cm}^{-1}$		

The general profile and structure observed in the PIE curve for HgI_2^+ are very similar to those found in the PIE curves for HgCl_2^+ and HgBr_2^+ . The analysis of Rydberg series I and II converging to the $^2D_{\pm 5/2g}$ state at 15.99 eV and $^2D_{\pm 3/2, \pm 1/2}$ states at 17.91 eV, respectively, is summarized in Table VII. The resonance energy ($880.2 \pm 0.1 \text{ \AA}$) for the member $n = 7$ was located in a high resolution spectrum for HgI_2^+ . The members $n = 8$ and 9 of series I and $n = 7$ of series II seem to appear as broad window resonances in Fig. 3(a). With the exception of the resonance energy for the $n = 7$ member which was determined by fitting its resonance profile to the Fano line profile formula as described previously,^{20,41} all the other positions of resonances listed in the table are estimated by either the maximum or minimum depending on whether the resonance exhibits a peaklike or diplike profile, respectively. The IE for the $^2D_{\pm 5/2}$ state of HgI_2^+ as determined by the convergence limit of series I ($15.988 \pm 0.020 \text{ eV}$) is consistent with that measured previously by photoelectron spectroscopy.¹

HgI^+

The PIE curve for HgI^+ from HgI_2 in the region $600\text{-}1180 \text{ \AA}$ obtained by using a wavelength resolution of 1.4 \AA (FWHM) is shown in Fig. 3(b). Similar to observations in the HgCl^+ and HgBr^+ spectra, most of the autoionization structures resolved in the PIE curve for HgI^+ have peaklike line profiles instead of appearing as window resonances in the PIE curve for the parent HgI_2^+ ion. The nature of the two broad peaks located at the higher and lower energy sides of the resonance associated

Table VII. Rydberg series converging the ${}^2D_{\pm 5/2}$ and ${}^2D_{\pm 3/2, \pm 1/2}$ limits of HgI_2^+

n(p)	E(n) (eV)		n^{*b}	δ^c
	Series I	Series II		
6	~ 11.322 (1095 Å)	12.639 (981 Å)	~ 1.708	~ 4.292
7	14.086 (880.2 Å)	15.906 (779.5 Å)	2.675	4.325
8	14.983 (827.5 Å)	...	3.681	4.319
9	15.364 (807 Å)	...	4.671	4.329
10	15.566 (796.5 Å)	...	5.680	4.320
Series limit	IE (${}^2D_{\pm 5/2}$) 15.988 ± 0.020	IE (${}^2D_{\pm 3/2, 1/2}$) 17.91^a

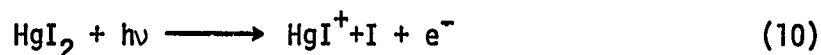
^aReference 1.

^bEffective principal quantum number.

^cQuantum defect.

with the member $n = 7$ at 880.2 \AA is not known. Similar structures were observed in the PIE curves for HgCl^+ , $^{20}\text{HgBr}^+$, Br_2^+ and other fragment ions, I_2^+ and I^+ , which will be discussed below.

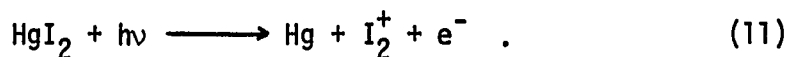
The AE for HgI^+ from HgI_2 was determined to be $1140 \pm 5 \text{ \AA}$ ($10.88 \pm 0.05 \text{ eV}$). Assuming the HgI^+ ions are produced by the reaction



near the threshold, the latter value, along with the known values for $\Delta H^\circ_{f0}(\text{HgI}_2)$ ($-2.353 \pm 0.5 \text{ kcal/mol}$)⁴² and $\Delta H^\circ_{f0}(\text{I})$ ($25.63 \pm 0.01 \text{ kcal/mol}$)⁴², allows the deduction of a value of $222.9 \pm 1.2 \text{ kcal/mol}$ for $\Delta H^\circ_{f0}(\text{HgI}^+)$. By subtracting the value for $\Delta H^\circ_{f0}(\text{HgI})$ ($33.18 \pm 1.1 \text{ kcal/mol}$)⁴² from $\Delta H^\circ_{f0}(\text{HgI}^+)$, the IE of HgI was predicted to be $8.23 \pm 0.07 \text{ eV}$. By using known values for $\Delta H^\circ_{f0}(\text{HgI}^+)$, $\Delta H^\circ_{f0}(\text{Hg}^+)$, and $\Delta H^\circ_{f0}(\text{I})$, a value of $59 \pm 1 \text{ kcal/mol}$ ($2.55 \pm 0.04 \text{ eV}$) was also calculated for the bond dissociation energy of HgI^+ .

I_2^+

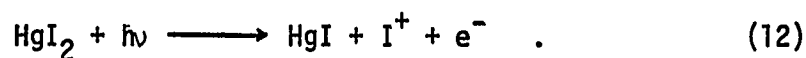
The PIE curve for I_2^+ from HgI_2 in the region $600\text{--}1190 \text{ \AA}$ obtained using a wavelength resolution of 1.4 \AA (FWHM) is shown in Fig. 3(c). Autoionizing peaks associated with the $n = 6$ members of series I and II were found to be the dominate structures. The AE for the formation of I_2^+ from HgI_2 was determined to be $1155 \pm 3 \text{ \AA}$ ($10.73 \pm 0.03 \text{ \AA}$). The value is slightly lower than the thermochemical threshold (10.83 eV) for the reaction



This discrepancy is partly due to the uncertainty in the IE of I_2 and partly due to finite vibrational hot band effects in this study.⁴⁴

I^+

Figure 3(d) shows the PIE curve for I^+ in the region 600-1000 Å obtained using a wavelength resolution of 1.4 Å (FWHM). The AE for the formation of I^+ from HgI_2 was determined to be 945 ± 3 Å (13.12 ± 0.04 eV) which is in excellent agreement with the thermochemical threshold (13.10 ± 0.05 eV) for the process



Using the AE for I^+ and known values for $\Delta H^\circ_{f0}(HgI_2)$, $\Delta H^\circ_{f0}(I^+)$, $\Delta H^\circ_{f0}(Hg)$ and $\Delta H^\circ_{f0}(I)$, the bond dissociation energy for the HgI was calculated to be 0.32 ± 0.06 eV which is also consistent with the literature value.⁴⁵⁻⁴⁷

Table VIII summarizes the energetics of fragmentation processes determined in this study. Some values obtained by other techniques are also included in the table for comparison.

Table VIII. Summary of photoionization data for HgI₂

Ion	AE or IE	Process
HgI ₂ ⁺ ($\tilde{X}^2\Pi_{3/2g}$)	9.5088±.0022 9.50 ^a	HgI ₂ + hν → HgI ₂ ⁺ ($\tilde{X}^2\Pi_{3/2g}$) + e
HgI ₂ ⁺ ($^2\Pi_{1/2g}$)	10.1953±.0025 10.16 ^a	HgI ₂ + hν → HgI ₂ ⁺ ($^2\Pi_{1/2g}$) + e
HgI ₂ ⁺ ($^2D_{\pm 5/2}$)	15.988±0.020 15.99 ^a	HgI ₂ + hν → HgI ₂ ⁺ ($D_{5/2}$) + e
HgI ⁺	10.88±0.05 11.3±0.4 ^b	HgI ₂ + hν → HgI ⁺ + I + e
I ₂ ⁺	10.73±0.04	HgI ₂ + hν → I ₂ ⁺ + Hg + e
I ⁺	13.12±0.04 15.5±0.4 ^b	HgI ₂ + hν → I ⁺ + HgI + e

^aReference 1.

^bReference 7.

DISCUSSION

Spin-Orbit Splitting of the ${}^2\Pi_g$ State of HgX_2

Since the energy of the Hg 6p orbitals is considerably higher than that of the 6s orbital, the highest occupied molecular orbital of HgX_2 is expected to resemble the π_g molecular orbital of a diatomic halogen at large internuclear distance. Therefore, the spin-orbit splitting for the ${}^2\Pi_g$ state of HgX_2^+ should be characteristic of the halogen atoms. The theory of spin-orbit interaction in molecules has been summarized by Van Vleck.⁴⁸ A simple approximation was reported previously for the diatomic halogens.⁴⁹ Cornford *et al.* show that by neglecting differential overlap and two-center integrals, the spin-orbit splitting for a diatomic halogen is roughly equal to two-thirds of the free-atom value. The values for the ${}^2P_{3/2} - {}^2P_{1/2}$ splitting in chlorine, bromine, and iodine are 0.11, 0.46, and 0.94 eV,⁵⁰ respectively. Thus, the values for the spin-orbit splittings of HgCl_2 , HgBr_2 , and HgI_2 predicted by this approximation are 0.07, 0.31, and 0.63 eV, respectively. The latter values are in agreement with experimental values for the spin-orbit splittings of the ${}^2\Pi_g$ states of HgBr_2^+ (0.325 ± 0.003 eV) and HgI_2^+ (0.687 ± 0.003 eV), whereas the experimental value for HgCl_2^+ (0.125 ± 0.003 eV) is higher than the predicted value.

Series I and II

Converging to the ${}^2D_{\pm 5/2}$
and ${}^2D_{\pm 3/2, \pm 1/2}$ States of HgX_2^+

Prominent structures resolved in the PIE curve for Hg^+ from Hg were attributed to autoionizing Rydberg series corresponding to excitations of inner shell 5d electrons to np, $n \geq 6$, Rydberg orbitals.^{51,52} Linn et al.²⁰ point out that since one expects that the 5d orbitals (especially the $5d_{x^2-y^2}$ and $5d_{xy}$ orbitals) of Hg in HgX_2 only play a minor role in the bonding of the mercuric halides and remain mostly atomic in nature, Rydberg transitions similar to those observed in Hg should be manifest as prominent structures in the photoabsorption spectra of HgX_2 . As a result of the stronger electron withdrawing character of the halogen atoms in comparison with that of the mercury atom, binding energies for electrons in the 5d shell of Hg in HgX_2 are greater than those of the mercury atom. Therefore, Rydberg transitions originating from the 5d orbitals in HgX_2 , if observable in the PIE curve of HgX_2 and its fragment ions, should be shifted by approximately the difference in binding energies of the 5d electrons in HgX_2 and Hg. In a comparison of the PIE curve for Hg^+ from Hg and that for HgCl_2^+ , Linn et al. found a close correspondence between Rydberg structures observed in the Hg^+ and HgCl_2^+ spectra. Members of autoionizing Rydberg Series I of HgCl_2 were found to be blue-shifted by ~ 1.7 eV with respect to corresponding members of the autoionizing series $[(5d)^9(6s)^2D_{5/2}] np, {}^1P^0$, of Hg, and these shifts

are approximately equal to the difference (1.9 eV) between the IE of the ${}^2D_{\pm 5/2}$ state of HgCl_2^+ and that of the ${}^2D_{5/2}$ state of Hg^+ . Similarly, members of autoionizing series II of HgCl_2 are blue-shifted by 2 eV relative to corresponding members of the series $[(5d)^9(6s)^2 {}^2D_{3/2}] np, {}^3P^o$, of Hg, and these shifts are also close to the separation (1.94 eV) between the IEs of the ${}^2D_{\pm 3/2, \pm 1/2}$ states of HgCl_2^+ and that of the ${}^2D_{3/2}$ state of Hg^+ . This observation has led Linn et al. to conclude that Series I and Series II can be assigned to transitions:

$$[(5d)^{10} \sigma_g^2 \sigma_u^2 \pi_u^4 \pi_g^4] \rightarrow [(5d)^9 \sigma_g^2 \sigma_u^2 \pi_u^4 \pi_g^4 {}^2D_{\pm 5/2}] np \text{ and}$$

$$[(5d)^{10} \sigma_g^2 \sigma_u^2 \pi_u^4 \pi_g^4] \quad [(5d)^9 \sigma_g^2 \sigma_u^2 \pi_u^4 \pi_g^4 {}^2D_{\pm 3/2, \pm 1/2}] np,$$

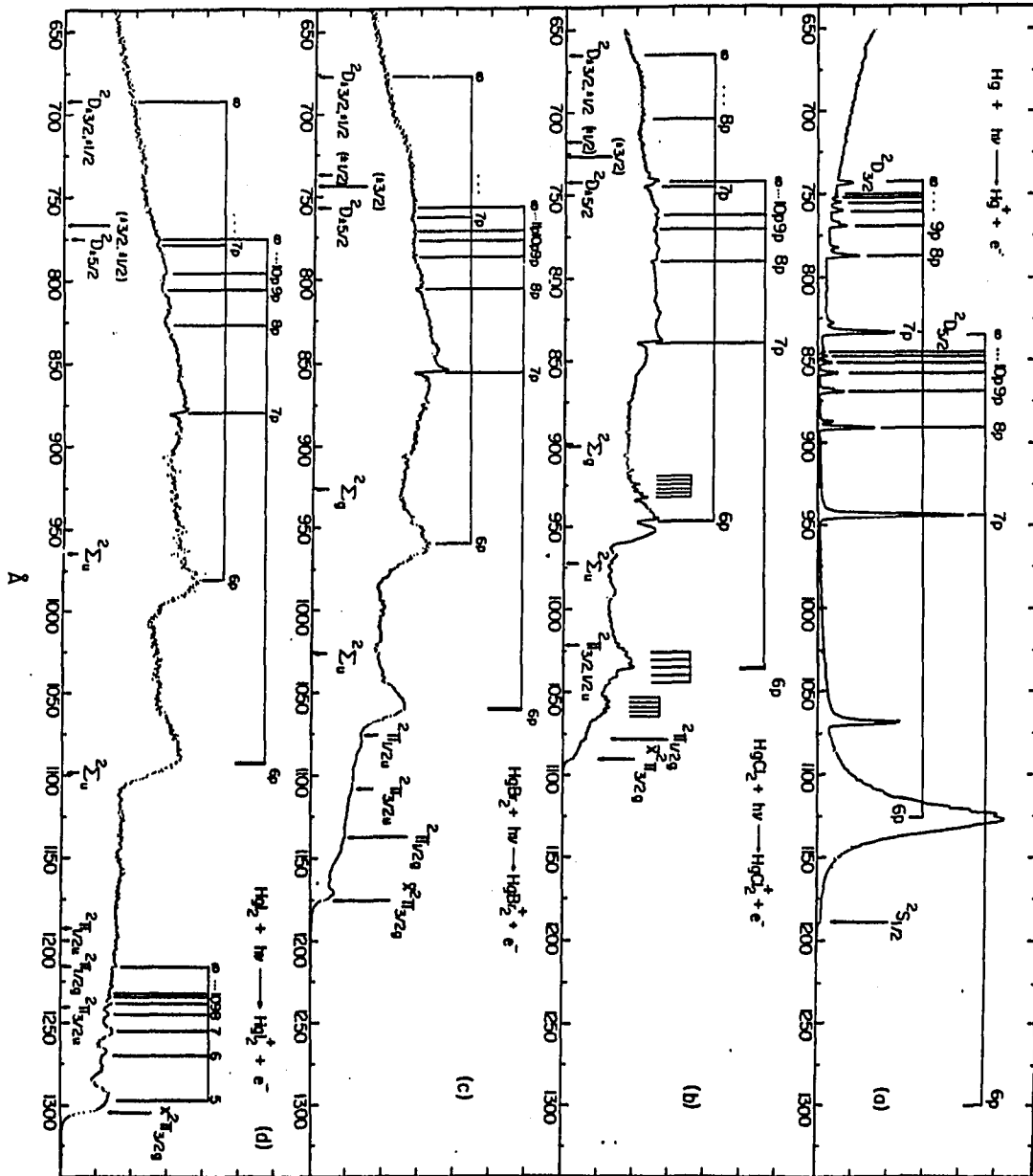
respectively, which are mainly associated with Hg in HgCl_2 . Figures 5(a), 5(b), 5(c), and 5(d) compare the PIE curves for Hg^+ from Hg, HgCl_2^+ , HgBr_2^+ , and HgI_2^+ . The PIE curve for Hg^+ from Hg was obtained in our laboratory in a separate study using a similar experimental arrangement. It is obvious that Series I and II identified in HgBr_2 and HgI_2 are similar in nature to those observed in HgCl_2 and can be assigned to the same Rydberg transitions as in HgCl_2 . The assignment of the values for the principal quantum number for members of Series I and II for HgBr_2 and HgI_2 summarized in Tables IV and VII is based on this comparison.

Resonance Line Profiles

The parameterization of the 7p line of Series I appearing in the high resolution (0.14 Å FWHM) PIE curve for HgCl_2^+ according to the Fano line shape formula⁴¹

Figure 5. PIE curves for (a) Hg^+ from Hg , (b) HgCl_2^+ , (c) HgBr_2^+ , and (d) HgI_2^+ in the region 625-1350 Å

Ion / Iphoton (arbitrary units)



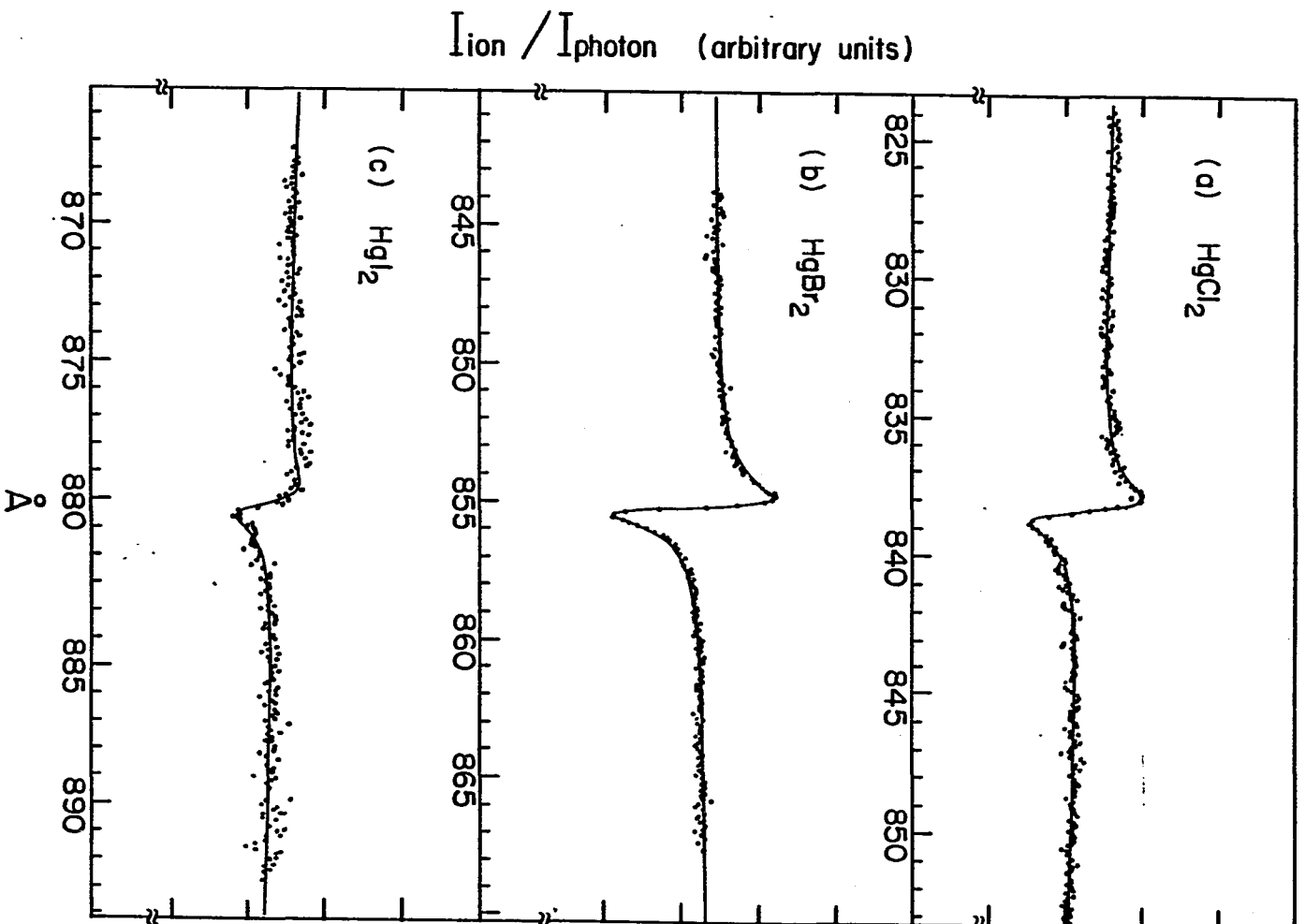
$$\sigma(E) = \sigma_{cm} + \sigma_{rm} \frac{q_m^2 + 2\epsilon q_m - 1}{1 + \epsilon^2} \quad (13)$$

has been reported previously.²⁰ Here, $\epsilon = (E - E_0)/(\Gamma/2)$, E_0 is the energy of the resonance after perturbation by the continuum, Γ is the width of the resonance, q_m is the shape parameter for channel m , and σ_{cm} and σ_{rm} show the strength of the continuum and the resonance, respectively. The validity and limitation in physical significance of the fitting to resonances observed in molecular photoionization according to Eq. 13 have been discussed extensively by Eland *et al.*⁴¹ Since only the PIE curves for HgBr_2^+ and HgI_2^+ have been obtained in high resolution, the 7p line profiles of Series I resolved in the resolution spectra of HgBr_2^+ and HgI_2^+ were chosen for careful parameterizations. At the resonance energies for the 7p levels, the intensities of the fragment ions from HgCl_2 , HgBr_2 and HgI_2 only constitute 8%, 12%, and ~15% of the total intensities, respectively. The values for E_0 , Γ , q_m and σ_{cm}/σ_{rm} determined for the $7p(^2D_{\pm 5/2})$ levels of HgBr_2 and HgI_2 are compared with those for HgCl_2 in Table IX. The fittings of the observed resonance line profiles for the $7p(^2D_{\pm 5/2})$ levels of HgCl_2 , HgBr_2 , and HgI_2 by using parameters listed in Table IX are shown in Figs. 6(a), 6(b), and 6(c), respectively. The q_m values for these resonances were found to be in the order $q_m(\text{HgCl}_2) > q_m(\text{HgBr}_2) > q_m(\text{HgI}_2)$, whereas the values for the widths Γ are quite close. Taking the widths of these resonances to be a measure of the lifetimes

Table IX. Resonance parameters for the $7p(^2D_{\pm 5/2})$ levels in the PIE curves for HgX_2^+ , X = Cl, Br, and I

Resonances	n^*	$E_0 (\text{\AA})$	$\Gamma(\text{eV})$	q_m	$\sigma_{\text{rm}}/\sigma_{\text{cm}}$
$7p(\text{HgCl}_2)$	2.658	838.42	0.016	0.88	0.25
$7p(\text{HgBr}_2)$	2.678	855.2	0.012	0.81	0.33
$7p(\text{HgI}_2)$	2.675	880.2	0.017	0.61	0.15

Figure 6. Theoretical fits to the resonance line profiles of the $7p(^2D_{\pm 5/2})$ levels resolved in the PIE curves for (a) HgCl_2^+ , (b) HgBr_2^+ and HgI_2^+



through the uncertainty relationship, the lifetimes for the $7p(^2D_{\pm 5/2})$ levels of HgX_2 are estimated to be $\sim 10^{-14}$ s.

Precise parameterizations of the resonance peak shapes of the $7p(^2D_{\pm 5/2})$ level in the fragment curves are not possible because the widths of these resonances ($\Gamma(HgCl_2) = 0.9 \text{ \AA}$, $\Gamma(HgBr_2) = 0.7 \text{ \AA}$, and $\Gamma(HgI_2) = 1.2 \text{ \AA}$) are smaller than the instrumental resolution (1.4 \AA FWHM) used in obtaining the fragment ion spectra. Furthermore, the presence of broad unassigned structures near many of the resonances makes parameterization difficult due to the large uncertainties introduced in quantifying the background continuum curves. In spite of this difficulty, crude estimates of the q_m values for resonance line profiles of the $7p(^2D_{\pm 5/2})$ levels appearing in the fragment ions spectra are shown in Table X. Due to the weakness of the resonances observed in the $Hg^+(HgBr_2)$ and I_2^+ spectra, the q_m values cannot be determined. In a systematic examination of resonances found in the PIE curves for other linear molecular ions and their fragments, Eland *et al.*⁴¹ found that the $|q_m|$ value was usually largest in the weakest channel. This conclusion is valid for the channels observed in $HgCl_2$. The branching ratio of $HgCl_2^+ : Hg^+ : HgCl^+$ at 850 \AA is 28:1.4:1 where q_m is in the order $q_m(HgCl_2^+) < q_m(Hg^+) < q_m(HgCl^+)$. However, in the case of $HgBr_2$, the branching ratio at 850 \AA for $HgBr_2^+ : HgBr^+ : Hg:Br_2$ is 201:21:5:1, a qualitative examination of the spectra reveals that the strongest fragmentation channel, $HgBr^+$, has the largest q_m value. For HgI_2 , the branching ratio at the resonance energy of the $7p(^2D_{\pm 5/2})$

Table X. q_m values for the $7p(^2D_{\pm 5/2})$ resonances appearing in the PIE curves for HgX_2^+ ($X = \text{Cl}, \text{Br}, \text{and I}$) and their fragment ions

Ions	q_m
HgCl_2^+	0.9 ^a
Hg^+	1.3
HgCl^+	2.2
HgBr_2^+	0.8 ^a
HgBr^+	5.3
Hg^+	>1 ^b
Br_2^+	1.8
HgI_2^+	0.6 ^a
HgI^+	3.0
I^+	2.7
I_2	... ^b

^aBased on the high resolution data.

^bResonances are too weak for parameterization.

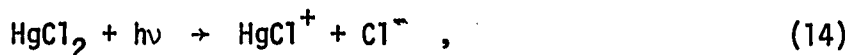
level for $\text{HgI}_2^+:\text{HgI}^+:\text{I}^+:\text{I}_2^+$ is approximately 65:10:1.5:1. Here, again the q_m value is largest for the HgI^+ fragment which is the strongest fragmentation channel available. The previous observation that $|q_m|$ is generally largest in the weakest channel does not seem to be valid for HgBr_2 and HgI_2 . However, a more definite conclusion has to await quantitative analysis of these resonances observed in higher resolution.

Fragmentation Processes of HgX_2

Considering that the fragmentations of HgX_2 are preceded by photoionization and that the available electronic states of HgX_2^+ are all doublet states as those determined in photoelectron spectroscopy, the formations of the lowest product states of these fragmentation channels, $\text{HgX}^+(^1\Sigma) + \text{X}(^2\text{P}_{3/2})$, $\text{Hg}^+(^2\text{S}_{1/2}) + \text{Cl}_2(^1\Sigma)$, $\text{X}_2^+(^2\Pi_{3/2g}) + \text{Hg}(^1\text{S}_0)$, and $\text{X}^+(^3\text{P}_2) + \text{HgX}(^2\Sigma)$, obey the spin correlation rule. This consideration is consistent with the fact that the AEs of many of these fragmentation processes were found to be in agreement with their known thermochemical thresholds. When the thresholds of the formations of $\text{HgX}^+(^1\Sigma) + \text{X}(^2\text{P}_{3/2})$, $\text{X} = \text{Cl}, \text{Br}, \text{and I}$, are not known, the spin correlation rule also supports the identifications of the experimental AEs to be the thermochemical thresholds for the lowest product states.

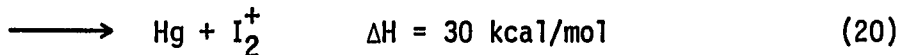
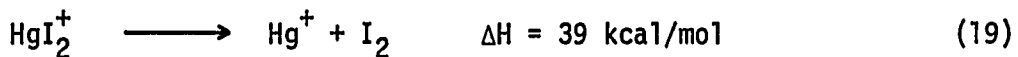
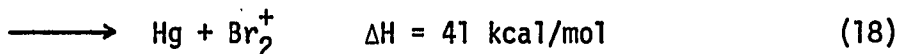
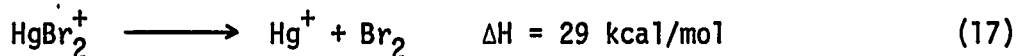
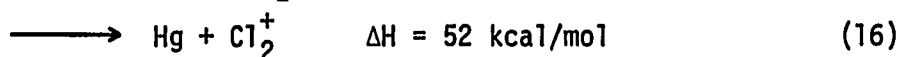
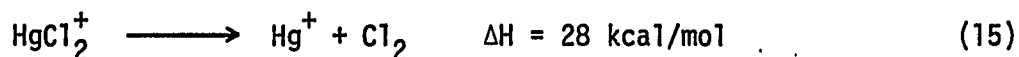
In the photoionization study of HgCl_2 , Linn *et al.*²⁰ found that weak HgCl^+ signals persist below the IE of HgCl_2 . The AEs for HgBr^+ and HgI^+ were found to be well-behaved here and have values above the IEs of HgBr_2 and HgI_2 , respectively. Since the HgCl_2 , HgBr_2 , and HgI_2 experiments were performed in similar experimental conditions,

this observation supports the previous conclusion that HgCl^+ ions observed below the IE of HgCl_2 are not due to secondary collisional processes. If the HgCl^+ ions formed below the IE of HgCl_2 originate from the ion-pair process



it is intriguing that similar processes are not observed in HgBr_2 and HgI_2 . A careful search for the ion-pair process (14) is needed in order to make a positive identification for the formation of HgCl^+ near the threshold.

It is interesting to note that the Hg^+ fragment is only observed from HgCl_2 and HgBr_2 and not from HgI_2 while the X_2^+ fragment is observed from both HgBr_2 and HgI_2 and not in HgCl_2 . Assuming the formations of $\text{Hg}^+ + \text{X}_2$ and $\text{Hg} + \text{X}_2^+$ from HgX_2^+ to be competing processes, a rationalization can be found by examining the energetics of the two processes in each case.



This examination seems to indicate that the lower energetic channels are favored. In the case of HgBr_2 where both Hg^+ and Br_2^+ are observed,

the intensity of Hg^+ is much greater than that of Br_2^+ . We are aware that the exclusion of the participation by other fragmentation channels as competing processes may not be justified.

$D_0(\text{HgX})$, $\text{IE}(\text{HgX})$, and $D_0(\text{HgX}^+)$

The bond dissociation energies of HgX , $D_0(\text{HgX})$, and HgX^+ , $D_0(\text{HgX}^+)$, and the IEs of HgX determined in this study are listed in Table XI. Values for $D_0(\text{HgX})$ obtained previously by spectroscopic methods^{45,46} and theoretical calculations¹¹ are also included in the table. The bond dissociation energies for HgCl , HgBr , and HgI determined here are found to be slightly smaller than those reported by Wilcomb and Bernstein.⁴⁶ Taking into account the error limits, they are all in agreement with those obtained by Wieland⁴⁵ and Wadt.¹¹ Because of the gradual tailing structure of the thresholds for the formations of X^+ from HgX_2 , it is not surprising to find that values for $D_0(\text{HgX})$ derived from the measured AEs of X^+ are lower bounds.

The bond dissociation energies for HgCl^+ , HgBr^+ , and HgI^+ are similar. The IE of HgX is in the order $\text{IE}(\text{HgCl}) > \text{IE}(\text{HgBr}) > \text{IE}(\text{HgI})$. If the highest occupied orbital of HgX has strong Hg character and the electron in this orbital is mainly localized at Hg in HgX , the increase in electronegativity from I to Cl is expected to increase the energy needed to eject the electron from the highest occupied orbital. A similar trend was observed previously for the IEs of heterogeneous diatomic halogen molecules,⁴⁴ e.g. the IEs of I_2 , IBr , and ICl are found to be in the order $\text{IE}(\text{ICl}) > \text{IE}(\text{IBr}) > \text{IE}(\text{I}_2)$.⁵³

Table XI. Bond dissociation energies (D_0) of HgX and HgX^+ and ionization energies (IE) of HgX , $X = \text{Cl}, \text{Br}, \text{and I}$

HgX	$D_0(\text{HgX})$ (eV)	$D_0(\text{HgX}^+)$ (eV)	IE(HgX) (eV)
HgCl	0.92 ± 0.10^a	$\sim 2.33^a$	$\sim 9.16^a$
	1.067 ± 0.025^b		
	1.04 ± 0.1^c		
	0.91^d		
HgBr	0.54 ± 0.20^e	2.39 ± 0.09^e	8.73 ± 0.39^e
	0.744 ± 0.025^b		
	0.712 ± 0.021^c		
	0.48^d		
HgI	0.32 ± 0.05^e	2.55 ± 0.04^e	8.23 ± 0.07^e
	0.387 ± 0.006^b		
	0.354 ± 0.018^c		

^aReference 20.

^bReference 46.

^cReferences 45 and 47.

^dReference 11.

^eThis work.

SUMMARY

The photoionization study of HgBr_2 and HgI_2 has been successfully carried out using the molecular beam method. This study not only has provided more accurate IEs for the $\tilde{X}^2\Pi_{3/2g}$, $^2\Pi_{1/2g}$, and $^2D_{\pm 5/2}$ states of HgBr_2^+ and HgI_2^+ , it has also identified transitions corresponding to Rydberg series I and II of HgBr_2 and HgI_2 . The fragmentation processes for HgCl_2^+ , HgBr_2^+ and HgI_2^+ are found to be similar. From the measured AEs for the formations of X^+ and HgX^+ , $X = \text{Br}$ and I , bond dissociation energies for HgBr , HgI , HgBr^+ , and HgI^+ were calculated.

REFERENCES

1. J.H.D. Eland, *Int. J. Mass Spectrom. Ion Phys.* 4, 37 (1970).
2. J. Berkowitz, *J. Chem. Phys.* 61, 407 (1974).
3. K. Wittel, B. S. Mohanty, and R. Manne, *J. Electron Spectrosc. Rel. Phenom.* 5, 1115 (1974).
4. L. C. Cusachs, F. A. Grimm, and G. K. Schweitzer, *J. Electron Spectrosc. Rel. Phenom.* 3, 229 (1974).
5. S. Evans and A. F. Orchard, *J. Electron Spectrosc. Rel. Phenom.* 6, 207 (1975).
6. R. G. Egde11, A. F. Orchard, D. R. Lloyd, and N. Y. Richardson, *J. Electron Spectrosc. Rel. Phenom.* 12, 415 (1977).
7. R. W. Kiser, J. G. Dillard, and D. L. Dugger, "Advances in Chemistry Series", Vol. 72 (American Chemical Society, Washington, D.C., 1968), p 153.
8. A. Terenin, *Z. Phys.* 44, 713 (1927).
9. K. Wieland, *Z. Phys.* 76, 801 (1932).
10. K. Wieland, *Z. Phys.* 77, 157 (1932).
11. W. R. Wadt, *J. Chem. Phys.* 72, 2469 (1980).
12. J. Maya, *J. Chem. Phys.* 67, 4976 (1977).
13. J. Husain, J. R. Wiesenfeld, and R. N. Zare, *J. Chem. Phys.* 72, 2479 (1980).
14. H. Hofmann and S. R. Leone, *J. Chem. Phys.* 68, 3819 (1978).
15. J. H. Parks, *Appl. Phys. Lett.* 31, 192 (1977).
16. J. G. Eden, *Appl. Phys. Lett.* 31, 448 (1977).
17. J. H. Park, *Appl. Phys. Lett.* 31, 297 (1977).

18. E. J. Schimitschek and J. E. Celto, *Opt. Lett.* 2, 64 (1978).
19. R. L. Burnham, *Appl. Phys. Lett.* 33, 156 (1978).
20. S. H. Linn, J. M. Brom, Jr., W.-B. Tzeng, and C. Y. Ng, *J. Chem. Phys.* (submitted).
21. Y. Ono, S. H. Linn, H. F. Prest, M. E. Gress, and C. Y. Ng, *J. Chem. Phys.* 73, 2523 (1980).
22. K. E. Schubert and R. D. Hudson, "A Photoelectric Atlas of the Intense Lines of the Hydrogen Molecular Emission Spectrum from 1025 to 1650 Å at a Resolution of 0.10 Å", Report Number ATN-64(9233)-2, Aerospace Corp., Los Angeles, 1963.
23. G. Herzberg, "Molecular Spectra and Molecular Structure of Polyatomic Molecules" (Van Nostrand, Princeton, N. J., 1966).
24. M. Wehrli, *Helv. Phys. Acta* 11, 339 (1938).
25. U. Fano, *Nuovo Cimento* 12, 156 (1935).
26. H. Beulter, *Z. Phys.* 93, 177 (1935).
27. U. Fano, *Phys. Rev. A* 1, 1976 (1961).
28. U. Fano and J. W. Cooper, *Phys. Rev. Sect. A* 137, 1364 (1965).
29. U. Fano and J. W. Cooper, *Rev. Mod. Phys.* 40, 441 (1968).
30. J. N. Bardsley, *Chem. Phys. Lett.* 2, 329 (1968).
31. A. L. Smith, *J. Quant. Spectrosc. Radiat. Transfer* 10, 1129 (1970).
32. D. L. Ederer, *Phys. Rev. A* 4, 2263 (1971).
33. A. L. Smith, *Phil. Trans. Roy. Soc. Lond. A* 268, 169 (1970).

34. F. H. Mies, Phys. Rev. 175, 164 (1968).
35. M. J. Seaton, Proc. Phys. Soc. London 88, 801 (1966).
36. K. T. Lu, Phys. Rev. Lett. 33, 123 (1974).
37. U. Fano, J. Opt. Soc. Am. 65, 979 (1975).
38. D. L. Ederer, Phys. Rev. A 14, 1936 (1976).
39. A. F. Starace, Phys. Rev. A 16, 231 (1977).
40. P. C. Kemeny, J.A.R. Samson, and A. F. Starace, J. Phys. B 10, 1201 (1977).
41. J.H.D. Eland, J. Berkowitz, and J. E. Monohan, J. Chem. Phys. 72, 253 (1980).
42. "JANAF Thermochemical Tables", Natl. Stand. Ref. Data Ser. 37, Natl. Bur. Stand., June 1971.
43. In view of the efficient cooling of the rotational and low-frequency vibrational degrees of freedom, we assume heats of formation determined in this study correspond to 0 K values.
44. H. M. Rosenstock, K. Draxl, B. W. Steiner, J. T. Heron, J. Phys. and Chem. Ref. Data 6, Suppl. 1 (1977).
45. K. Wieland, Z. Elektrochem. 64, 761 (1960); K. Wieland, Helv. Phys. Acta 14, 420 (1941).
46. B. E. Wilcomb and R. B. Bernstein, J. Mol. Spectros. 62, 442 (1976).
47. K. P. Huber and G. Herzberg, "Molecular Spectra and Molecular Structure IV: Constants of Diatomic Molecules" (Van Nostrand Reinhold, New York, 1979).

48. J. H. Van Vleck, Rev. Mod. Phys. 23, 213 (1951).
49. A. B. Cornford, D. C. Frost, C. A. McDowell, J. L. Ragle,
and I. A. Stenhouse, J. Chem. Phys. 54, 1872 (1971).
50. C. E. Moore, "Atomic Energy Levels", Vol. 1, Natl. Bur. Std.
Circular No. 467 (U.S. Government Printing Office, Washington,
D.C., 1949).
51. J. Berkowitz and C. Lifshitz, J. Phys. B 1, 438 (1968).
52. B. Brehm, Z. Naturf. 212, 196 (1966).
53. A. B. Cornford, Univ. of British Columbia, Ph.D. Thesis, 1971.

SECTION III.
PHOTOIONIZATION STUDY OF
CO₂, N₂O DIMERS AND CLUSTERS

ABSTRACT

Photoionization efficiency data for $(\text{CO}_2)_{2-4}^+$ and $(\text{N}_2\text{O})_2^+$ in the region 600-1020 Å have been obtained using the molecular beam method. The ionization energies (IE) of $(\text{CO}_2)_2$, $(\text{CO}_2)_3$, $(\text{CO}_2)_4$ and $(\text{N}_2\text{O})_2$ were measured to be 13.32 ± 0.02 eV (930.5 ± 1.5 Å), 13.24 ± 0.02 eV (936.5 ± 1.5 Å), 13.18 ± 0.02 eV (941 ± 1.5 Å), and 12.35 ± 0.03 eV (1004 ± 1.5 Å), respectively. Using these values, the known IEs for CO_2 and N_2O , and the estimated binding energies for $(\text{CO}_2)_2$ and $(\text{N}_2\text{O})_2$, the dissociation energies for $\text{CO}_2^+ \cdot \text{CO}_2$, $(\text{CO}_2)_2^+ \cdot \text{CO}_2$, $(\text{CO}_2)_3 \cdot \text{CO}_2$, and $\text{N}_2\text{O}^+ \cdot \text{N}_2\text{O}$ were deduced to be 11.8 ± 1.0 , 3.3 ± 1.4 , 2.8 ± 1.4 , and 13.1 ± 0.9 kcal/mol, respectively. The ion-molecule half reaction $\text{N}_2\text{O}^+ \cdot \text{N}_2\text{O} \rightarrow \text{N}_3\text{O}_2^+ + \text{N}$ was observed. The analysis of the photoionization efficiency curves for $(\text{CO}_2)_2^+$ and $(\text{N}_2\text{O})_2^+$ suggests that electronic predissociation or direct dissociation might be important dissociation mechanisms for the $\text{CO}_2^*(n) \cdot \text{CO}_2$ and $\text{N}_2\text{O}^*(n) \cdot \text{N}_2\text{O}$ excited Rydberg dimers.

INTRODUCTION

The change in enthalpy at ~ 530 K for the ion-molecule association reaction



has been determined to be -16.2 ± 1.5 kcal/mol by Meot-Ner and Field¹ using the pulsed high pressure mass spectrometric method. In a photoionization study of carbon dioxide using synchrotron radiation as the light source, Jones and Taylor² deduced a value of ~ 9 kcal/mol³ for the bond dissociation energy for $\text{CO}_2^+ \cdot \text{CO}_2$ from the measured ionization energy (IE) and the estimated binding energy for $(\text{CO}_2)_2$. From the comparison of the latter value with that reported in Ref. 1, Jones and Taylor concluded the ionization onset was not the adiabatic IE for $(\text{CO}_2)_2$. The main disadvantage of using synchrotron radiation as the light source in measuring the ionization onsets of clusters is the difficulty of eliminating the effect of refracted higher order vacuum ultraviolet (VUV) light. At the onset, where the ionization cross section is low, ions produced by higher order VUV light will make the identification of the true IE extremely difficult.

Values for the stabilities of dimeric ions^{4,5} derived from recent photoionization experiments using laboratory discharge lamps as the light source are found to be in agreement with values obtained from equilibrium constant measurements. This indicates that the IEs measured for these dimers are very close to their true adiabatic IEs.

Since carbon dioxide cluster ions are of planetary atmospheric significance,⁶ we have remeasured the stabilities of $(\text{CO}_2)_2^+$, $(\text{CO}_2)_3^+$, and $(\text{CO}_2)_4^+$.

Previous photoionization studies of $(\text{H}_2)_2$,⁷ $(\text{CS}_2)_2$,⁴ $(\text{OCS})_2$,⁸ $(\text{CO})_2$, $(\text{N}_2)_2$, $(\text{NO})_2$,⁹ and $(\text{O}_2)_2$ ⁵ suggested that vibrational predissociation is an important dissociation process for these excited Rydberg dimers. Due to the similarity between electronic structures of CO_2 and N_2O with those of CS_2 and OCS , the comparison of PIE curves for $(\text{CO}_2)_2^+$ and $(\text{N}_2\text{O})_2^+$ with those for $(\text{CS}_2)_2^+$ and $(\text{OCS})_2^+$ should provide insight into the dissociation mechanism of these excited Rydberg dimers.

EXPERIMENTAL

The experimental arrangement and procedures are similar to those described previously.^{4,10} The grating employed in this study was the Bausch and Lomb 1200 λ /mm osmium coated aluminum grating blazed at 1360 \AA . The helium Hopfield continuum was used as the light source throughout this experiment except at the ionization onset of $(\text{N}_2\text{O})_2^0$ where the hydrogen many-lined pseudocontinuum was used.

Photoionization efficiency (PIE) data were obtained in this study using 500 μm entrance and exit slits and the resolution attained was 1.4 \AA (FWHM). Each PIE curve was based on at least two scans and prominent structures in the curve were found to be reproducible. Wavelength calibrations were achieved using known atomic resonance lines, or H_2 emission lines¹¹ when the H_2 pseudocontinuum was used.

The carbon dioxide (>99.99% purity) and nitrous oxide (>99.99% purity) used in this experiment were obtained from Matheson. The CO_2 molecular beam was produced by supersonic expansion through a 0.05 mm diameter stainless steel nozzle at a stagnation pressure of ~ 1000 Torr. The N_2O molecular beam was prepared by expansion through a cooled nozzle (~ 220 K) at a stagnation pressure of ~ 600 Torr. The stability of the nozzle temperature was maintained at better than ± 3 K as monitored with a thermocouple.

Data are plotted at intervals of 0.25 and 0.5 \AA except for N_3O_2^+ where part of the data is plotted at intervals of 1 \AA . The net counting rates for $(\text{CO}_2)_2^+$ (at 800 \AA), $(\text{CO}_2)_3^+$ (at 925 \AA), $(\text{CO}_2)_4^+$ (at 930 \AA),

$(\text{N}_2\text{O})_2^+$ (at 800 Å), and N_3O_2^+ (at 800 Å) were about 5000, 160, 150, 5500, and 30 ct/s, respectively. The counting times varied from 5 s for the dimers to 300 s for N_3O_2^+ near the onsets. In general, the signal-to-noise ratios obtained are $\leq 3\%$ for $(\text{CO}_2)_2^+$, $(\text{CO}_2)_3^+$, and $(\text{N}_2\text{O})_2^+$, $\leq 5\%$ for $(\text{CO}_2)_3^+$ and $(\text{CO}_2)_4^+$ near the thresholds, and $\sim 5\text{--}10\%$ for N_3O_2^+ .

RESULTS AND DISCUSSION

Photoionization efficiency data for CO_2^+ , $(\text{CO}_2)_2^+$, and $(\text{CO}_2)_3^+$ in the region 650-950 Å are plotted to Figs. 1(a), 1(b), and 1(c), respectively. Due to the similarity of the PIE curve for $(\text{CO}_2)_4^+$ to that for $(\text{CO}_2)_3^+$, the PIE curve for $(\text{CO}_2)_4^+$ was not shown here. The IE's of $(\text{CO}_2)_2^+$, $(\text{CO}_2)_3^+$, and $(\text{CO}_2)_4^+$ were determined to be 13.32 ± 0.02 eV (930.5 ± 1.5 Å), 13.24 ± 0.02 eV (936.5 ± 1.5 Å), and 13.18 ± 0.02 eV (941 ± 1.5 Å), respectively [Figs. 2(a), 2(b) and 2(c)].

Recent calculations^{12,13} predicted a staggered parallel configuration for the carbon dioxide dimer with a well depth of 0.059 eV. Using this value and the IE's for CO_2^{+14} and $(\text{CO}_2)_2^+$, the bond dissociation energy for $\text{CO}_2^+ \cdot \text{CO}_2$ was calculated to be 11.8 ± 1.0 kcal/mol. Since the temperature of the CO_2 sample gas is expected to be quite low after the supersonic expansion, this value is taken to be the negative enthalpy change at 0 K for Reaction (1) and compared with previous values in Table I. Values for the enthalpy change of Reaction (1) determined by Meot-Ner and Field¹ and J. V. Headley *et al.*,¹⁵ after converting them to ΔH°_{f0} using arguments similar to those used in Ref. 4, are found to be in good agreement with the value deduced from this experiment. A value of 17.6 ± 2.8 kcal/mol for the bond dissociation energy of $\text{CO}_2^+ \cdot \text{CO}_2$ has also been reported recently by Rakshit and Warneck.¹⁶ However, since the effective temperature of their measurement was unknown, it is difficult to compare with other values.

Assuming the binding energies for $(\text{CO}_2)_2 \cdot \text{CO}_2$ and $(\text{CO}_2)_3 \cdot \text{CO}_2$ to be the same as that for $(\text{CO}_2)_2$, dissociation energies for $(\text{CO}_2)_2^+ \cdot \text{CO}_2$,

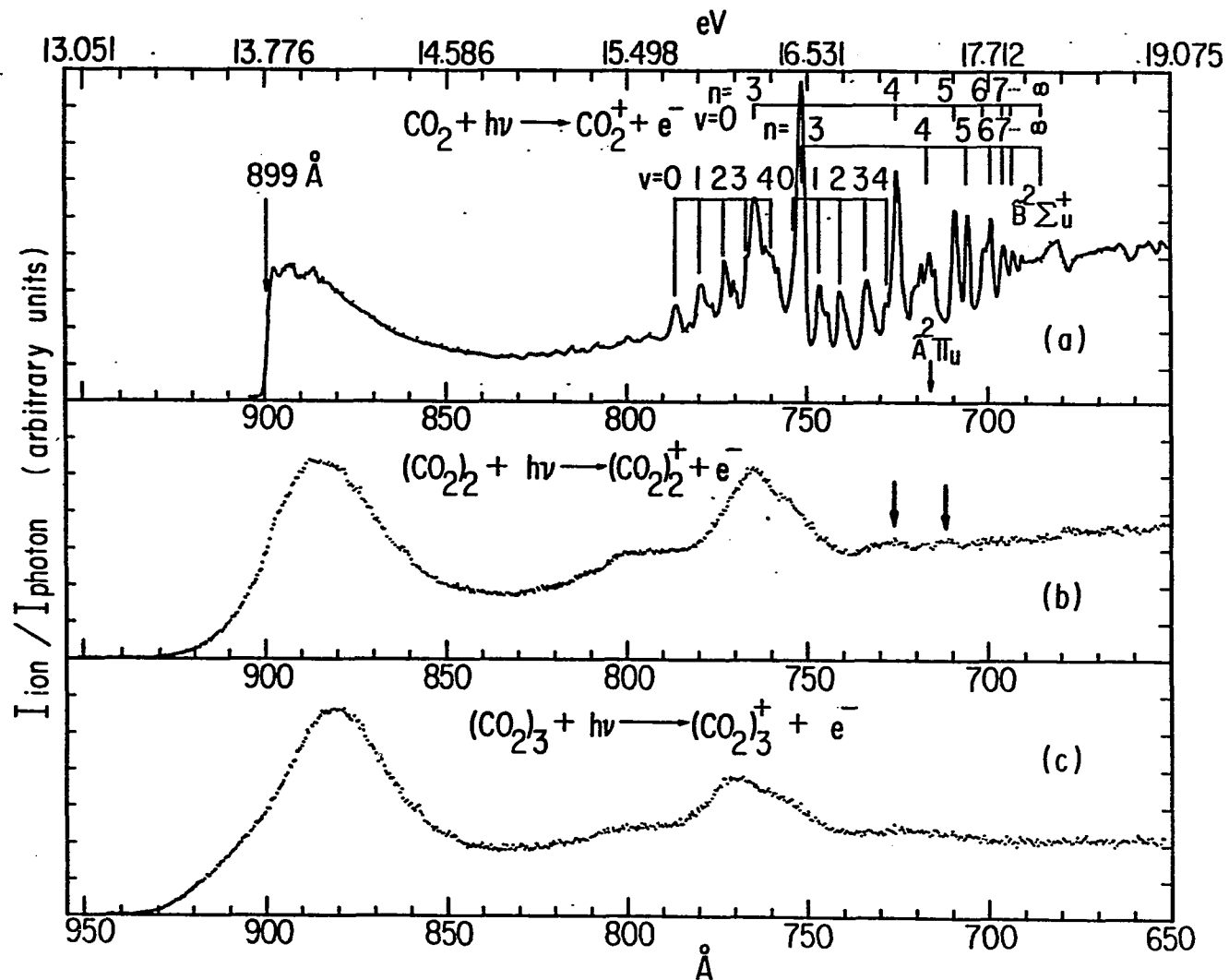


Figure 1. PIE curves for (a) CO_2^+ , (b) $(\text{CO}_2)_2^+$, and (c) $(\text{CO}_2)_3^+$ in the region 650-950 \AA

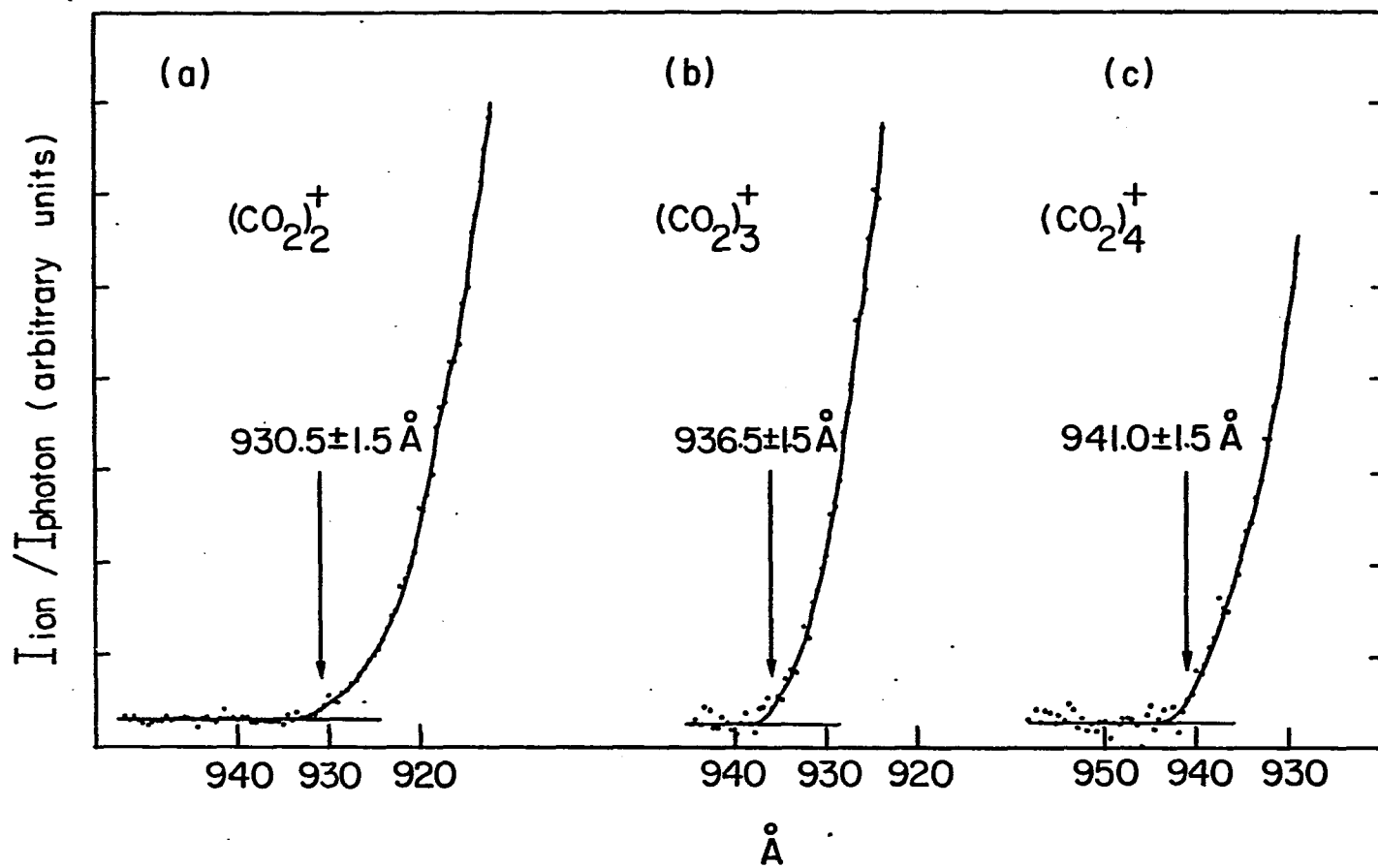


Figure 2. PIE curves for (a) $(\text{CO}_2)_2^+$, (b) $(\text{CO}_2)_3^+$ and (c) $(\text{CO}_2)_4^+$ near the thresholds

Table 1. Bond dissociation energies of $(\text{CO}_2)_{1-3}^+ \cdot (\text{CO}_2)$, $\text{N}_2\text{O}^+ \cdot \text{NO}$ and $\text{NO}^+ \cdot \text{NO}_2$

Ion	This work (kcal/mol)	Other technique ^a (kcal/mol)
$\text{CO}_2^+ \cdot \text{CO}_2$	11.8 ± 1.0	13.0 ± 1.5^b 12.7 ± 0.6^c $\geq 9^d$ 17.6 ± 2.8^e
$(\text{CO}_2)_2^+ \cdot \text{CO}_2$	3.3 ± 1.4	4.8 ± 1.5^b
$(\text{CO}_2)_3^+ \cdot \text{CO}_2$	2.8 ± 1.4	---
$\text{N}_2\text{O}^+ \cdot \text{N}_2\text{O}$	13.1 ± 0.9	---
$\text{NO}^+ \cdot \text{NO}_2$	≥ 5	---

^aValues of Refs. 1 and 15 have been converted to enthalpy change at 0 K using arguments similar to those used in Ref. 4.

^bReference 1.

^cReference 15.

^dReference 2.

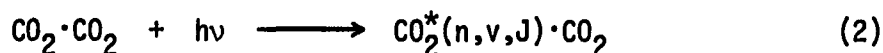
^eReference 16. Effective temperature unknown.

and $(\text{CO}_2)_3^+ \cdot \text{CO}_2$ were calculated to be 3.3 ± 1.4 and 2.8 ± 1.4 kcal/mol, respectively. A value of 4.8 ± 1.5 kcal/mol for $-\Delta H^\circ_{f0}$ of the reaction $\text{CO}_2^+ \cdot \text{CO}_2 + \text{CO}_2 \rightarrow (\text{CO}_2)_3^+$ deduced from the equilibrium constant measurement¹ is again found to be within the limits of error of the binding energy obtained for $(\text{CO}_2)_2^+ \cdot \text{CO}_2$ in the present photoionization study.

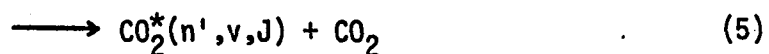
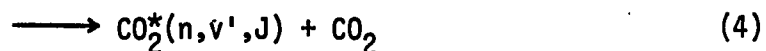
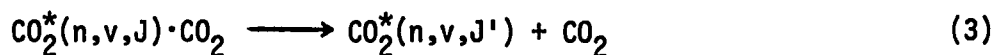
The PIE curve for CO_2^+ obtained here is consistent with that measured previously by Dibeler and Walker^{17,18} using similar wavelength resolution. The rich autoionization structure from 685 to 790 Å are most readily attributable to Rydberg series converging to the $\tilde{\text{B}}^2\Sigma_u^+$ state of CO_2^+ which are labeled "sharp" and "diffuse" series by Tanaka and Ogawa.¹⁹⁻²¹ Since the photoelectron spectrum (PES)^{22,23} of the $\tilde{\text{B}}^2\Sigma_u^+$ band shows a much larger Franck-Condon factor for the (0,0,0) → (0,0,0) transition than the other vibrational transitions, the "sharp" series at 752, 717.4, 706.9, 700.4, and 696.5 Å etc., and the "diffuse" series at 764.7, 726.3, 710.2, 702.2, and 697.6 Å etc. as shown in Fig. 1(a), have all been assigned to $v=0$. Therefore, the autoionization mechanism for these series should be electronic rather than vibrational. Most of the remaining autoionization features in the PIE curve for CO_2^+ originate from the Tanaka-Ogawa¹⁹ series which converges to the $\tilde{\text{A}}^2\Pi_u$ state of CO_2^+ . Each Rydberg member of this series encompasses a progression of vibrational bands with Franck-Condon pattern similar to that observed in the PES of the $\tilde{\text{A}}^2\Pi_u$ band.

The PIE curve for $(\text{CO}_2)_2^+$ shown in Fig. 1(b) is obtained using a higher wavelength resolution and finer wavelength intervals than that used previously.² The peak at 765 \AA probably originates from the vibrational ground state of the $n=3$ Rydberg level of the "diffuse" series. The relative intensity of the peaks observed is opposite to that measured previously.² We have carefully examined the pressure effect on the shape of the PIE curve for $(\text{CO}_2)_2^+$. The PIE curves for $(\text{CO}_2)_2^+$ obtained using a room temperature nozzle at nozzle stagnation pressures of ~ 100 and 1000 Torr, and a cooled nozzle at ~ 246 K operated at ~ 270 Torr²⁴ were all found to be essentially the same as that shown in Fig. 1(b). Therefore, contrary to the conclusion of Ref. 2, we believe that contributions to the PIE curve of $(\text{CO}_2)_2^+$ from photodissociative ionization processes of higher clusters are not significant in this wavelength region. Weak structures observed previously at 727.7 and 711.7 \AA (Table 1 of Ref. 2) are also resolved here as marked in Fig. 1(b). The broader appearance of the peaks in comparison to that shown in Fig. 2 of Ref. 2 is partly due to the finer wavelength intervals used in this experiment, which results in an expansion of the horizontal scale in our plot. According to Fig. 1(b), it is difficult to determine the positions of these two broad peaks to better than $\pm 1.5 \text{ \AA}$. The feature at $\sim 712 \text{ \AA}$ probably has contributions from the $n=5$ Rydberg states of the "diffuse" and "sharp" series. The much weaker Rydberg features observed in the PIE curve for $(\text{CO}_2)_2^+$ as

compared to those resolved in the PIE curve for CO_2^+ indicates that excited Rydberg dimers formed by the photoexcitation process²⁵



in this wavelength region are strongly dissociative. Here n , v , and J represent the principal, vibrational and rotational quantum numbers, respectively. The redistribution of internal energies from the initially excited moiety of the complex to the van der Waals bond must eventually lead to dissociation of these excited dimers. Possible dissociation processes (3), (4) and (5) listed below

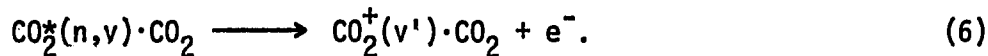


which involve the redistributions of rotational, vibrational and electronic energies are known as rotational, vibrational and electronic predissociations, respectively. In view of the efficient rotational relaxation in a supersonic expansion and the rotational selection rule for photoexcitation processes, one would expect process (3) to be a minor dissociation mechanism. Vibrationally excited Rydberg complexes, $\text{CO}_2^*(n, v \geq 1) \cdot \text{CO}_2$, can be formed by process (2) involving vibrationally excited members of the Tanaka-Ogawa Rydberg series. Since the amount of energy ($\sim 0.1-0.2$ eV)²⁶ required to dissociate the excited Rydberg dimer is less than or of the order of a vibrational quantum of CO_2^+ ,

vibrational predissociation (4) is likely to be an important dissociation process. However, for excited Rydberg complexes, $\text{CO}_2^*(n, v=0) \cdot \text{CO}_2$, with one moiety of the dimer excited to members of the "sharp" or "diffuse" series, vibrational predissociation should be excluded from the consideration as an efficient dissociation mechanism. Therefore, following the above arguments, this experiment seems to suggest electronic predissociation to be a major dissociation mechanism of the $\text{CO}_2^*(n) \cdot \text{CO}_2$ excited Rydberg dimers.

If a potential energy barrier exists²⁷ in the interaction potential between $\text{CO}_2^*(n)$ and CO_2 at a shorter intermolecular distance than the equilibrium distance between CO_2 and CO_2 , direct dissociation can also occur as a result of excitation to the side of the barrier outside the well region of the interaction potential for $\text{CO}_2^*(n) \cdot \text{CO}_2$.

Furthermore, one needs to consider possible dissociation processes after autoionization, i.e.,



If $\text{CO}_2^+(v')$ of the dimeric ion formed by autoionization (6) is vibrationally excited ($v' \geq 1$), vibrational predissociation will again be a possible process. According to theoretical prediction,^{28,29} the vibrational energy distribution of $\text{CO}_2^+(v')$ resulting from autoionization is governed by Franck-Condon factors between the vibrational level of the Rydberg state and vibrational levels of the ionic state. For Rydberg levels converging to the $\tilde{A}^2\Pi_u$ and $\tilde{B}^2\Sigma_u^+$ states of CO_2^+ , autoionization

will most likely give rise to CO_2^+ in the $\tilde{X}^2\Pi_g$ ground state. Photoelectron data²² for CO_2 show that the $\tilde{X}^2\Pi_g$ and $\tilde{B}^2\Sigma_u^+$ states are essentially nonbonding in nature, hence they are expected to have the same nuclear configuration. Because of the similarity between potential energy curves of members of the "sharp" and "diffuse" series and that of the $\tilde{B}^2\Sigma_u^+$ state, the Franck-Condon factor for the (0,0,0) \rightarrow (0,0,0) transition should be much larger than other transitions. Since the initially populated Rydberg levels of the "sharp" and "diffuse" series are mainly $v=0$ states, autoionization from these states will produce mostly vibrationless $\text{CO}_2^+(\tilde{X}^2\Pi_g)$ ions. Assuming the autoionization process to be unperturbed in the excited dimer, the dimeric ions formed by process (6) will contain little vibrational energy. Hence, vibrational predissociation of $\text{CO}_2^+(\tilde{X}^2\Pi_g, v'=0) \cdot \text{CO}_2$ is again an unlikely dissociation mechanism here. For vibrationally excited dimeric ions, $\text{CO}_2^+(\tilde{X}^2\Pi_g, v' \geq 1) \cdot \text{CO}_2$, originating from members of the Tanaka-Ogawa series, vibrational predissociation is certainly a possible process.

Nitrous oxide is isoelectronic with carbon dioxide, and the electronic structure of N_2O^+ is similar to that of CO_2^+ . In accordance with the PES of N_2O ,^{22,30} the $\tilde{X}^2\Pi$ and $\tilde{A}^2\Sigma^+$ states of N_2O^+ are also nonbonding in nature. As shown in Fig. 3(a), Rydberg series III and IV,³¹⁻³⁴ which account for most of the prominent autoionization structures in the region 750-850 Å and converge to the $\tilde{A}^2\Sigma^+(0,0,0)$ state of N_2O^+ , all correspond to the vibrational ground state. The general profiles of the

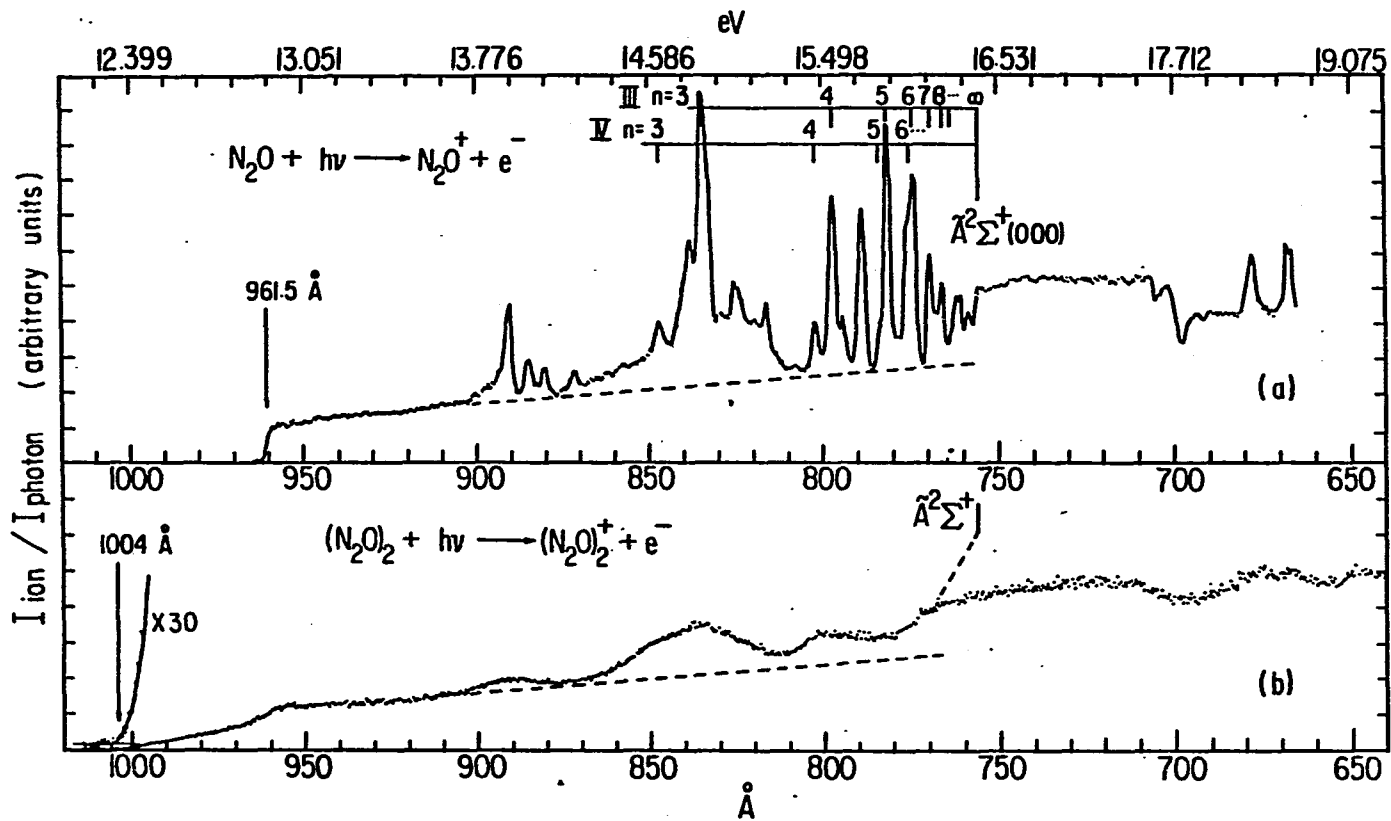


Figure 3. PIE curves for (a) N_2O^+ and (b) $(N_2O)_2^+$ in the region 640-1020 \AA

PIE curves for N_2O^+ and $(N_2O)_2^+$ are quite similar except that structures originating from Rydberg series III and IV are almost completely unobservable in the PIE curve for $(N_2O)_2^+$ [Fig. 3(b)]. Based on the same arguments used above to explain the dissociation mechanism of $CO_2^*(n) \cdot CO_2$, we again conclude that electronic dissociation and/or predissociation are the principal processes responsible for the dissociation of the $N_2O^*(n, v=0) \cdot N_2O$ excited Rydberg dimers.

In fact, experimental observations for $(N_2O)_2^+$ and $(CO_2)_2^+$ presented here are different from those of other linear triatomic systems, such as $(CS_2)_2^+$,⁴ $(OCS)_2^+$, and $(OCS \cdot CS_2)^+$.⁸ The PIE curves for $(CS_2)_2^+$, $(OCS)_2^+$, and $(OCS \cdot CS_2)^+$ show moderately resolved structures correlating to Rydberg states of the monomers. Autoionization structures observed for CS_2^+ and OCS^+ are in general much stronger than those observed for N_2O^+ and CO_2^+ ; this is indicative of faster autoionization processes in CS_2 and OCS than those in N_2O and CO_2 . If electronic predissociation is slow in comparison to autoionization, autoionization structures should be observed in the PIE curve for the dimeric ion. This is probably the case for $(CS_2)_2^+$, $(OCS)_2^+$, and $(OCS \cdot CS_2)^+$. In the cases of $(CO_2)_2^+$ and $(N_2O)_2^+$, the strongly dissociative nature of $CO_2^*(n) \cdot CO_2$ and $N_2O^*(n) \cdot N_2O$ can be attributed to faster electronic predissociation than associative ionization processes, such as process (6). Although vibrational predissociation is believed to be a major dissociation mechanism for $H_2^*(n, v) \cdot H_2$,⁷ $O_2^*(n, v) \cdot O_2$,⁵ $CO^*(n, v) \cdot CO$, $N_2^*(n, v) \cdot N_2$, and $NO^*(n, v) \cdot NO$,⁹ electronic predissociation might still play a role in the dissociation of these excited Rydberg dimers.

The IE of $(\text{N}_2\text{O})_2$ was measured to be 12.35 ± 0.02 eV (1004 ± 1.5 Å) in this study. Using this value, the known IE for N_2O (12.886 ± 0.002 eV)³² and the estimated binding energy (0.02 eV)³⁵ for $(\text{N}_2\text{O})_2$, the bond dissociation energy for $\text{N}_2\text{O}^+ \cdot \text{N}_2\text{O}$ is deduced to be 0.56 ± 0.04 eV. The charge induced dipole interaction is probably not the only interaction term which accounts for the stability of the dimer ions. Nevertheless, it is interesting to note a good correlation of the bond dissociation energies of $(\text{CS}_2)_2^+$ (0.76 eV),⁴ $(\text{OCS})_2^+$ (0.75 eV),⁸ $(\text{SO}_2)_2^+$ (0.66 eV),³⁶ $(\text{N}_2\text{O})_2^+$ (0.56 eV), and $(\text{CO}_2)_2^+$ (0.51 eV) with the polarizabilities of CS_2 (8.7×10^{-24} cm³), OCS (5.7×10^{-24} cm³), SO_2 (3.7×10^{-24} cm³), N_2O (3×10^{-24} cm³), and CO_2 (2.6×10^{-24} cm³).³⁷

The N_3O_2^+ ion is the only ion which originates from the nitrous oxide dimer and has high enough intensity for the measurement of its spectrum. The PIE data for the N_3O_2^+ fragment is depicted in Fig. 4(b) and compared with the PIE curve for the NO^+ fragment from N_2O in Fig. 4(a) in the same wavelength region. Similar to the observation for S_2O_3^+ from $(\text{SO}_2)_2$,³⁶ the PIE curve for N_3O_2^+ was found to have the same curve profile as that of NO^+ except autoionization structures resolved in the NO^+ spectrum are unobservable in the N_3O_2^+ spectrum. This seems to suggest that dissociations of N_2O^+ and $\text{N}_2\text{O}^+ \cdot \text{N}_2\text{O}$ to form $\text{NO}^+ + \text{N}$ and $\text{NO}^+ \cdot \text{N}_2\text{O} + \text{N}$, respectively, follow the same reaction pathway, and the neutral moiety N_2O in $\text{N}_2\text{O}^+ \cdot \text{N}_2\text{O}$ acts like a spectator in the fragmentation process, $\text{N}_2\text{O}^+ \cdot \text{N}_2\text{O} \rightarrow \text{NO}^+ \cdot \text{N}_2\text{O} + \text{N}$.

The appearance energy (AE) for the NO^+ formation from N_2O is found to be at 14.73 eV (842 Å)³⁸ which is well above the thermochemical

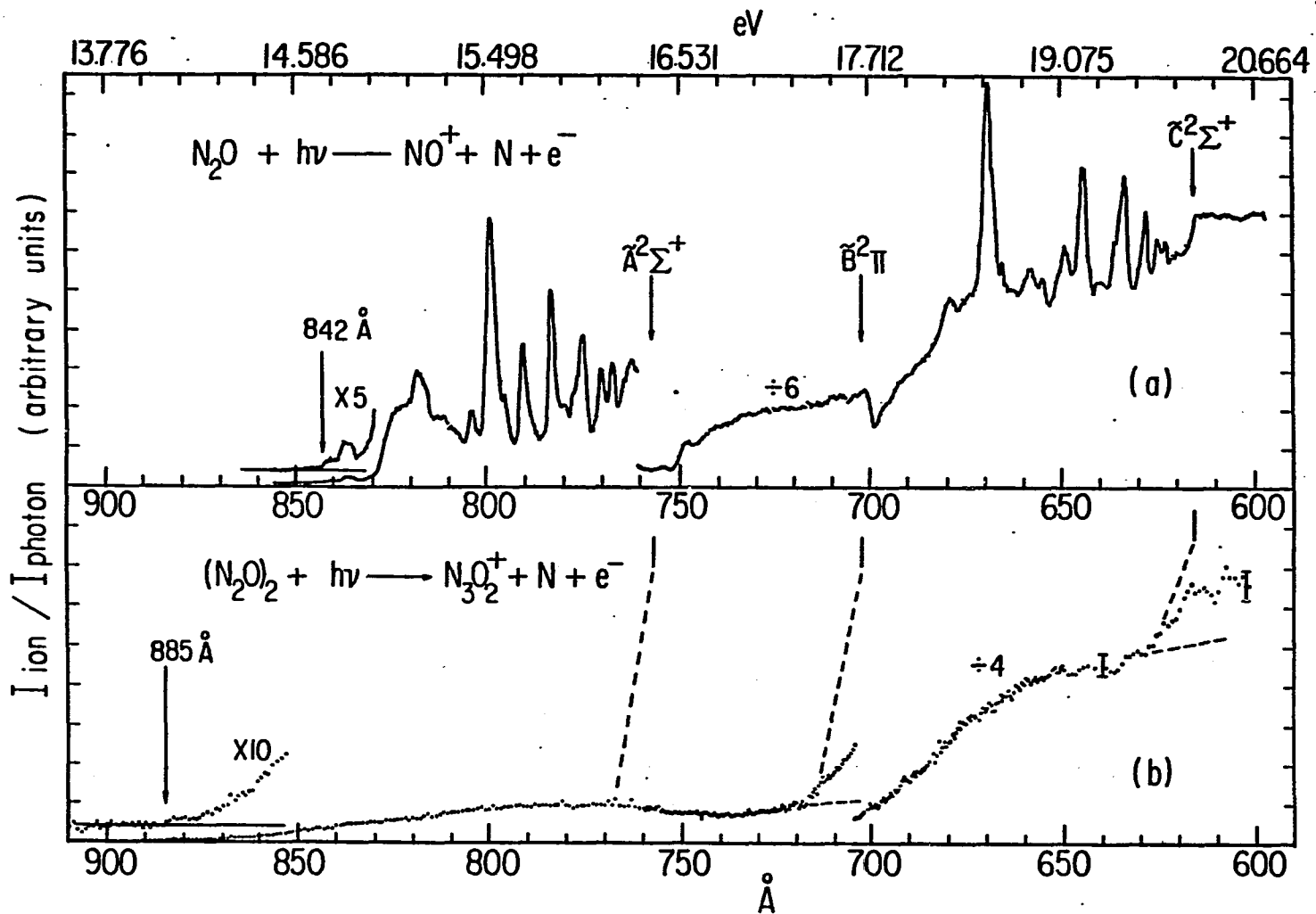


Figure 4. PIE curves for (a) NO^+ and (b) N_3O_2^+ in the region 600-910 \AA

threshold (14.19 eV)³⁹ for the dissociative photoionization process $N_2O + h\nu \rightarrow NO^+ + N + e^-$. If the formations of NO^+ and $N_3O_2^+$ indeed proceed via the same fragmentation pathway, the AE (14.01 eV) for $N_3O_2^+$ determined here probably is not the thermochemical threshold for the process $N_2O \cdot N_2O + h\nu \rightarrow N_3O_2^+ + N + e^-$. From the measured AE of $N_3O_2^+$, the thermochemical threshold for NO^+ from N_2O , and the estimated binding energy for $(N_2O)_2$, a lower bound for the bond dissociation energy for $NO^+ \cdot N_2O$ is calculated to be 0.2 eV.

In the photoionization study of $(CS_2)_2$, thresholds for the $\tilde{B}^2\Sigma_u^+$ and $\tilde{C}^2\Sigma_g^+$ states of CS_2^+ in $(CS_2)_2^+$ are found to be red shifted by ~ 0.16 eV. Apparent increases in PIE for $N_3O_2^+$ at ~ 623 and 713 \AA can be seen in the $N_3O_2^+$ spectrum. Since these features occur at approximately 0.2 eV below the thresholds for the $\tilde{B}^2\Pi$ and $\tilde{C}^2\Sigma^+$ states of N_2O^+ , the positions at 713 and 623 \AA are interpreted as the onsets of the $\tilde{B}^2\Pi$ and $\tilde{C}^2\Sigma^+$ states of N_2O^+ in $N_2O^+ \cdot N_2O$, respectively. The onset for the $\tilde{A}^2\Sigma^+$ state is not evident in the $N_3O_2^+$ spectrum. This is due to the nondissociative nature of the $\tilde{A}^2\Sigma(0,0,0)$ state.⁴⁰ However, a red shift of ~ 0.2 eV for the $\tilde{A}^2\Sigma^+$ state was observed in the PIE curve for $(N_2O)_2^+$.

Though autoionization features are not discernible in the PIE curve for the $N_3O_2^+$ fragment, it is difficult to exclude completely contributions from autoionization. Finite photoionization yields of $N_3O_2^+$ below the threshold for the $\tilde{A}^2\Sigma^+$ state probably arise from vibrationally

excited $\tilde{X}^2\Pi$ ions populated by resonant autoionization processes.

Baer et al.⁴¹ have found that approximately 10% of the autoionization in the region between the $\tilde{X}^2\Pi$ and $\tilde{A}^2\Sigma^+$ states can produce vibrationally excited $\tilde{X}^2\Pi$ ions.

In summary, the binding energies for $\text{CO}_2^+\cdot\text{CO}_2$ and $(\text{CO}_2)_2^+\cdot\text{CO}_2$ deduced from this experiment are in agreement with values obtained previously. The stabilities of $(\text{CO}_2)_4^+$, $(\text{N}_2\text{O})_2^+$ and $\text{NO}^+\cdot\text{N}_2\text{O}$ are determined for the first time. The comparison of the PIE curves for $(\text{CO}_2)_2^+$ and $(\text{N}_2\text{O})_2^+$ with those of CO_2^+ and N_2O^+ , respectively, suggests that electronic predissociation or direct dissociation might be important dissociation mechanisms of the $\text{CO}_2^*(n)\cdot\text{CO}_2$ and $\text{N}_2\text{O}^*(n)\cdot\text{N}_2\text{O}$ excited Rydberg dimers.

REFERENCES

1. M. Meot-Ner (Mautner) and F. H. Field, J. Chem. Phys. 66, 4527 (1977).
2. G. G. Jones and J. W. Taylor, J. Chem. Phys. 68, 1768 (1978).
3. A value of 7.3 kcal/mol for the binding energy of $\text{CO}_2^+ \cdot \text{CO}_2$ was obtained in Ref. 2 by using the wrong sign for the enthalpy of the dimerization reaction.
4. Y. Ono, S. H. Linn, H. F. Prest, M. E. Gress, and C. Y. Ng, J. Chem. Phys. 73, 2523 (1980).
5. S. H. Linn, Y. Ono, and C. Y. Ng, J. Chem. Phys. 74, 3348 (1981).
6. A. O. Nier, W. B. Hanson, A. Seiff, M. B. McElory, N. W. Spencer, R. J. Duckett, T. C. D. Knight, and W. S. Cook, Science 193, 786 (1976).
7. S. L. Anderson, T. Hirooka, P. W. Tiedemann, B. H. Mahan, Y. T. Lee, J. Chem. Phys. 73, 4779 (1980).
8. Y. Ono, E. A. Osuch, and C. Y. Ng, J. Chem. Phys. 74, 1645 (1981).
9. S. H. Linn, Y. Ono, and C. Y. Ng, J. Chem. Phys. 74, 3342 (1981).
10. Y. Ono, S. H. Linn, H. F. Prest, C. Y. Ng, and E. Miescher, J. Chem. Phys. 73, 4855 (1980).
11. K. E. Schubert and R. D. Hudson, Report Number ATN-64 (9233-2), Aerospace Corp., Los Angeles, 1973.
12. A. Koide and T. Kihara, Chem. Phys. 5, 34 (1974).
13. N. Brigot, S. Odier, S. H. Walmsley, and J. L. Whitten, Chem. Phys. Lett. 49, 157 (1977).

14. K. E. McCulloh, *J. Chem. Phys.* 59, 4250 (1973).
15. J. V. Headley, R. S. Mason, and K. R. Jennings, presented at the 28th Annual Conference on Mass Spectrometry and Allied Topics, New York, N.Y., May 25-30, 1980.
16. A. B. Rakshit and P. Warneck, *Int. J. Mass Spectrom. Ion Phys.* 35, 23 (1980).
17. V. H. Dibeler and J. A. Walker, *J. Opt. Soc. Am.* 57, 1007 (1967).
18. For high resolution PIE curve for CO_2^+ , see J. Berkowitz, "Photoabsorption, Photoionization, and Photoelectron Spectroscopy", (Academic Press, New York, 1979), p. 251.
19. Y. Tanaka and M. Ogawa, *Can. J. Phys.* 40, 879 (1962).
20. Y. Tanaka, A. S. Jursa, and F. J. LeBlanc, *J. Chem. Phys.* 32, 1199 (1960).
21. H. J. Henning, *Ann. Phys. (Leipzig)* 13, 599 (1932).
22. C. R. Brundle and D. W. Turner, *Int. J. Mass Spectrom. Ion Phys.* 2, 195 (1969); D. W. Turner, C. Baker, A. D. Baker, and C. R. Brundle, "Molecular Photoelectron Spectroscopy", (Wiley-Interscience, London, 1970).
23. J. H. D. Eland and C. J. Danby, *Int. J. Mass Spectrom. Ion Phys.* 1, 111 (1968).
24. At these nozzle conditions, Jones et al. found the PIE curve for $(\text{CO}_2)_2^+$ increased at higher photon energy. This change was attributed to contributions from photodissociative ionization of higher clusters (see Ref. 2).

25. Since the binding between the two moieties of a van der Waals dimer is very weak, to a good approximation, photoexcitation of the dimer can be viewed as exciting one of the moieties making up the dimer.
26. The binding energy of $\text{CO}_2^*(n) \cdot \text{CO}_2$ is expected to be similar to that of $\text{CO}_2^+ \cdot \text{CO}_2$. However, due to the difference in geometry of $(\text{CO}_2)_2$ and $\text{CO}_2^*(n) \cdot \text{CO}_2$, $\text{CO}_2^*(n) \cdot \text{CO}_2$ formed by the vertical excitation [process (2)] will be close to the asymptotic region of the potential energy curve for $\text{CO}_2^*(n) + \text{CO}_2$ and can be dissociated with less energy than the actual binding energy of $\text{CO}_2^*(n) \cdot \text{CO}_2$. A more detailed discussion of the excitation process for van der Waals dimer is given in Ref. 4.
27. For rare gas dimers, both experiment and theoretical calculations suggest the existence of potential energy barriers in their Rydberg states. See Y. Tanaka and W. C. Walker, J. Chem. Phys. 74, 2760 (1981), J. S. Cohen and B. Schneider, J. Chem. Phys. 61, 3230 (1974), and R. S. Mulliken, J. Chem. Phys. 52, 5170 (1970).
28. J. N. Bradzley, Chem. Phys. Lett. 2, 329 (1968).
29. A. L. Smith, Phil. Trans. Roy. Soc. Lond. A 268, 169 (1970).
30. P. Natalis and J. E. Collin, Int. J. Mass Spectrom. Ion Phys. 2, 222 (1969).
31. Y. Tanaka, A. S. Jursa and F. J. LeBlanc, J. Chem. Phys. 32, 1205 (1960).
32. J. Berkowitz and J. H. D. Eland, J. Chem. Phys. 67, 2740 (1977).

33. P. Coppens, J. Smets, M. G. Fishel, and J. Drowart, *Int. J. Mass Spectrom. Ion Phys.* 14, 57 (1974).
34. V. H. Dibeler and J. A. Walker, *Advan. Mass Spectrom.* 4, 767 (1967);
V. H. Dibeler, J. A. Walker and S. K. Liston, *J. Res. NBS* 71A,
371 (1967).
35. H. L. Johnston and K. E. McCloskey, *J. Phys. Chem.* 44, 1038 (1940);
M. Trautz and F. Kurz, *Ann. Phys.* 9, 981 (1931).
36. J. Erickson and C. Y. Ng, *J. Chem. Phys.* 75, 1650 (1981).
37. J. O. Hirschfelder, C. F. Curtiss, and R. B. Bird, "Molecular
Theory of Gases and Liquids" (Wiley, New York, 1964), p. 950.
38. The A.E. for NO^+ observed here is in good agreement with the
value (~ 14.78 eV) obtained by Berkowitz and Eland. See Ref. 32.
39. Energetics of Gaseous Ions, in "J. Phys. Chem. Ref. Data", edited by
H. M. Rosenstock, K. Draxl, B. W. Steiner, and J. T. Herron (Natl.
Bur. Stand., Washington, D.C., 1977), Vol. 6, Suppl. 1.
40. J. H. D. Eland, *Int. J. Mass Spectrom. Ion Phys.* 12, 389 (1973);
Spectrom. Ion Phys. 13, 251 (1974).
41. T. Baer, P.-M. Guyon, I. Nenner, A. Tabché-Fouhaillé, R. Botter,
L. F. A. Ferriera, and T. R. Govers, *J. Chem. Phys.* 70, 1585 (1979).

SECTION IV.

MOLECULAR BEAM PHOTOIONIZATION STUDY
OF CO, N₂, AND NO DIMERS AND CLUSTERS

ABSTRACT

Photoionization efficiency (PIE) data for $(\text{CO})_2^+$, $(\text{N}_2)_2^+$, and $(\text{NO})_2^+$ have been obtained near the thresholds using the molecular beam method. The ionization energies (IE) for $(\text{CO})_2$, $(\text{N}_2)_2$, and $(\text{NO})_2$ were measured to be 13.05 ± 0.04 eV (950 ± 3 Å), 14.69 ± 0.05 eV (844 ± 3 Å) and 8.736 ± 0.002 eV (1419.2 ± 0.3 Å), respectively. Using these values, the known IEs for CO, N_2 , and NO, and the estimated binding energies for $(\text{CO})_2$, $(\text{N}_2)_2$, and $(\text{NO})_2$, the bond dissociation energies for $\text{CO}^+ \cdot \text{CO}$, $\text{N}_2^+ \cdot \text{N}_2$, and $\text{NO}^+ \cdot \text{NO}$ were deduced to be 0.97 ± 0.04 eV, 0.90 ± 0.05 eV, and 0.598 ± 0.006 eV, respectively. From the analysis of the PIE curve for $(\text{NO})_2^+$, the IEs of $(\text{NO})_2$ to $\text{NO}^+(\tilde{X}^1\Sigma^+, v=1) \cdot \text{NO}$ and $\text{NO}^+(\tilde{X}^1\Sigma^+, v=2) \cdot \text{NO}$ were determined to be 8.997 ± 0.007 eV (1378 ± 1 Å) and 9.253 ± 0.013 (1340 ± 2 Å), respectively. This measurement supports the conclusion that the bonding of NO^+ in $\text{NO}^+ \cdot \text{NO}$ is stronger than that of NO, but weaker than that of NO^+ . The IEs for $(\text{CO})_3$, $(\text{N}_2)_3$, and $(\text{NO})_{n=3-6}$ were also measured.

INTRODUCTION

One of the most accurate and commonly used methods for determining the binding energy between a neutral molecule A and a molecular ion B^+ is the pulsed high pressure mass spectrometric technique.¹ This method generally involves the measurements of the temperature variation of the equilibrium constant (K) for the association reaction



From the slope of a $\log K$ vs $1/T$ plot, the enthalpy change (ΔH_T) for Reaction (1) can be obtained. In the case when only one equilibrium constant is measured at a specific temperature, ΔH_T can be deduced from an estimate of the entropy change for Reaction (1).

Since the accuracy for the measurements of K requires comparable concentrations of A^+ and AB^+ , the experimental conditions are usually selected by raising the temperature of the ion source such that the forward and reverse reactions of Reaction (1) are very fast and the equilibrium can be attained in a reasonably short time. If the bond energy for AB^+ is strong (>20 kcal/mol), the ion source has to be maintained at temperatures ≥ 700 K in order to fulfill the above requirement.² However, as a result of the limited temperature range and delay times attainable with a particular instrument, this method is therefore only applicable to dimeric ions having relatively low binding energies. In a high pressure mass spectrometric study of the association reaction



Meot-Ner and Field² found that equilibrium could not be reached in Reaction (2) at the highest temperature (695 K) and the longest delay times obtainable with their instrument. Their study only led to a lower bound for $-\Delta H_{695\text{K}}$ for Reaction (2).

It has been shown³ that molecular beam photoionization of van der Waals dimers and clusters is an excellent method for the determination of ion-neutral interaction potentials. Since this method does not suffer from the above limitation, we have performed a photoionization study of CO dimer and trimer. PIE data for N_2 , NO dimers and clusters are also presented in this report. From the measured ionization energies (IE) for $(\text{CO})_2$, $(\text{N}_2)_2$ and $(\text{NO})_2$, we were able to deduce the bond energies for $\text{CO}^+\cdot\text{CO}$, $\text{N}_2^+\cdot\text{N}_2$ and $\text{NO}^+\cdot\text{NO}$. The photoionization data for $(\text{NO})_2^+$ are obtained in this experiment with higher wavelength resolution than that used previously.⁴

EXPERIMENTAL

The experimental arrangement and procedures are essentially the same as those described previously.^{3,5} Briefly, the apparatus consists of a 3-m near normal incidence VUV monochromator (McPherson 2253M), a supersonic molecular beam production system, a capillary discharge light source, a VUV light detector and a quadrupole mass spectrometer for ion detection. The gratings employed in this study are Bausch and Lomb 1200 1/mm MgF_2 or Os coated aluminum gratings blazed at 1360 Å.

The carbon monoxide ($\geq 99.99\%$ purity), nitrogen ($\geq 99.99\%$ purity), and nitric oxide ($\geq 99\%$ purity) used in this experiment were obtained from Matheson. The CO, N_2 and NO molecular beams were produced by supersonic expansion through a 0.05 mm diameter stainless steel nozzle. A schematic diagram of the nozzle design was shown in Fig. 2 of Ref. 3. By controlling the feeding rate of liquid nitrogen and the input power of the heater, the stagnation temperature of the nozzle can be varied from ≈ 90 K to ≈ 600 K. During the experiments, the stagnation temperatures for the N_2 and CO beams were kept at ≈ 110 K whereas that of the NO beam was maintained at ≈ 150 K. The stabilities of the temperatures were found to be better than ± 5 K as monitored with a thermocouple. In order to optimize the intensities of different clusters, the nozzle stagnation pressure was varied in the range from ≈ 300 to ≈ 1500 Torr.

The photoionization efficiency (PIE) curve for $(\text{NO})_2^+$ near the threshold (1365-1425 Å), obtained using an optical resolution of 0.28 Å (FWHM), is shown in Fig. 2(b). These PIE data were the average of four independent scans. Data are plotted at intervals of 0.1 Å. The remaining PIE curves were obtained in this study using 500 μm entrance and exit slits so that the resolution achieved was 1.4 Å (FWHM). Data are plotted at intervals of 0.5 Å. Each PIE curve was based on at least two scans, and the prominent structures in the curves were found to be reproducible. Wavelength calibrations were achieved by using known atomic resonance lines, or H₂ emission lines⁶ when the H₂ pseudocontinuum was used.

RESULTS AND DISCUSSION

The PIE curves for $(\text{CO})_2^+$ and CO^+ are compared in Fig. 1. The PIE curves for $(\text{N}_2)_2^+$ and N_2^+ are shown in Figs. 2(a) and 2(b), respectively. The PIE curves obtained for CO^+ and N_2^+ are consistent with those reported previously.^{7,8} In contrast to the rich autoionization features observed in the CO^+ and N_2^+ spectra, the PIE curves for $(\text{CO})_2^+$ and $(\text{N}_2)_2^+$ are structureless. This observation suggests that after the excitation process, $\text{CO}\cdot\text{CO}$ [or $\text{N}_2\cdot\text{N}_2$] + $h\nu \rightarrow \text{CO}^*(n,v)\cdot\text{CO}$ [or $\text{N}_2^*(n,v)\cdot\text{N}_2$], the excited dimers $\text{CO}^*(n,v)\cdot\text{CO}$ [or $\text{N}_2^*(n,v)\cdot\text{N}_2$] are strongly dissociative, and the reaction probability of forming the $(\text{CO})_2^+$ [or $(\text{N}_2)_2^+$] dimeric ions by the associative ionization process $\text{CO}^*(n,v)\cdot\text{CO} \rightarrow \text{CO}^+\cdot\text{CO} + e^-$ is negligible.⁹ Similar observations are found for $\text{O}_2^*(n,v)\cdot\text{O}_2$ ¹⁰ and $\text{NO}^*(n,v)\cdot\text{NO}$ ¹¹ prepared in this wavelength region.

Since the excited ionic states for CO^+ , N_2^+ , NO^+ , and O_2^+ in this region have equilibrium bond distances quite different from those of their ground ionic states,¹² Rydberg levels converging to these excited ionic states, which are manifested as major autoionization peaks in the PIE curves of these ions, are likely to be vibrationally excited states. Since one expects that the dissociation energies for these excited dimers are smaller than the vibrational energy contents of the ion cores, it is reasonable to believe that vibrational pre-dissociation is the main dissociation mechanism of these vibrationally

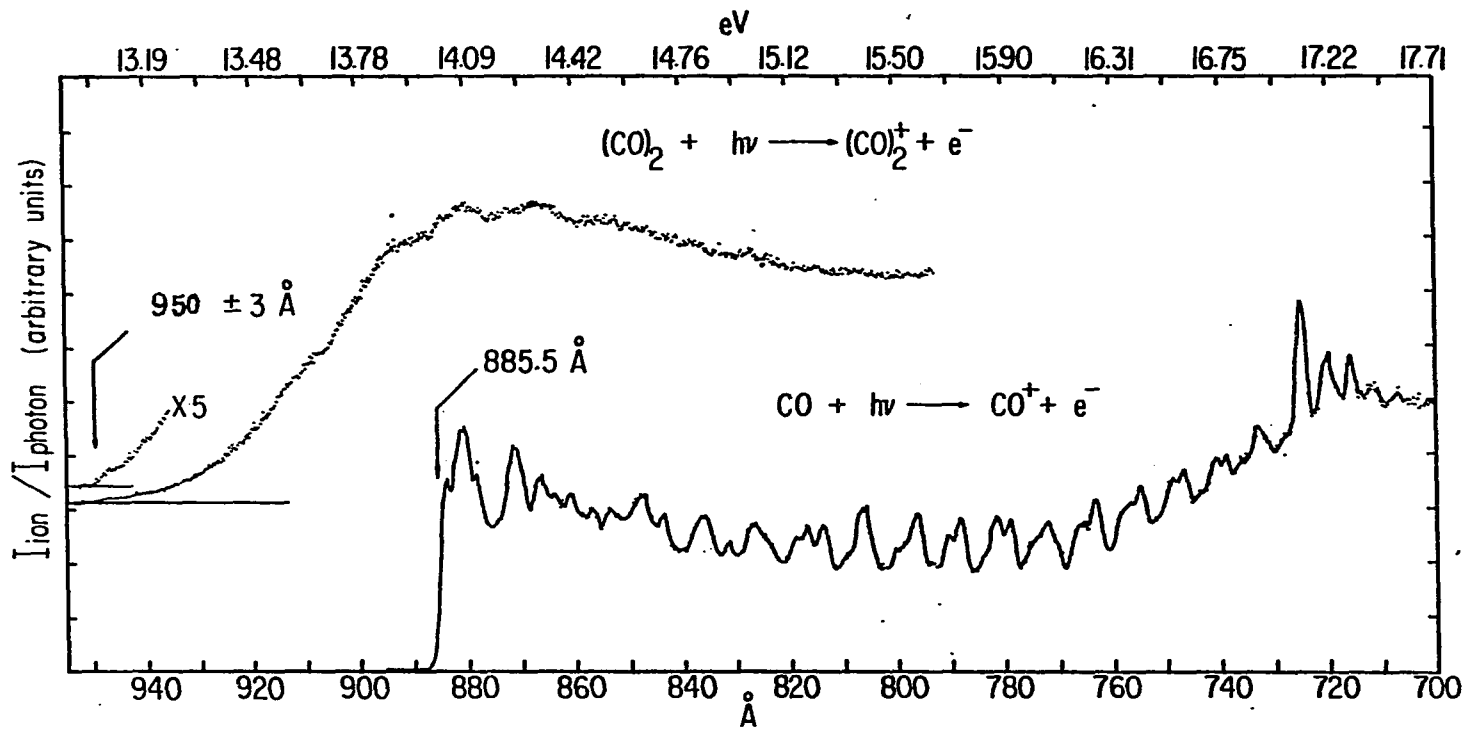


Figure 1. PIE curve for $(\text{CO})_2^+$ and CO^+ in the range 700-955 Å

excited Rydberg dimers. Considering associative ionization and predissociation to be competing processes, these observations can also be taken as evidence that the lifetimes for the vibrational predissociation processes of these excited dimers are shorter than the autoionization lifetimes of the corresponding Rydberg states.¹³ By contrast, in the cases of $(\text{CS}_2)_2$, ArCS_2 ,³ $(\text{OCS})_2$, and $\text{OCS}\cdot\text{CS}_2$,¹⁴ where the excited Rydberg levels involved are essentially nonbonding in nature, the ion cores of these excited Rydberg dimers are mainly in their vibrational ground states. Therefore, vibrational predissociation will not be an efficient dissociation process for these excited Rydberg dimers. The relatively well-resolved autoionization features observed in the PIE curves for these dimeric ions seem to support the above arguments.

As shown in Figs. 1 and 2(a), the PIE for $(\text{CO})_2^+$ and $(\text{N}_2)_2^+$ decrease exponentially toward the ionization thresholds. The IEs for $(\text{CO})_2$ and $(\text{N}_2)_2$ are determined to be 13.05 ± 0.04 eV (950 ± 3 Å) and 14.69 ± 0.05 eV (844 ± 3 Å), respectively. Using these values, the known IEs for CO (14.013 ± 0.004 eV)¹⁵ and N_2 (15.5803 eV),^{16,17} and the estimated dissociation energies for $(\text{CO})_2$ (0.008 eV)¹⁸ and $(\text{N}_2)_2$ (0.007 eV),¹⁸ the bond energies for $\text{CO}^+\cdot\text{CO}$ and $\text{N}_2^+\cdot\text{N}_2$ are calculated to be 0.97 ± 0.04 eV (22.4 ± 1.0 kcal/mol) and 0.90 ± 0.05 eV (20.8 ± 1.2 kcal/mol), respectively. Because of the high degree of rotational and low frequency vibrational relaxation in the supersonic expansion, these values can be taken to be the enthalpy changes for the corresponding

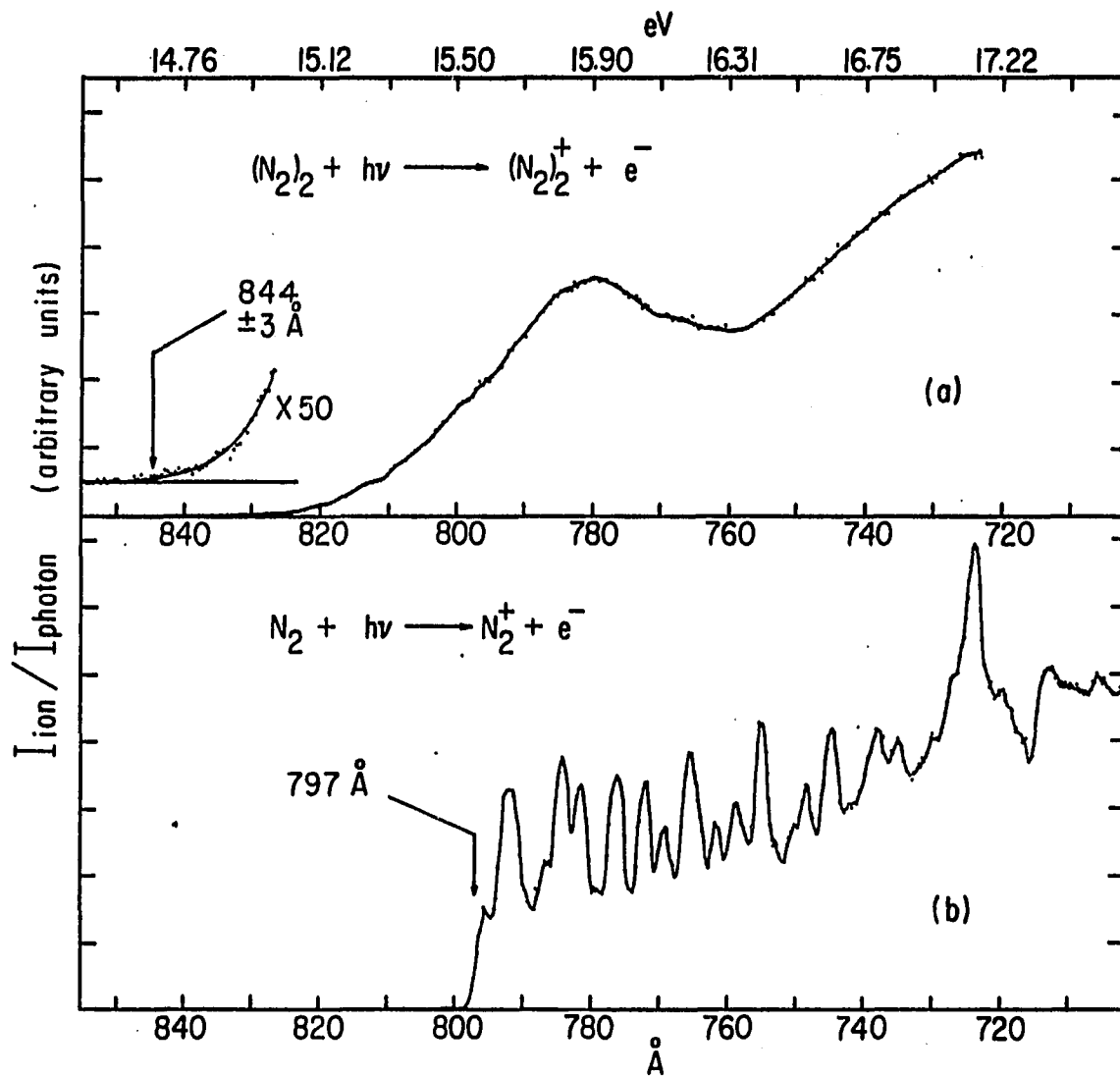


Figure 2. PIE curves for (a) $(N_2)_2$ and (b) N_2^+ in the range 700-855 Å

ion/molecule association reactions at 0 K. The enthalpy change at ~ 770 K for the association reaction



has been measured previously by Payzant and Kebarle¹⁹ to be -22.8 kcal/mol. From the apparent equilibrium constant measured at 695 K, Meot-Ner and Field² obtained a lower bound of ≤ 25.4 kcal/mol for $-\Delta H_{695\text{K}}$ of (2). In order to compare these values with the results of this experiment, these values have been converted to $-\Delta H_0$ K using arguments similar to those used in Ref. 3. As shown in Table I, the bond energy for $\text{CO}^+ \cdot \text{CO}$ derived from this work is consistent with the estimate by Meot-Ner et al. Good agreement can also be seen between the values obtained here and those measured by Chong and Franklin.²⁰

The PIE curves for $(\text{CO})_3^+$ and $(\text{N}_2)_3^+$ have also been measured in this wavelength region. Since these curves are similar in shape to the dimer curves, they are not shown here. The IEs for $(\text{CO})_3$ and $(\text{N}_2)_3$ were determined to be 12.91 ± 0.04 eV (961 ± 3 Å) and 14.64 ± 0.05 eV (847 ± 3 Å), respectively. Assuming the binding energies for $(\text{CO})_2 \cdot \text{CO}$ and $(\text{N}_2)_2 \cdot \text{N}_2$ to be the same as those of the dimers, the binding energies for $(\text{CO})_2^+ \cdot \text{CO}$ and $(\text{N}_2)_2^+ \cdot \text{N}_2$ are deduced to be 0.16 ± 0.08 eV and 0.06 ± 0.10 eV, respectively. The charge-dipole interactions in $\text{CO}^+ \cdot \text{CO}$ and $(\text{CO})_2^+ \cdot \text{CO}$ are probably responsible for the slightly higher bond dissociation energies observed for $\text{CO}^+ \cdot \text{CO}$ and $(\text{CO})_2^+ \cdot \text{CO}$ than those for $\text{N}_2^+ \cdot \text{N}_2$ and $(\text{N}_2)_2^+ \cdot \text{N}_2$.

Table I. Bond energies of $\text{CO}^+\cdot\text{CO}$, $\text{N}_2^+\cdot\text{N}_2$ and $\text{NO}^+\cdot\text{NO}$

Ion	This work (kcal/mol)	Other technique ^a (kcal/mol)
$\text{CO}^+\cdot\text{CO}$	22.4 ± 1.0	26 ± 7^b $\geq 21.2^c$
$\text{N}_2^+\cdot\text{N}_2$	20.8 ± 1.2	27 ± 7^b 18.2^d
$\text{NO}^+\cdot\text{NO}$	13.79 ± 0.14	13.6 ± 0.5^e

^aValues of Refs. 20, 2 and 19 have been converted to enthalpy changes at 0 K using arguments similar to that used in Ref. 3.

^bReference 20.

^cReference 2.

^dReference 19.

^eReference 4.

Figure 3 shows the PIE curve for $(\text{NO})_2^+$ in the range 1235-1425 Å obtained using an optical resolution of 1.4 Å (FWHM). As a consequence of improved intensity of $(\text{NO})_2$ in the beam and higher sensitivity of the present apparatus, the counting rate for $(\text{NO})_2^+$ is more than two orders of magnitude higher than that obtained in the previous experiment.⁴ The general profile of the PIE curve for $(\text{NO})_2^+$ [Fig. 3] is in good agreement with previous measurements. Due to substantial improvement in the signal to noise ratio a change in slope can now be seen at ~1330-1340 Å. The three steps resolved in the dimer curve are quite gradual and extend over ~6 Å. The PIE data for $(\text{NO})_2^+$ [Fig. 4(b)] obtained using a wavelength resolution of 0.28 Å (FWHM) seem to reveal finer step-like structures at the onset. Supersonic expansion has been known to be very effective in the relaxation of rotational and low frequency vibrational excitations. Furthermore, the recent photoionization study of NO by Ono *et al.*⁵ also suggests that the relaxation from the low lying $^2\Pi_{3/2}$ state to ground $\tilde{X}^2\Pi_{1/2}$ state of NO is efficient. Therefore, it is quite possible that these structures might arise from the excitations of the low frequency vibrational modes of $(\text{NO})_2^+$. Presently, experimental set ups which will allow the measurements of the $(\text{NO})_2^+$ ions in coincidence with threshold (zero kinetic energy) electrons are in progress in our laboratory. We expect that the coincidence experiment will be helpful in assigning these step-like structures.

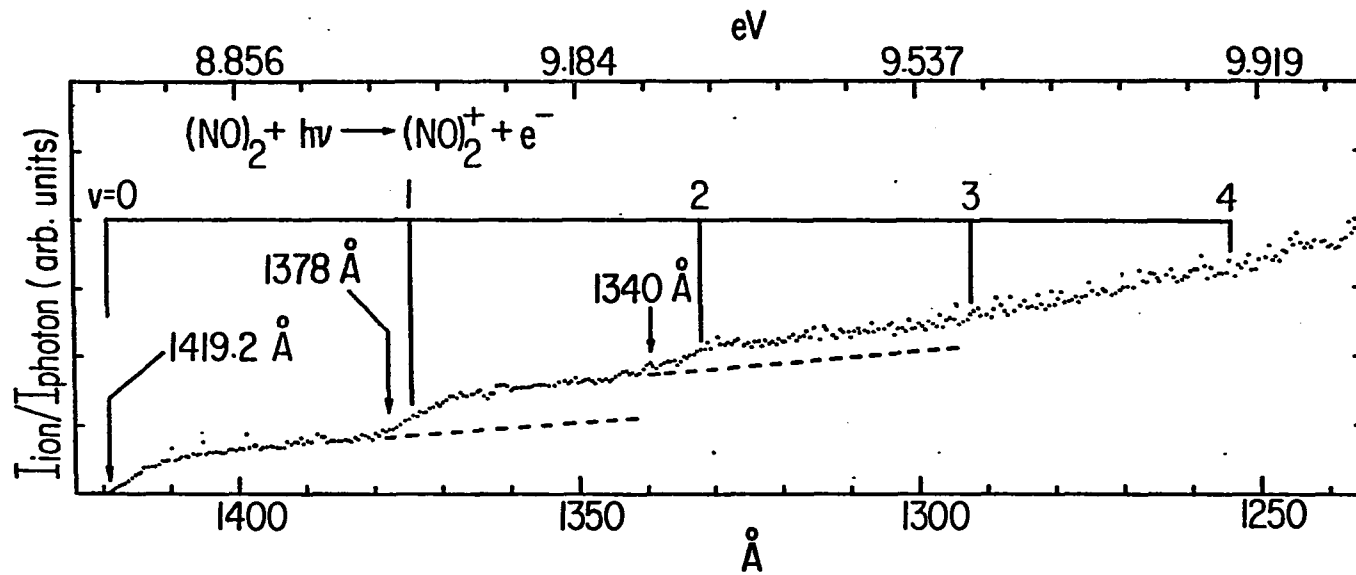


Figure 3. PIE curve for $(\text{NO})_2^+$ in the range 1235-1425 \AA

Assuming the efficient relaxation of rotational, low frequency vibrational, and low lying electronic excitations, the IE for $(\text{NO})_2$ is determined to be 8.736 ± 0.002 eV (1419.2 ± 0.3 Å). The uncertainty of this value is taken to be the largest difference of the results of four scans. Using this value, the known IE (9.265 eV)²¹ for NO and the binding energy (0.069 ± 0.004 eV)²² for $(\text{NO})_2$, the bond energy for $\text{NO}^+ \cdot \text{NO}$ is deduced to be 0.598 ± 0.006 eV.

To a first approximation, one should expect the separations in energy of the IEs of $(\text{NO})_2$ to $\text{NO}^+(\tilde{X}^1 \Sigma^+, v=0) \cdot \text{NO}$, $\text{NO}^+(\tilde{X}^1 \Sigma^+, v=1) \cdot \text{NO}$ and $\text{NO}^+(\tilde{X}^1 \Sigma^+, v=2) \cdot \text{NO}$ to be equal to the corresponding separations in the IEs of NO to $\text{NO}^+(\tilde{X}^1 \Sigma^+, v=0)$, $\text{NO}^+(\tilde{X}^1 \Sigma^+, v=1)$ and $\text{NO}^+(\tilde{X}^1 \Sigma^+, v=2)$. In Fig. 3, we have shifted the positions of the onsets for $\text{NO}^+(\tilde{X}^1 \Sigma^+, v=0, 1, 2, 3, \text{ and } 4)$ by 0.529 eV, which is the difference of the IEs for $(\text{NO})_2$ and NO, and compared them with the structure observed in the PIE curve for $(\text{NO})_2^+$. This comparison clearly suggests the second and third steps should be assigned as the onsets for $\text{NO}^+(\tilde{X}^1 \Sigma^+, v=1) \cdot \text{NO}$ and $\text{NO}^+(\tilde{X}^1 \Sigma^+, v=2) \cdot \text{NO}$, respectively. The observation of the third step in the PIE curve for $(\text{NO})_2^+$ does not contradict previous arguments concerning the efficient dissociation of energetically unstable $\text{NO}^+ \cdot \text{NO}$ dimeric ions. On the contrary, since the binding energy (0.598 ± 0.006 eV) determined in this experiment is larger than the difference in energy (0.577 eV)^{5, 23} of the IEs of NO to $\text{NO}^+(\tilde{X}^1 \Sigma^+, v=2)$ and $\text{NO}^+(\tilde{X}^1 \Sigma^+, v=0)$, $\text{NO}^+(\tilde{X}^1 \Sigma^+, v=2) \cdot \text{NO}$ is expected to be bound. We

note that the relative height of the third step in comparison to the first and second steps in $(\text{NO})_2^+$ is smaller than the relative step heights (or Franck-Condon factors) corresponding to the excitations of the $\tilde{X}^1\Sigma^+, v=0,1$ and 2 states of NO^+ resolved in the PIE curve for NO^+ .⁵

The IEs of $(\text{NO})_2$ to $\text{NO}^+(\tilde{X}^1\Sigma^+, v=1) \cdot \text{NO}$ and $\text{NO}^+(\tilde{X}^1\Sigma^+, v=2) \cdot \text{NO}$ are determined to be 8.997 ± 0.007 eV (1378 ± 1 Å) and 9.253 ± 0.013 eV (1340 ± 2 Å), respectively. The vibrational spacings, $\Delta v=0-1$ and $1-2$ are 0.261 ± 0.008 eV and 0.256 ± 0.020 , respectively (Table II). Since the hot band effects would lower the values of all thresholds by the same amount, the values of these vibrational spacings should not be affected even when the relaxation of the low lying excited states is incomplete in this experiment. Interestingly, as shown in Table II, these values are found to be larger than the corresponding spacings in $\text{NO}(\tilde{X}^2\Pi)$,²⁴ but smaller than those in $\text{NO}^+(\tilde{X}^1\Sigma^+)$.^{5,23} Since the ionization of $\text{NO}(\tilde{X}^2\Pi)$ to form $\text{NO}^+(\tilde{X}^1\Sigma^+)$ involves the removal of an antibonding electron from the π^* molecular orbital, the larger vibrational spacing in $\text{NO}^+(\tilde{X}^1\Sigma^+)$ than that in $\text{NO}(\tilde{X}^2\Pi)$ simply indicates an increase in bond strength in $\text{NO}^+(\tilde{X}^1\Sigma^+)$ as the result of the ionization process. Therefore, this observation supports the conclusion that the bonding of NO^+ in $\text{NO}^+ \cdot \text{NO}$ is stronger than that of NO and weaker than that of NO^+ .

The PIE curves for $(\text{CO})_2^+$, $(\text{N}_2)_2^+$ and $(\text{O}_2)_2^+$ ¹⁰ near the thresholds are all found to tail away gradually toward their onsets. This

Table II. Comparison of the vibrational spacings of $\text{NO}^+(\tilde{X}^1\Sigma^+,v)\cdot\text{NO}$, $\text{NO}^+(\tilde{X}^1\Sigma^+,v)$ and $\text{NO}(\tilde{X}^2\Pi)$

Δv	$\text{NO}^+(\tilde{X}^1\Sigma^+,v)\cdot\text{NO}$ (eV)	NO^+ ^a (eV)	NO ^b (eV)
0-1	0.261±0.008	0.290	0.233
1-2	0.256±0.020	0.287	0.229

^aReferences 5 and 23.

^bReference 24.

indicates that the Franck-Condon factors for the photoionization from the neutral dimers to the dimeric ions are unfavorable at the thresholds, and the structures for the neutral dimers are possibly quite different from those of the dimeric ions. The relatively sharp onsets observed for $(\text{NO})_2^+$ can be considered evidence that the geometry of $(\text{NO})_2^+$ is similar to that of $(\text{NO})_2$. Infrared measurements²⁵ reveal a nearly cis rectangular configuration for $(\text{NO})_2$ in the gas phase. The high binding energy for the nitric oxide dimer is attributed to the overlap of the highest occupied molecular orbital (π^*) of each NO.²⁶ Although the geometry for $\text{NO}^+\cdot\text{NO}$ is not known, it is reasonable to believe that a certain amount of overlap between the π^* orbitals of NO^+ and NO also exists in $\text{NO}^+\cdot\text{NO}$. This interaction would allow NO^+ to share the anti-bonding electron of NO. Based on this picture, one would expect the bond strength of $\text{NO}^+(\tilde{X}^1\Sigma^+)$ in $(\text{NO})_2^+$ to be between those of $\text{NO}^+(\tilde{X}^1\Sigma^+)$ and NO. This expectation seems to be consistent with the vibrational spacings measured for $\text{NO}^+(\tilde{X}^1\Sigma^+,v)\cdot\text{NO}$ in this study.

As a result of the increase in the reduced mass, the vibrational frequency of NO^+ is also expected to be lower in $\text{NO}^+\cdot\text{NO}$. However, since the binding between NO^+ and NO is weak, this effect should be quite small. In the case of $(\text{NO})_2$ which has a C_{2v} symmetry, the A_1 symmetric and the B_1 asymmetric stretching modes are found to be 0.232 eV (1870 cm^{-1}) and 0.222 eV (1788 cm^{-1}), respectively,^{27,28} as compared to a value of 0.233 eV (1876 cm^{-1}) for the vibrational

frequency for $\text{NO}(\tilde{X}^2\Pi)$. A precise assignment of the vibrational frequency resolved in this experiment will require more detailed experimental and theoretical studies in the future.

Anti-bonding electrons also seem to play an important role in the bonding of dimeric ions. From the measured bond dissociation energies for $\text{CO}^+\cdot\text{CO}$ (0.97 eV), $\text{N}_2^+\cdot\text{N}_2$ (0.90 eV), $\text{NO}^+\cdot\text{NO}$ (0.598 eV), and $\text{O}_2^+\cdot\text{O}_2$ (0.42 eV),^{10,29-31} one can see the dramatic decrease in bond energy as the number of anti-bonding electrons increases.

The PIE curve for $(\text{NO})_3^+$ in the range 1415-1470 Å is shown in Fig. 4(a). The measured IE for $(\text{NO})_3$ is 8.483 ± 0.017 eV. The IEs for $(\text{NO})_{n=4-6}$ have also been measured. These values, together with the IEs for $(\text{CO})_3$ and $(\text{N}_2)_3$, are listed in Table III. By assuming the binding energy of $(\text{NO})_n$, $n=2-5$, with NO to be the same as that of $(\text{NO})_2$, the solvation energies for NO^+ by two, three, four, and five nitric oxides can be calculated via the cycles shown in Fig.

A plot of the measured IEs for $(\text{NO})_n$, $n=1-6$, as a function of $1/n$ is shown in Fig. 6. In analogy to the previous analysis for the carbon disulfide cluster system, we find that except for a small deviation of the IE for $(\text{NO})_2$, the correlation of the IEs with cluster size is consistent with the prediction of the independent-systems model.^{32,33} If the IEs for $(\text{NO})_n$, $n>6$ continue to decrease linearly as a function of $1/n$, a value of ca. 8.1 eV is predicted for the bulk IE for nitric oxide.

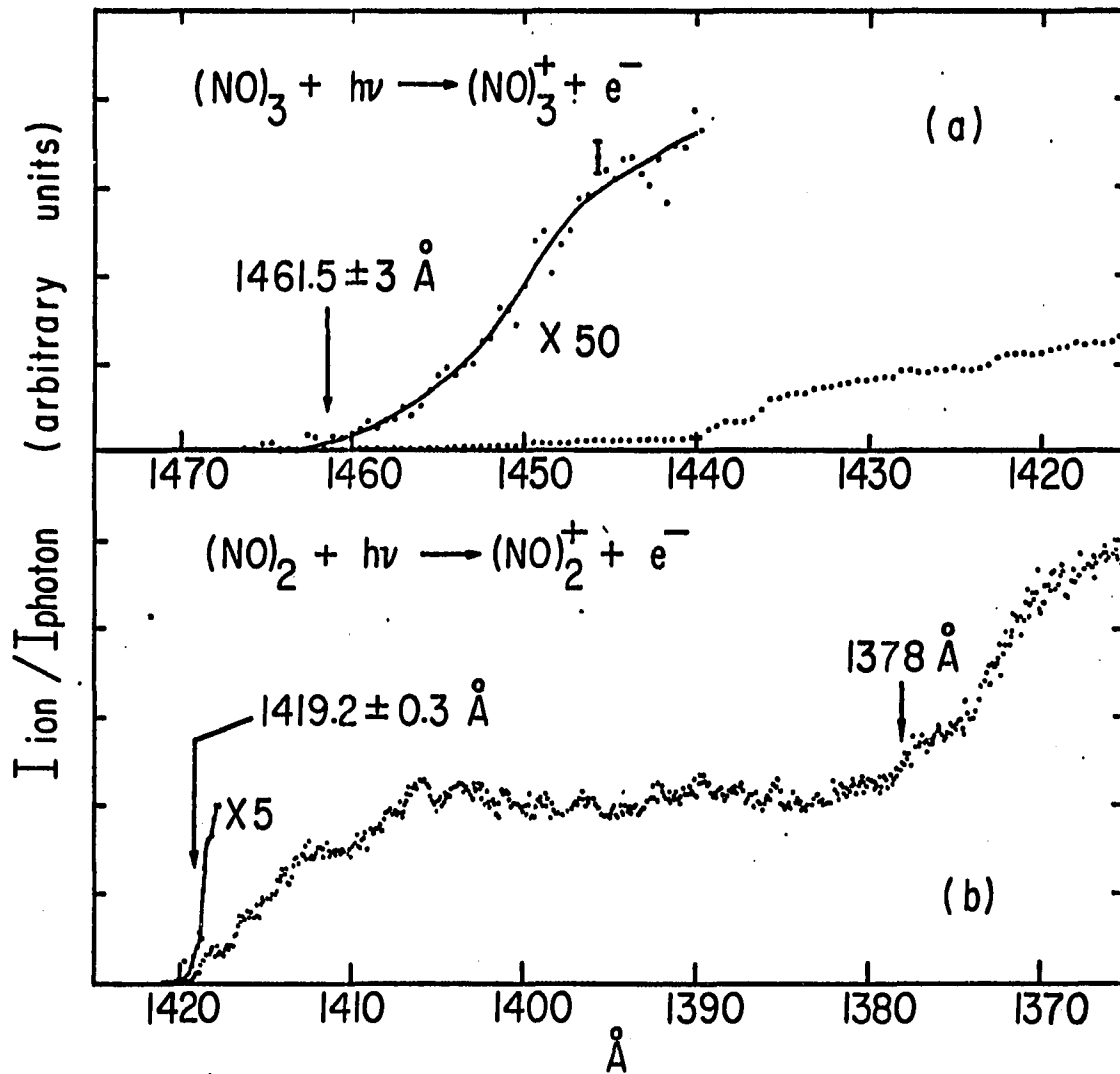


Figure 4. PIE curves for (a) $(\text{NO})_3^+$ in the range 1415-1470 Å and (b) $(\text{NO})_2^+$ in the range 1365-1425 Å obtained using a wavelength resolution of 0.28 Å (FWHM)

Table III. The ionization energies (IE) for $(\text{CO})_{2-3}$, $(\text{N}_2)_{2-3}$ and $(\text{NO})_{2-6}$

Ion	IE (eV)
$(\text{CO})_2^+$	13.05 ± 0.04
$(\text{CO})_3^+$	12.91 ± 0.04
$(\text{N}_2)_2^+$	14.69 ± 0.05
$(\text{N}_2)_3^+$	14.64 ± 0.05
$\text{NO}^+(\tilde{X}^1\Sigma^+, v=0) \cdot \text{NO}$	8.736 ± 0.002
$\text{NO}+(\tilde{X}^1\Sigma^+, v=1) \cdot \text{NO}$	8.997 ± 0.007
$\text{NO}+(\tilde{X}^1\Sigma^+, v=2) \cdot \text{NO}$	9.253 ± 0.013
$(\text{NO})_3^+$	8.486 ± 0.017
$(\text{NO})_4^+$	8.39 ± 0.03
$(\text{NO})_5^+$	8.32 ± 0.03
$(\text{NO})_6^+$	8.28 ± 0.03

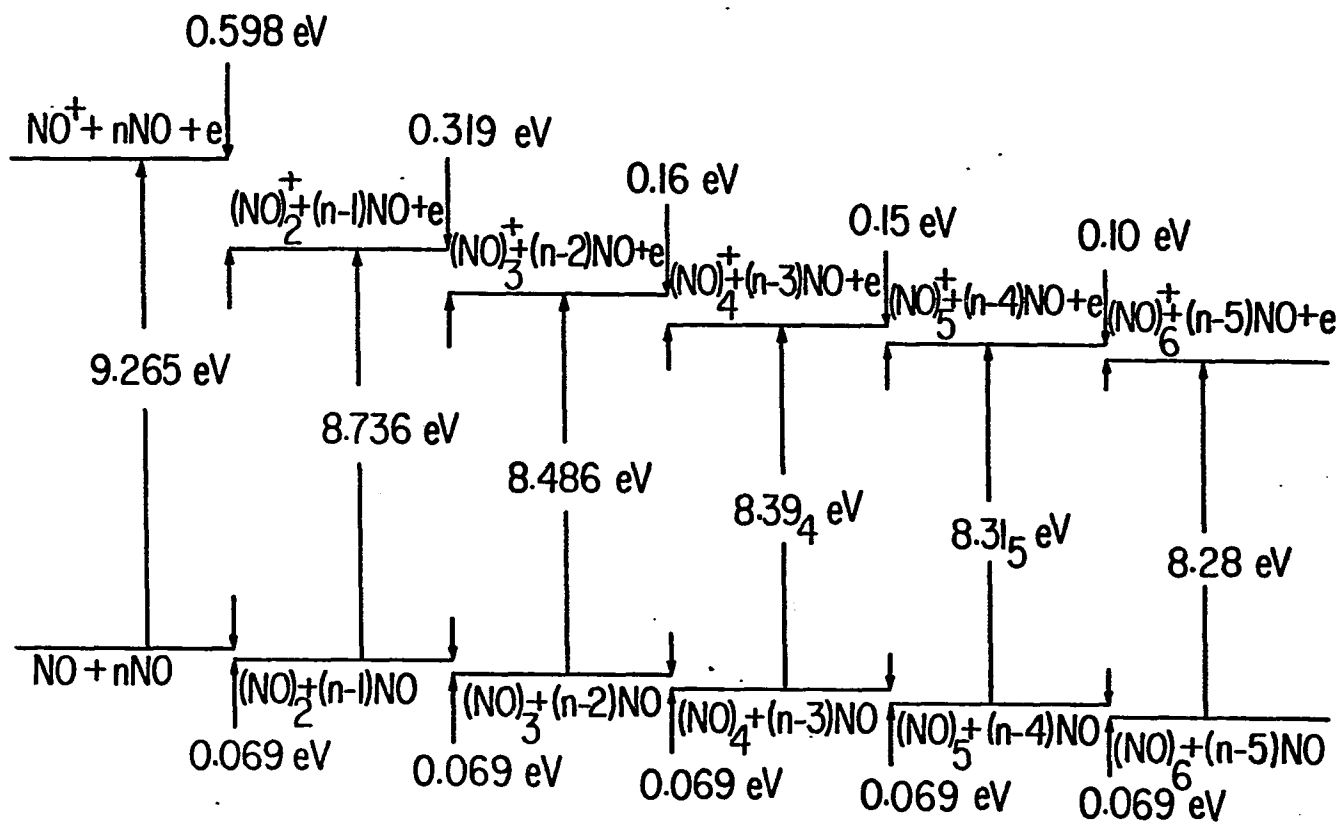


Figure 5. Energetics of $(NO)_n^+$, $n=1-6$, system

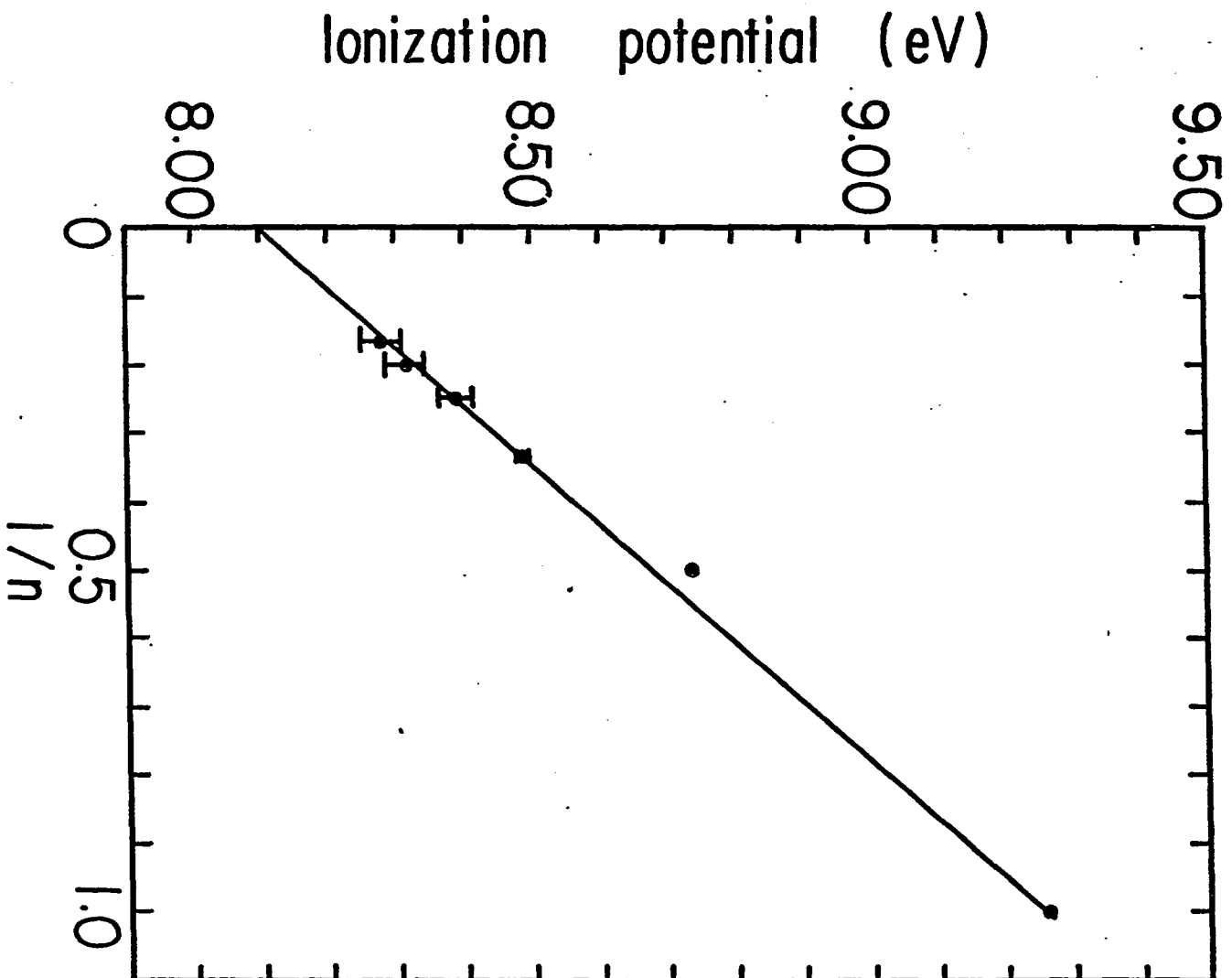


Figure 6. Plot of the IE of $(\text{NO})_n$ vs $1/n$

REFERENCES

1. J. J. Solomon, M. Meot-Ner, and F. H. Field, J. Amer. Chem. Soc. 96, 3727 (1974).
2. M. Meot-Ner and F. H. Field, J. Chem. Phys. 61, 3742 (1974).
3. See Y. Ono, S. H. Linn, H. F. Prest, M. E. Gress, and C. Y. Ng, J. Chem. Phys. 73, 2523 (1980) and references therein.
4. C. Y. Ng, P. W. Tiedemann, B. H. Mahan, and Y. T. Lee, J. Chem. Phys. 66, 3985 (1977).
5. Y. Ono, S. H. Linn, H. F. Prest, C. Y. Ng, and E. Meisher, J. Chem. Phys. 73, 4855 (1980).
6. K. E. Schubert and R. D. Hudson, "A Photoelectric Atlas of the Intense Lines of the Hydrogen Molecular Emission Spectrum from 1025 to 1650 Å at a Resolution of 0.10 Å", Report Number ATN-64 (9233)-2, Aerospace Corp, Los Angeles, 1963.
7. G. R. Cook, P. H. Metzger and M. Ogawa, Can. J. Phys. 43, 1706 (1965), and G. R. Cook and P. H. Metzger, J. Chem. Phys. 41, 321 (1964).
8. For higher resolution PIE curves for CO^+ and N_2^+ , see J. Berkowitz, "Photoabsorption, Photoionization, and Photoelectron Spectroscopy" (Academic Press, New York, 1979), p. 218 and 251.
9. Another plausible explanation is that the $\text{CO}^+\cdot\text{CO}$ (or $\text{N}_2^+\cdot\text{N}_2$) dimeric ions formed by the autoionization process in this wavelength region are energetically unstable. If these ions dissociate in less than

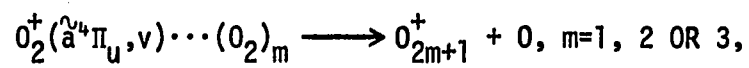
10^{-6} sec, which is approximately the flight time from the ionization region to the entrance of the quadrupole mass spectrometer, they will not be detected.

10. S. H. Linn, Y. Ono and C. Y. Ng, J. Chem. Phys. 74, 1125 (1981).
11. S. H. Linn, Y. Ono and C. Y. Ng, Iowa State University, Ames, IA.
12. This conclusion is supported by the HeI photoelectron spectra of CO, N₂, NO, and O₂. See D. W. Turner, C. Baker, A. D. Baker and C. R. Brundle, "Molecular Photoelectron Spectroscopy" (Wiley, New York, 1970).
13. In a photoionization study of (H₂)₂, Anderson et al. have been able to estimate the vibrational predissociation lifetime of vibrationally excited hydrogen molecule dimers using the known autoionization lifetime of H₂^{*}(n,v). See S. L. Anderson, T. Hirooka, P. W. Tiedemann, B. H. Mahan, and Y. T. Lee, J. Chem. Phys. 73, 4779 (1980).
14. Y. Ono, E. A. Osuch, and C. Y. Ng, J. Chem. Phys. 74, 1645 (1981).
15. P. H. Krupenie, Natl. Stand. Ref. Data Ser., Natl. Bur. Stand. 5 (1966).
16. R. E. Worley, Phys. Rev. 64, 207 (1943).
17. M. Ogawa and Y. Tanaka, Can. J. Phys. 40, 1593 (1962).
18. J. O. Hirschfelder, C. F. Curtiss and R. B. Bird, "Molecular Theory of Gases and Liquids" (Wiley, New York, 1964), p. 1111.
19. J. D. Payzant and P. Kebarle, J. Chem. Phys. 53, 4723 (1970).

20. S. L. Chong and J. L. Franklin, J. Chem. Phys. 54, 1487 (1971).
21. E. Miescher, Can. J. Phys. 54, 2074 (1976).
22. J. Billingsley and A. B. Callear, Trans. Faraday Soc. 67, 589 (1971).
23. F. Alberti and A. E. Douglas, Can. J. Phys. 53, 1179 (1975).
24. R. H. Gillette and E. H. Eyster, Physic. Rev. 56, 1113 (1939).
25. C. E. Dinerman and G. E. Ewing, J. Chem. Phys. 53, 626 (1970).
26. B. L. Blaney and G. E. Ewing, "Annual Review of Physical Chemistry", edited by B. S. Rabinovitch (Annual Reviews, Palo Alto, 1976), Vol. 27.
27. C. E. Dinerman and G. E. Ewing, J. Chem. Phys. 53, 626 (1970).
28. S. Skaarup, P. N. Skancke, and J. E. Boggs, J. Am. Chem. Soc. 98, 6106 (1976).
29. A value of 0.26 ± 0.01 eV was reported in Ref. 13.
30. D. C. Conway and G. S. Janik, J. Chem. Phys. 53, 1859 (1970).
31. D. A. Durden, P. Kekarke, and A. Good, J. Chem. Phys. 50, 805 (1969).
32. W. T. Simpson, "Theories of Electrons in Molecules" (Prentice-Hall, Englewood Cliffs, N.J., 1962), Chap. 4.
33. A. Streitwieser, Jr., "Molecular Orbital Theory for Organic Chemists" (Wiley, New York, 1961), Chap. 2.

SECTION V.

A STUDY OF THE ION-MOLECULE HALF REACTIONS



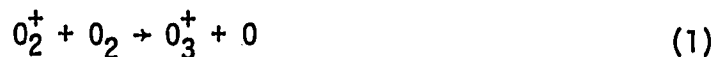
USING THE MOLECULAR BEAM PHOTOIONIZATION METHOD

ABSTRACT

The photoionization efficiency (PIE) curve for $(O_2)_2^+$ has been obtained in the region 650-1080 Å using the molecular beam photoionization method. The ionization energy (IE) for $(O_2)_2$ is determined to be 11.66 ± 0.03 eV. From the measured IE for $(O_2)_2^+$, the known IE for O_2 and the estimated dissociation energy (0.01 eV) of $(O_2)_2$, the binding energy for $(O_2)_2^+$ is deduced to be 0.42 ± 0.03 eV. Comparisons of the PIE spectra for O_2^+ and $(O_2)_m^+$, where $m=2, 3$, and 4 indicate that the excited dimer complexes $O_2^*(n,v) \cdot (O_2)_m$ ($m=1, 2$, and 3) formed in this wavelength region are almost completely dissociative, and the cluster ions are predominantly formed by the direct photoionization processes $(O_2)_{m=2, 3 \text{ or } 4} + h\nu \rightarrow (O_2)_{m=2, 3 \text{ or } 4}^+ + e$. The PIE curves for O_3^+ , O_5^+ , and O_7^+ are measured in the region 650-780 Å. The appearance energy 16.66 ± 0.03 eV (744 ± 1.5 Å) for O_3^+ is found to be consistent with a zero activation energy for the ion-molecule reaction $O_2^+(\tilde{X}^2\Pi_g) + O_2 \longrightarrow O_3^+ + 0$. The appearance energy for O_5^+ is determined to be 16.41 ± 0.06 eV (755.5 ± 3 Å). This value has allowed the determination of a binding energy of 0.26 eV for $O_3^+ \cdot O_2$. The nearly structureless PIE spectra observed for O_3^+ , O_5^+ , and O_7^+ also suggest that these ions originate mainly from $(O_2)_2^+$, $(O_2)_3^+$, and $(O_2)_4^+$ which are formed by direct ionization processes. Using the relative Franck-Condon factors for the $O_2 \tilde{a}^4\Pi_u \leftarrow \tilde{X}^3\Sigma_g^-$ transitions, the relative reaction probabilities for the ion-molecule half reactions, $O_2^+(\tilde{a}^2\Pi_u, v) \cdot (O_2)_m \rightarrow O_{2m+1}^+ + 0$ ($m=1, 2$, and 3) — (1) as a function of the vibrational quantum number v have been determined. The relative intensities of O_3^+ , O_5^+ , O_7^+ , and $(O_2)_{m=2-4}^+$ observed in this experiment support the conclusion that the reaction probabilities of (1) with $m=2$ and 3 are substantially larger than those with $m=1$.

INTRODUCTION

The ion-molecule reaction



has been studied previously¹⁻⁶ using electron impact ionization to produce the reactant O_2^+ . In a gas cell photoionization experiment, Ajello, Pang, and Monahan⁷ have been able to observe the threshold for the reaction corresponding to the $O_2^+(\tilde{a}^4\Pi_u, v=5)$ convergence limit. A more recent study, which employed photoionization techniques to produce the O_2 reactant using a higher wavelength resolution, has been reported by Dehmer and Chupka.⁸ They found that the reaction proceeds primarily through the $O_2^+(\tilde{a}^4\Pi_u, v=5-10)$ vibrational states. With corrections for the contributions to the formation of O_3^+ from O_2^+ produced by autoionization processes, they were able to determine the reaction cross sections for Reaction (1) with O_2^+ in the $\tilde{a}^4\Pi_u, v=5-10$ states. Their study shows that vibrational energy was more effective than translational energy in forming the product and that the cross section for Reaction (1) increases significantly with vibrational energy from the $v=5-9$ levels.

The present report presents the results of a photoionization study of oxygen clusters using the molecular beam method. Since the binding between the two moieties in $(O_2)_2$ is very weak, to a good approximation, photoionization of the dimer can be viewed as ionizing only one of the moieties making up the dimer. By varying the photon energy, excited reaction complexes $O_2^+ \cdot O_2$, with O_2^+ in specific states, can be formed. Direct

measurements of the O_3^+ formation from these complexes as a function of internal excitation is expected to provide valuable information about the reaction dynamics of Reaction (1).

Owing to the nature of this experiment, the relative reaction probabilities for Reaction (1) determined in this study are only applied to reactions that proceed from complex formations. Although the excited complexes prepared from dimers are probably more specific than those formed in real collisional processes, it is still interesting to compare the reaction probabilities for Reaction (1) obtained here with the relative reaction cross sections reported in Ref. 8. This comparison will yield information about the relative importance of the direct and the complex reaction mechanisms for the O_3^+ formation with O_2^+ in specific excited states.

Following the argument given above, photoionization of higher oxygen clusters also offers a direct route for preparing collision complexes of the form $O_2^+(\tilde{a}^4\Pi_u, v) \cdot (O_2)_{m>1}$. A systematic measurement of fragments from these complexes will provide insight into the reaction mechanism in condensed phases.

From the ionization energies (IE) of oxygen clusters and the estimated bonding energies for the neutral clusters, the bond energies for $(O_2)_m^+ \cdot O_2$ can be deduced. However, since these values have been determined by Conway and Janik,⁹ and the photoionization study of the oxygen clusters, $(O_2)_{m=2-5}$, near the thresholds has been carried out recently by Anderson *et al.*,¹⁰ measurements of the PIE curves for these cluster ions [except that

for $(O_2)_2^+$ in this region have not been included in the present study. This report is concerned mainly with the study of the fragmentation yielding O_{2m+1}^+ , $m=1, 2, \text{ and } 3$, from these even-numbered oxygen atom cluster ions.

EXPERIMENTAL

This experiment was performed using a new molecular beam photoionization apparatus which has been already described in detail.^{11,12} Using a differential pumping arrangement different from that used previously,¹³ we have been able to improve the molecular beam intensity in the ionization region, and yet maintain a low enough background pressure to prevent interference due to secondary scattering processes. Briefly, the apparatus consists of a quadrupole mass spectrometer, a supersonic molecular beam production system, a windowless 3 m vacuum ultraviolet monochromator, and a capillary discharge light source. Depending on the wavelength region, the light sources used in this study were the helium Hopfield continuum and the hydrogen many-lined pseudocontinuum. The light intensity was monitored with a sodium salicylate coated photomultiplier. The grating employed in this study was a Bausch and Lomb 1200 λ/mm Os coated aluminum grating blazed at 1360 \AA .

The oxygen used in this experiment was obtained from Matheson (99.99% minimum purity). The van der Waals dimers and clusters of oxygen are produced by supersonic expansion through a 0.05 mm diameter stainless nozzle at a stagnation pressure of ~ 450 torr. The nozzle temperature was maintained at $\sim 110\text{K}$. During an experiment, the stability of the nozzle temperature was better than $\pm 3\text{K}$ as monitored with a thermocouple.

The PIE curves were obtained in this experiment using 500 μm entrance and exit slits and the wavelength resolution achieved was 1.4 \AA (FWHM).

Data are plotted at intervals of 0.5 \AA . Each curve was based on at least two scans and prominent structures in the curves were found to be reproducible. Wavelength calibrations were achieved by using the appropriate known atomic resonance lines.

Figure 1 shows the PIE curves for O_2^+ and $(O_2)_2^+$ in the region 650-1080 \AA . The PIE curves for O^+ (630-730 \AA), O_3^+ (665-750 \AA), O_5^+ (650-780 \AA), $(O_2)_3^+$ (650-820 \AA), O_7^+ (650-780 \AA), and $(O_2)_4^+$ (650-810 \AA) are depicted in Figs. 2(b), 2(a), 3(b), 3(a), 4(b), and 4(a), respectively.

RESULTS AND DISCUSSION

Recently, Anderson *et al.*¹⁰ have reported a photoionization study of the oxygen clusters, $(O_2)_{n=2-5}$, near the thresholds. From the IE for $(O_2)_2$ determined in their experiment, they concluded that $(O_2)_2^+$ is bound by 0.26 ± 0.02 eV. Since this value is substantially lower than the bond dissociation energy, 0.457 ± 0.005 eV, determined from equilibrium constant data,⁹ we decided to reexamine this value here. Due to the improved sensitivity of the apparatus used in this study, the IE of $(O_2)_2$ was found to be 11.66 ± 0.03 eV (1063 ± 3 Å) as shown in Fig. 1. Using this value, the known IE¹⁴⁻¹⁸ (12.07 eV) for O_2 , and the estimated binding energy¹⁹ (0.01 eV) for $(O_2)_2$, the dissociation energy for $O_2^+ \cdot O_2$ is deduced to be 0.42 ± 0.03 eV. Although this value is still slightly lower than the value reported in Ref. 9, taking into account the uncertainty of the binding energy for $(O_2)_2$, the previous value is probably within the limits of error of the binding energy deduced for $(O_2)_2^+$ in the present photoionization study.

The general shape of the PIE spectrum for the O_2^+ ion is in good agreement with the photoabsorption curve reported by Huffman *et al.*¹⁷ and the PIE curves of Cook and Metzger,²⁰ Dibeler and Walker,¹⁶ Matsunaga and Watanabe,²¹ and Dehmer and Chupka.¹⁵ The O_2^+ spectrum is dominated by intense autoionization features. Most of these structures have been identified as vibrational progressions or Rydberg series converging to electronically excited states of the oxygen molecular ions.¹⁵ However, in strong contrast to the O_2^+ spectrum, the PIE curve for $(O_2)_2^+$ is structureless. A plausible explanation

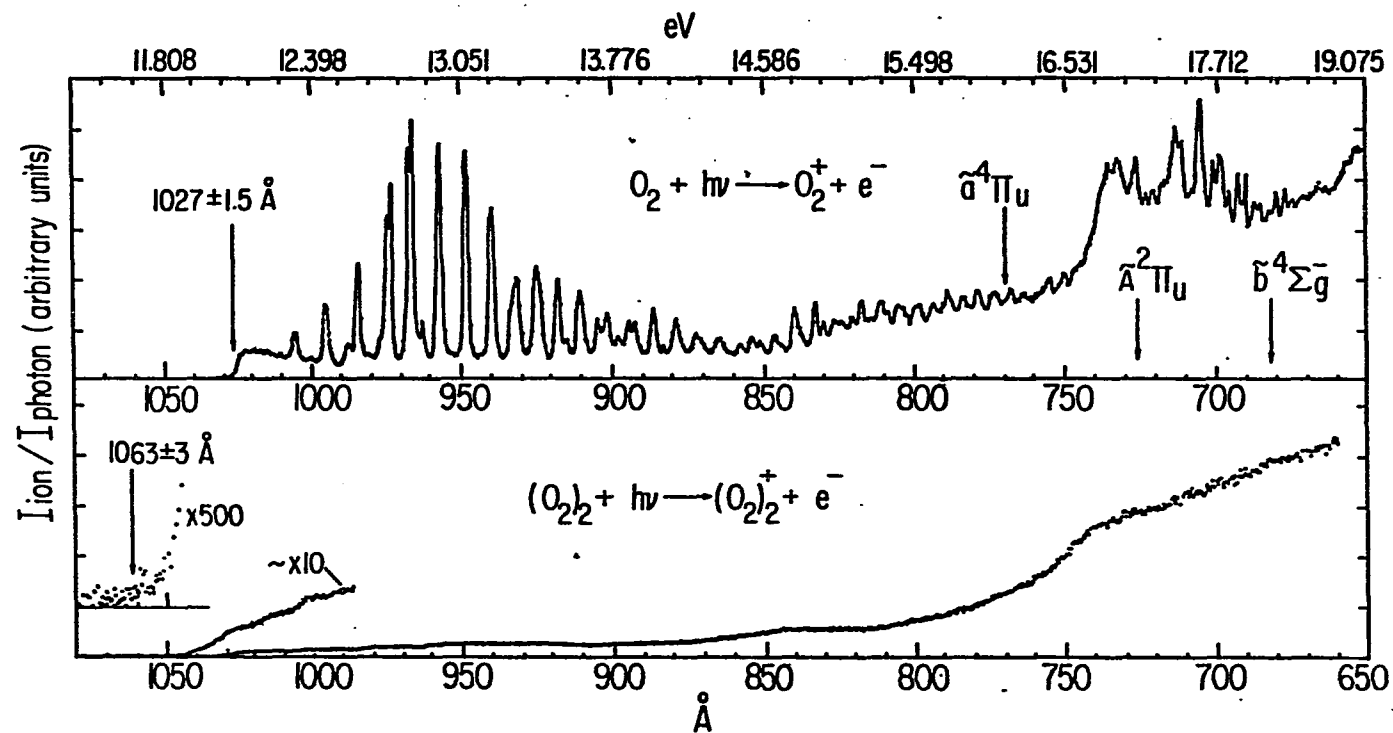


Figure 1. PIE curves for O_2^+ and $(O_2)_2^+$ in the region from 650-1080 \AA

for this observation is that the excited complexes, $O_2^*(n,v) \cdot O_2$, initially formed by photoexcitation in this region are strongly dissociative and the $(O_2)_2^+$ ions produced by the associative ionization processes are negligible. In other words, the $(O_2)_2^+$ ions observed in this experiment are formed predominately by the direct ionization processes,

$$O_2 \cdot O_2 + h\nu \rightarrow O_2^+ \cdot O_2.$$

When the photoionization efficiencies for the formation of $(O_2)_2^+$, $(O_2)_3^+$, and $(O_2)_4^+$ are normalized at a particular wavelength the PIE curves for $(O_2)_2^+$, $(O_2)_3^+$, and $(O_2)_4^+$ are nearly superimposable. Portions of the $(O_2)_3^+$ and $(O_2)_4^+$ data are plotted in Figs. 3(a) and 4(a), respectively. With the present nozzle conditions, the relative intensities measured at 650 Å for $(O_2)_2^+$, $(O_2)_3^+$, and $(O_2)_4^+$ are approximately 1, 0.50, and 0.25, respectively. The nearly identical curves observed for $(O_2)_2^+$, $(O_2)_3^+$, and $(O_2)_4^+$ indicate that the contamination of $(O_2)_2^+$ from fragmentations of higher clusters is not significant. The PIE curves for O_3^+ [Fig. 2(a)], O_5^+ [Fig. 3(b)], and O_7^+ [Fig. 4(b)] are also found to be very smooth. The sharp autoionization features resolved in the O_2^+ curve are hardly observable in these data. This leads us to believe that the O_3^+ , O_5^+ , and O_7^+ ions observed are mainly fragments of $(O_2)_2^+$, $(O_2)_3^+$, and $(O_2)_4^+$, respectively.

The appearance energy (AE) for O_3^+ is measured to be 16.66 ± 0.03 eV (744 ± 1.5 Å). Using this value, the AE (18.73 eV) of the dissociative ionization process, $O_2 + h\nu \rightarrow O^+ + O + e$, and the estimated binding energy (0.01 eV) of $(O_2)_2$, the threshold energy for the ion-molecule

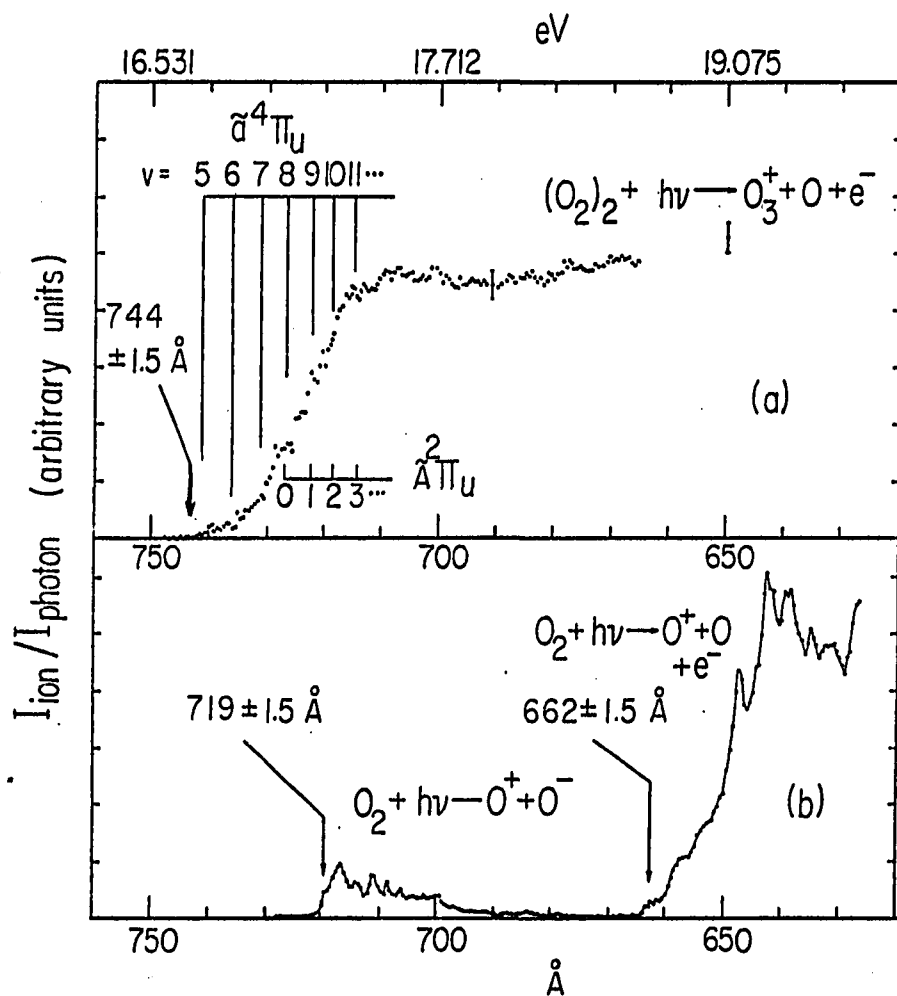


Figure 2. PIE curves for (a) O_3^+ and (b) O^+ in the region from 630-750 \AA

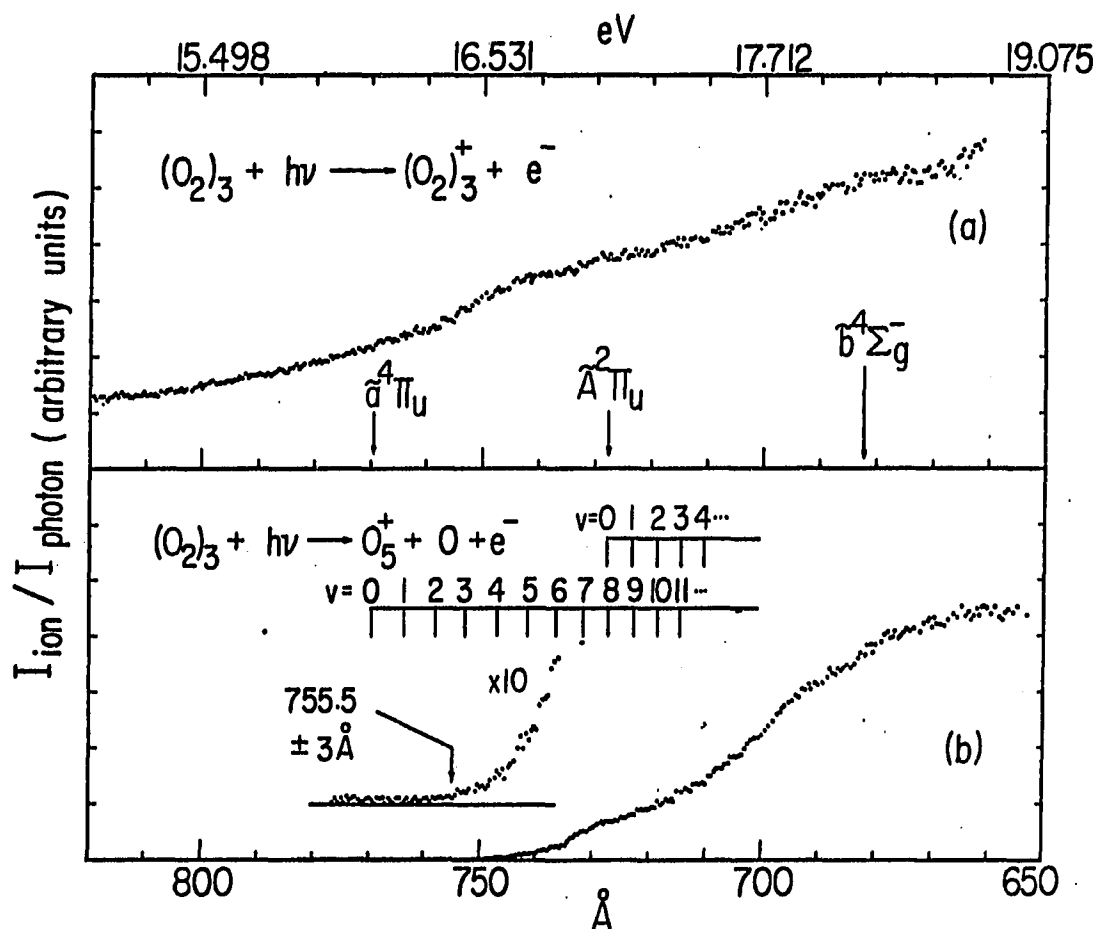


Figure 3. PIE curves for (a) $(\text{O}_2)_3^+$ and (b) O_5^+ in the region from 650-820 Å

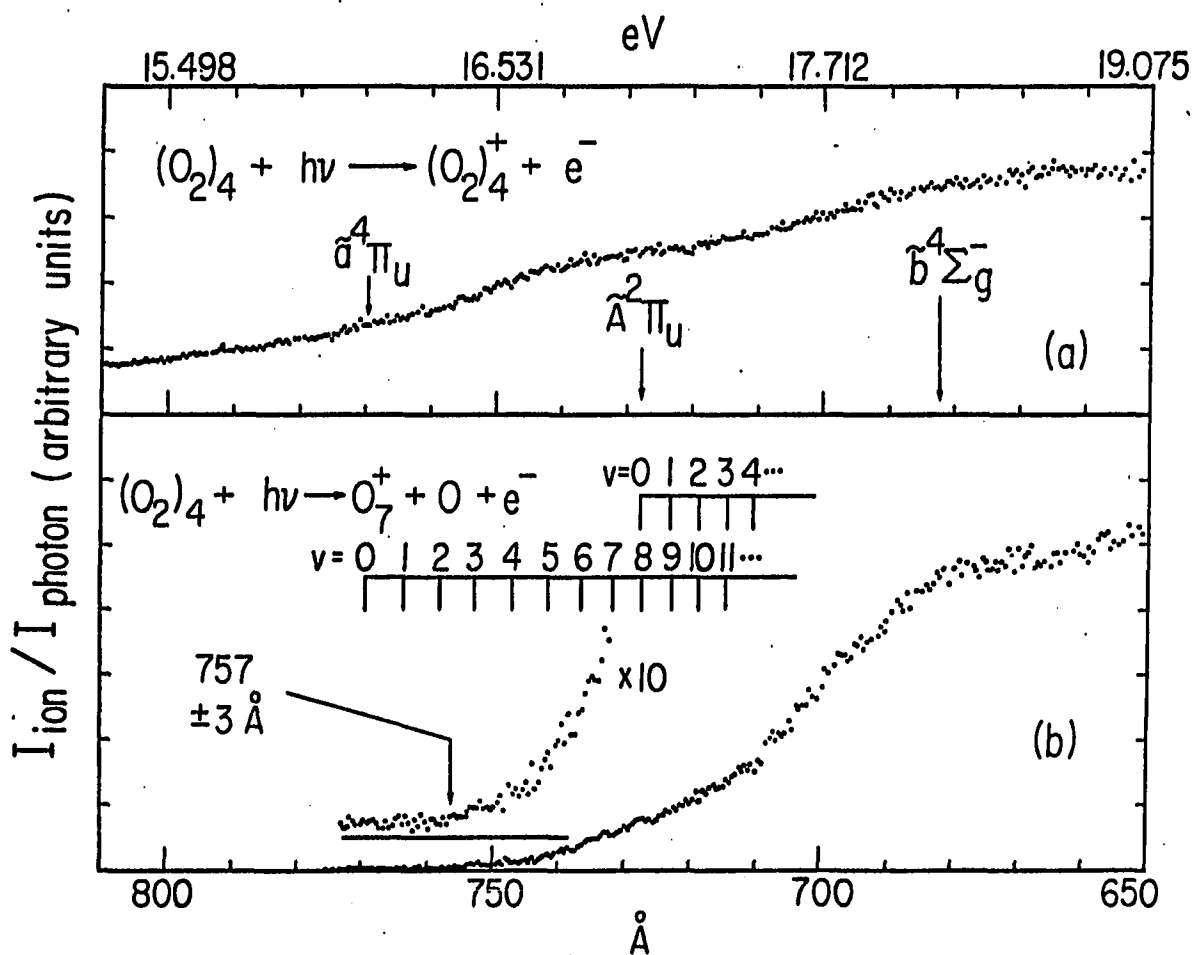


Figure 4. PIE curves for (a) $(\text{O}_2)_4^+$ and (b) O_7^+ in the region from 650-810 \AA

reaction (1) is deduced to be 4.58 ± 0.03 eV. Within the uncertainties of this experiment, this value is found to be equal to the thermochemical threshold for Reaction (1) with O_2^+ in the $\tilde{X}^2\Pi_g$ state. This measurement is consistent with the values reported in previous photoionization studies.^{7,8} The PIE for O_3^+ increases quite sharply from the threshold and then remains almost constant in the range ~ 715 - 680 Å. The curve shows a slow increase at ~ 680 Å, which is about the onset of the $\tilde{b}^4\Sigma_g^-$ state.

In order to estimate the contributions to the O_3^+ spectrum from fragmentations of higher polymers during the photoionization, a spectrum for O_3^+ was also obtained at a nozzle stagnation pressure of ~ 140 Torr, at which the concentrations of $(O_2)_3^+$ and $(O_2)_4^+$ are much less than that of $(O_2)_2^+$. The PIE curve for O_3^+ measured under these conditions is in good agreement with the spectrum shown in Fig. 2(a). This observation supports the conclusion that contaminations of the O_3^+ spectrum due to dissociations of higher clusters is minimal in this wavelength region.

The O^+ ions can be produced by the ion-pair process^{15,16,22}



as well as by the dissociative ionization process mentioned above [Fig. 2(b)]. Since the production of O^+ by Reaction (2) lies in the wavelength region of interest, one would expect contributions to the O_3^+ formation from the process

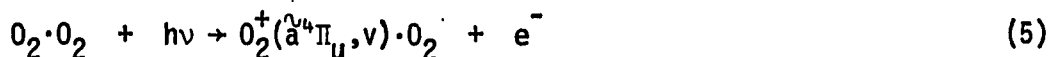


The AE for Reaction (3) is lower than that for the process:



by 1.462 eV,¹⁵ which is the electron affinity of the oxygen atom. The fact that no O_3^+ ions were observed below the AE for Reaction (4) is considered to be evidence that the O_3^+ ions formed by Reaction (3) are negligible.

The AE of O_3^+ formation is approximately the energy for simultaneous ionization and excitation of O_2 to the $v=5$ level of the $\tilde{a}^4\Pi_u$ state of O_2^+ .²⁴ Since the $(O_2)_2$ is only weakly bound by van der Waals forces, it is likely that the actual absorption of a photon by an oxygen dimer involves only one of the O_2 molecules in $(O_2)_2$. As a result of the perturbation of the absorber by its partner, the excitation photon energy for the process



is expected to be slightly different from that for the excitation process



However, due to the weak binding energies, ~ 0.01 eV and ~ 0.4 eV, for $(O_2)_2$ and $(O_2)_2^+$, respectively, the actual shift in energy for the above process in the dimer from that of the monomer should be quite small. The positions corresponding to the excitation of O_2 to the $\tilde{a}^4\Pi_u, v=6,7,8,9,10$, and 11 states of O_2^+ are shown in Fig. 2(a).

Assuming the validity of the arguments that the O_3^+ ions are fragments of the $O_2^+(\tilde{a}^4\Pi_u, v) \cdot O_2$ complexes which are formed by the direct

ionization process (5), the relative reaction probabilities, σ_v , for the half reaction



can be obtained by normalizing the average increments in the PIE for O_3^+ of various vibrational states with the relative Franck-Condon factors for Reaction (6).²³ The onset of the $\tilde{A}^2\Pi_u, v=0$, state of O_2^+ almost coincides with the $\tilde{a}^4\Pi_u, v=8$ state. Therefore, at energies greater than the $O_2^+(\tilde{A}^2\Pi_u, v=0)$ converging limit, the reaction may also proceed via this state. However, since the Franck-Condon factors for transitions from the ground state of O_2 to the first few vibrational levels of the $\tilde{A}^2\Pi_u$ state are very small, the contribution from this state is neglected. The values for σ_v obtained by this analysis are listed in Table I. Since errors of the O_3^+ data are $\sim\pm 10\%$, the uncertainties of these values are estimated to be $\sim\pm 20\%$. These values are normalized to 100 at $v=10$ so that they can be compared with the relative cross sections reported by Dehmer and Chupka.¹⁵ The general trend of σ_v is found to be similar to that observed for the relative cross sections, namely, it increases sharply as a function of vibrational energy and peaks at $v=10$. Dehmer and Chupka found that the total continuum for $v=11$ is approximately equal to that of $v=10$, which gives a cross section of zero for $v=11$. This was attributed to the dissociation of energetically unstable O_3^+ into $O_2^+ + O$. The nearly constant PIE for O_3^+ beyond the threshold of $v=11$ observed in this experiment is also consistent with this interpretation.

In a real collisional experiment, products can be formed by both the direct processes as well as by processes which involve intermediate complexes. Since the configurations of the excited complexes prepared by photoionization are probably quite specific,²⁴ and the division into direct and complex mechanisms is also quite arbitrary, it is difficult to relate the values for σ_V with those due to the complex mechanisms in real collisional experiments in which angular momenta are expected to play an important role. Nevertheless, a more dramatic vibrational energy dependence for the relative reaction cross sections obtained previously as compared to the σ_V derived from this study (shown in Table I) appears to reveal a stronger vibrational energy dependence for the reaction cross sections of the direct processes.

The AE for O_5^+ is determined to be 16.41 ± 0.06 eV. Within experimental uncertainties, the AE (16.38 ± 0.06 eV) for O_7^+ is found to be equal to that of O_5^+ . By assuming the binding energy of $(O_2)_m$, $m=2-3$, with O_2 to be the same as $(O_2)_2$, the energetics for the O_{2m+1}^+ , $m=1-3$, ions can be calculated via the cycles shown in Fig. 5. Since O_5^+ can be viewed as having a structure $O_3^+ \cdot O_2$, a binding energy of 0.26 eV is deduced for $O_3^+ \cdot O_2$ from this experiment. Formation of the O_5^+ ion has also been observed in a gas cell photoionization study of the ion-molecule reaction of $O_3^+ + O_3$.²⁵ The O_5^+ formed by this reaction is more likely to have a structure of $O_2^+ \cdot O_3$.

Using the same arguments as given above, the relative reaction probabilities, σ_V , for the reactions

Table I. Relative reaction probabilities for the ion-molecule reactions, $O_2^+(\tilde{a}^4\Pi_u, v) \cdots O_2 \longrightarrow O_3^+ + O$

$O_2^+(\tilde{a}^4\Pi_u, v)^a$	FCF ^b	σ_v^c	Relative cross section ^d
$v'=5$ 742.08	0.13202	8	1.9
6 737.09	0.12152	28	11
7 732.28	0.10301	67	38.5
8 727.64	0.08192	88	66
9 723.17	0.06197	100	100
10 718.86	0.044506	92	89.5

^aReference 23.

^bFranck-Condon factor for the excitation process (6).
See Ref. 23.

^cRelative reaction probabilities for the ion-molecule half reaction (7).

^dRelative cross sections for the full ion-molecule reaction $O_2^+(\tilde{a}^4\Pi_u, v) + O_2 \longrightarrow O_3^+ + O$ (Ref. 15).

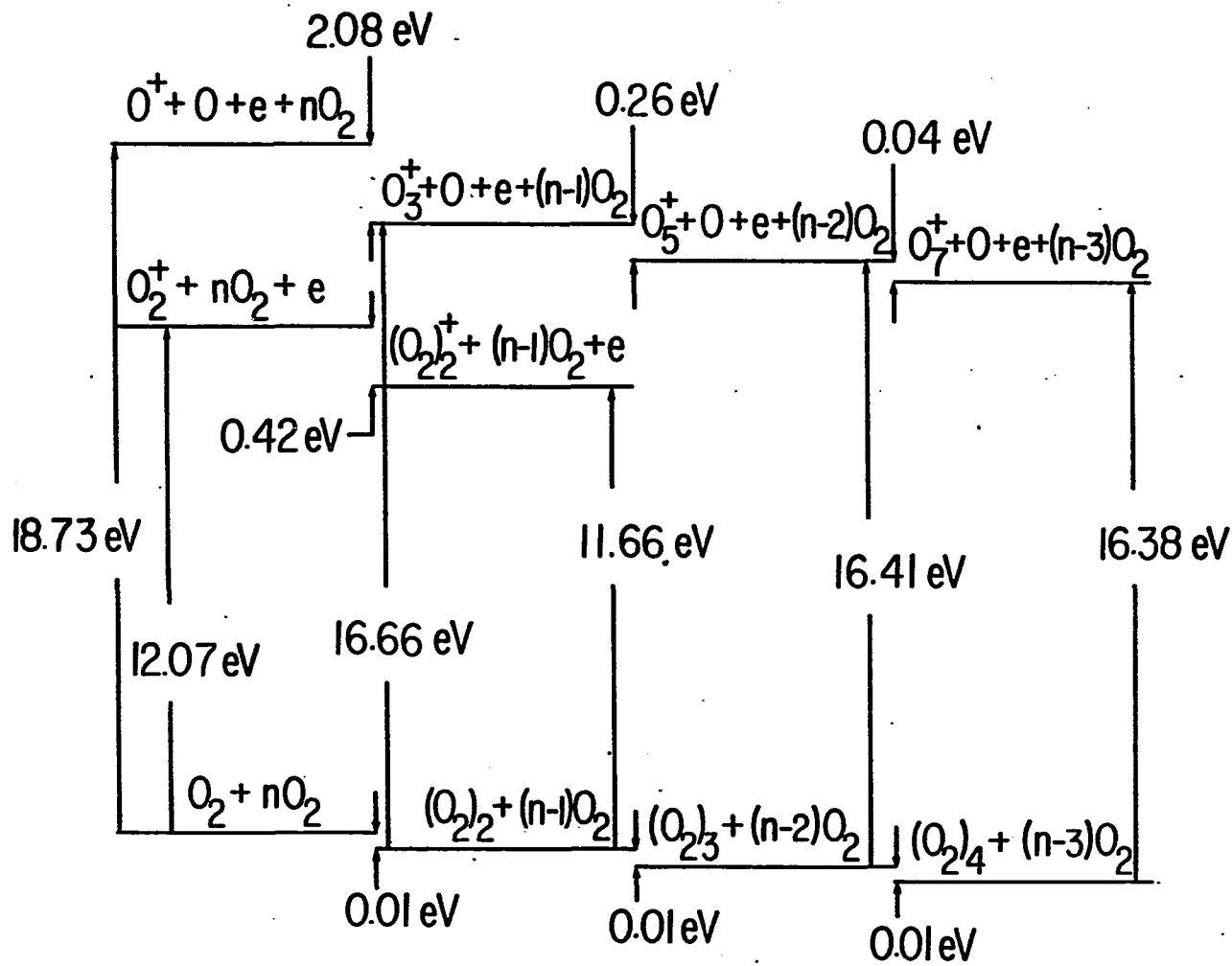
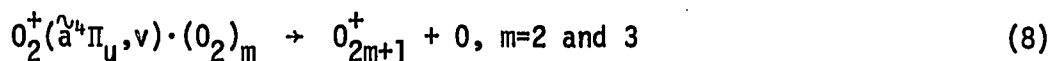


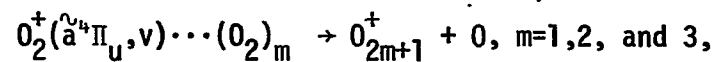
Figure 5. Energetics of the O_{2m+1}^+ , $m=1, 2,$ and 3 system






can also be derived as a function of vibrational energy. The values of σ_v obtained for Reactions (7) and (8) are compared in Fig. 6, where $\sigma_{v=3}(O_5^+)$, $\sigma_{v=3}(O_7^+)$, and $\sigma_{v=5}(O_3^+)$ are normalized to the same value. There seems to be anomalous increases in values of σ_v at $v=9$ and 10 of Reaction (8), $m=2$ and 3 . This behavior may arise from negligence of contributions from the $\tilde{A}^2\Pi_u$ state. It is found that σ_v for Reaction (7) has a stronger vibrational energy dependence than that of Reaction (8) with $m=2$. The values of σ_v for Reaction (8) with $m=3$ show only a weak dependence on vibrational energy. In view of the fact that a larger complex has more degrees of freedom to redistribute the energy after the excitation of one of the moieties in the cluster, it is reasonable to find vibrational energy to be less effective in promoting the reaction as the size of the cluster increases. The weaker dependence of σ_v on v for the higher cluster reactions (9) observed here is probably also due to fragmentations of the energetically unstable product ions formed at high excitation energies.

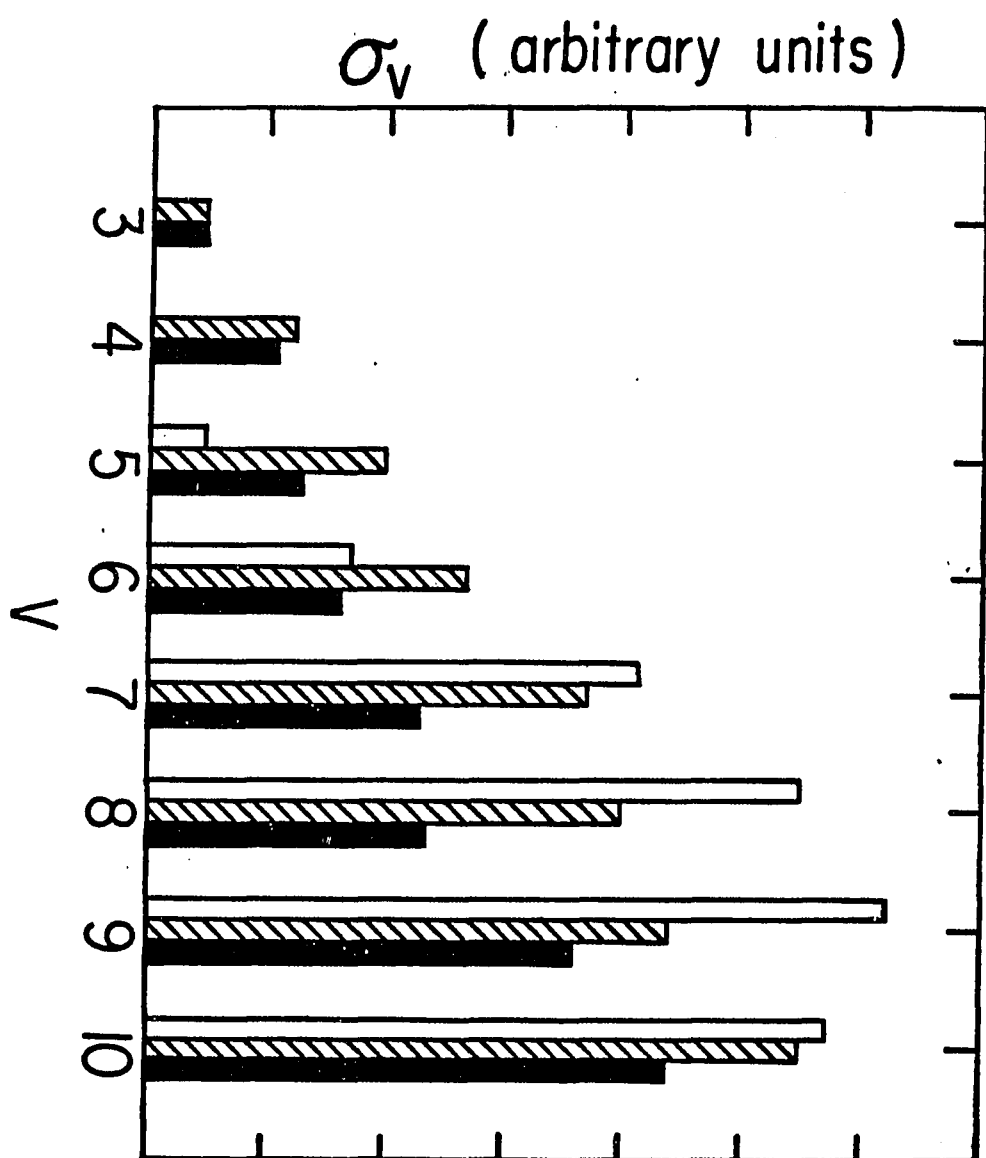
At 650 \AA , the values for $I(O_7^+)/I((O_2)_4^+)$, $I(O_5^+)/I((O_2)_3^+)$ and $I(O_3^+)/I((O_2)_2^+)$ were found to be ~ 0.15 , ~ 0.20 and ~ 0.015 ,²⁶ respectively, where $I(O_3^+)$, $I(O_5^+)$, $I(O_7^+)$, $I((O_2)_2^+)$, $I((O_2)_3^+)$, and $I((O_2)_4^+)$ represent the intensities of O_3^+ , O_5^+ , O_7^+ , $(O_2)_2^+$, $(O_2)_3^+$, and $(O_2)_4^+$, respectively. From the PIE curves for O_3^+ , O_5^+ , O_7^+ , $(O_2)_2^+$, $(O_2)_3^+$, and $(O_2)_4^+$ and the relative intensities of these species measured at 650 \AA , the relation, $I(O_7^+)/I((O_2)_4^+) \sim I(O_5^+)/I((O_2)_3^+) \sim 10I(O_3^+)/I((O_2)_2^+)$, was found to be valid

Figure 6. Relative reaction probabilities, σ_v , for the ion-molecule reactions,



as a function of the vibrational quantum number v . $\sigma_{v=3}(O_5^+)$, $\sigma_{v=3}(O_7^+)$ and $\sigma_{v=5}(O_3^+)$ are arbitrarily normalized to the same value

-  = σ_v for the formation of O_3^+ from $(O_2)_2^+$
-  = σ_v for the formation of O_5^+ from $(O_2)_3^+$
-  = σ_v for the formation of O_7^+ from $(O_2)_4^+$



at $\sim 730 \text{ \AA}$. Since the differences of $I(O_3^+)/I((O_2)_2^+)$ from $I(O_5^+)/I((O_2)_3^+)$ and $I(O_7^+)/I((O_2)_4^+)$ observed are too large to be caused by fragmentations, we conclude that the reaction probabilities for Reaction (8) are substantially higher than that of Reaction (7). The reaction probabilities for these reactions probably depend on solvation effects as well as the structures of these excited cluster ions. Stemming from the fact that the $O_2^+(\tilde{a}^4\Pi_u, v)$ molecular ions in $O_2^+(\tilde{a}^4\Pi_u, v) \cdot (O_2)_2$ and $O_2^+(\tilde{a}^4\Pi_u, v) \cdot (O_2)_3$ are in the proximity of two and three oxygen molecules, respectively, in comparison to only one oxygen molecule in $O_2^+(\tilde{a}^4\Pi_u, v) \cdot O_2$, the result observed in this study seems to be a reasonable one.

SUMMARY

The stabilities of $(O_2)_2^+$, O_3^+ , O_5^+ , and O_7^+ have been determined using the molecular beam photoionization method. By measuring the intensities of the fragments, O_3^+ , O_5^+ , and O_7^+ , which originate mainly from $O_2^+(\overset{\lambda}{a}^4\Pi_u, v) \cdot O_2$, $O_2^+(\overset{\lambda}{a}^4\Pi_u, v) \cdot (O_2)_2$ and $O_2^+(\overset{\lambda}{a}^4\Pi_u, v) \cdot (O_2)_3$, respectively, as a function of vibrational excitation, valuable insights concerning the internal energy effect on the reactions of O_2^+ with oxygen clusters have been obtained. This experiment has demonstrated that molecular beam photoionization of molecular clusters is a potentially useful method for the investigation of the solvation effect on chemical reactions in condensed phases.

REFERENCES

1. J. T. Herron and H. I. Schiff, *Can. J. Chem.* 36, 1159 (1958).
2. P. Dong and M. Cottin, *J. Chim. Phys.* 57, 557 (1960).
3. V. Cermak and Z. Herman, *J. Chim. Phys.* 57, 717 (1960).
4. R. K. Curran, *J. Chem. Phys.* 38, 2974 (1963).
5. J. J. Leventhal and L. Friedman, *J. Chem. Phys.* 46, 997 (1967).
6. V. Cermak and Z. Herman, *Collect. Czech. Chem. Commun.* 27, 1493 (1962).
7. J. M. Ajello, K. D. Pang and K. M. Monahan, *J. Chem. Phys.* 61, 3152 (1974).
8. P. M. Dehmer and W. A. Chupka, *J. Chem. Phys.* 62, 2228 (1975).
9. D. C. Conway and G. S. Janik, *J. Chem. Phys.* 53, 1859 (1970).
10. S. L. Anderson, T. Hirooka, P. W. Tiedemann, B. H. Mahan, and Y. T. Lee, *J. Chem. Phys.* 73, 4779 (1980).
11. Y. Ono, S. H. Linn, H. F. Prest, M. E. Gress, and C. Y. Ng, *J. Chem. Phys.* 73, 2523 (1980).
12. Y. Ono, S. H. Linn, H. F. Prest, C. Y. Ng, and E. Miescher, *J. Chem. Phys.* 73, 4855 (1980).
13. C. Y. Ng, B. H. Mahan and Y. T. Lee, *J. Chem. Phys.* 65, 1956 (1976).
14. J. A. R. Samson and J. L. Gardner, *Can. J. Phys.* 53, 1948 (1975).
15. P. M. Dehmer and W. A. Chupka, *J. Chem. Phys.* 62, 4525 (1975).
16. V. H. Dibeler and J. A. Walker, *J. Chem. Phys.* 57, 1007 (1967).

17. R. E. Huffman, J. C. Larrabee and Y. Tanaka, J. Chem. Phys. 40, 356 (1964).
18. J. A. R. Samson and R. B. Cairns, J. Opt. Soc. Am. 56, 769 (1966).
19. J. O. Hirschfelder, C. F. Curtiss and R. B. Bird, "Molecular Theory of Gases and Liquids" (Wiley, New York, 1964) p. 1111.
20. G. R. Cook and P. H. Metzger, J. Chem. Phys. 41, 321 (1964).
21. F. M. Matsunaga and K. Watanabe, Sci. Light (Tokyo) 16, 31 (1967).
22. H. Oertel, H. Schenk and H. Baumgärtel, Chem. Phys. 46, 251 (1980).
23. P. Krupene, J. Phys. Chem. Ref. Data 1, 423 (1972).
24. The configurations of the excited complexes, $O_2^+(\tilde{a}^4\Pi_u, v) \cdot O_2$ formed by photoionization are governed by the geometry of the neutral oxygen dimer and the nature of the ionization processes.
25. M. J. Weiss, J. Berkowitz, and E. H. Appelman, J. Chem. Phys. 66, 2049 (1977).
26. These ratios were found to change slightly as the nozzle stagnation pressure varied from ~ 200 to 450 Torr. These small changes indicate that fragmentations of small fractions of energetically unstable cluster ions indeed do take place.

GENERAL CONCLUSION

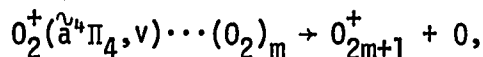
The first high resolution (0.14 Å) photoionization efficiency studies of higher temperature vapors (HgX_2 , $X = \text{Cl}, \text{Br}, \text{I}$) have been carried out using the supersonic beam method. Those studies have yielded more precise values for the IEs of the $\tilde{X}^2\Pi_{3/2g}$, $^2\Pi_{1/2g}$ and $^2D_{\pm 5/2}$ states of HgX_2^+ than the literature values. In addition, transitions corresponding to Rydberg series converging to the $^2D_{\pm 5/2}$ and $^2D_{\pm 3/2, \pm 1/2}$ states of HgX_2^+ have been identified.

The fragmentation processes of HgCl_2^+ , HgBr_2^+ and HgI_2^+ have been studied and were found to be similar. The autoionizing Rydberg series found in the PIE studies of HgX_2^+ were also present in the fragment PIE curves. The trend in the effective q values for the autoionizing resonances resolved in the PIE curves for HgCl_2^+ and its ionic fragments was found to be consistent with the previous observation of Eland *et al.*⁴⁹ the effective q value is largest for the weakest channel. This trend was not observed for the effective q values of autoionizing resonances appearing in the PIE curves of HgBr_2^+ , HgI_2^+ , and their ionic fragments. From the measured appearance energies of X^+ and HgX^+ , the bond dissociation energies of HgCl , HgBr , HgI , HgCl^+ , HgBr^+ and HgI^+ were calculated.

PIE curves for the CO_2 , N_2O , CO , N_2 and NO dimers and clusters were obtained using a cryogenic supersonic beam source. The stabilities of $(\text{CO}_2)_4^+$, $(\text{N}_2\text{O})_2^+$, $\text{NO}^+\cdot\text{N}_2\text{O}$, $(\text{CO})_3^+$ and $(\text{N}_2)_3^+$ were determined for the first time. In addition the solvation energies of NO^+ by two to five NO molecules were measured. A value of ~ 8.1 eV for the bulk IE of

nitric oxide was predicted. Evidence for the electronic predissociation of direct dissociation of CO_2 and N_2O Rydberg dimers was found by the comparison of the PIE curves of CO_2^+ , $(\text{CO}_2)_2^+$, N_2O^+ , and $(\text{N}_2\text{O})_2^+$. By analysis of the PIE curve of $(\text{NO})_2^+$, the IEs of $(\text{NO})_2$ to $\text{NO}^+(\hat{X}^1\Sigma^+, v=1)\cdot\text{NO}$ and $\text{NO}^+(\hat{X}^1\Sigma^+, v=2)\cdot\text{NO}$ were found, supporting the conclusion that the bonding of NO^+ in $\text{NO}^+\cdot\text{NO}$ is stronger than that of NO , but weaker than that of NO^+ .

The PIE curves of the O_3^+ , O_5^+ , and O_7^+ fragments [from $(\text{O}_2)_2^+$, $(\text{O}_2)_3^+$ and $(\text{O}_2)_4^+$, respectively] were measured and compared with the PIE curves of O^+ (from O_2), O_2^+ , $(\text{O}_2)_2^+$, $(\text{O}_2)_3^+$ and $(\text{O}_2)_4^+$. By using relative Franck-Condon factors for the $\hat{a}^4\Pi_u \leftarrow \hat{X}^3\Sigma_g^-$ transitions, the relative reaction probabilities for the ion-molecule half reaction



(where $m = 1, 2,$ and 3) were deduced. Although there is a marked dependence of the reaction probability on the vibrational energy of O_2 for $m = 1$, for reactions $m = 2$ and 3 the vibrational energy dependence was found to decrease substantially, indicating that the reaction probabilities for these reactions probably depend on solvation effects as well as on the structures of these excited cluster ions. This result demonstrates the potential of the molecular beam method for the study of solvation effects on chemical reactions in condensed phases.

REFERENCES

1. F. L. Mohler, Phys. Rev. 28, 46 (1926).
2. F. L. Mohler, P. D. Foote and R. L. Chenault, Phys. Rev. 27, 37 (1926).
3. K. Watanabe and E. C. Y. Inn, J. Opt. Soc. Am. 43, 32 (1953).
4. K. Watanabe, Phys. Rev. 91, 1155 (1953).
5. K. Watanabe, J. Chem. Phys. 22, 1564 (1954).
6. N. Wainfan, W. C. Walker and G. L. Weessler, J. Appl. Phys. 24, 1318 (1953).
7. N. Wainfan, W. C. Walker and G. L. Weessler, Phys. Rev. 99, 542 (1955).
8. H. Hurzeler, M. G. Inghram and J. D. Morrison, J. Chem. Phys. 27, 313 (1957).
9. H. Hurzeler, M. G. Inghram and J. D. Morrison, J. Chem. Phys. 28, 76 (1958).
10. J. Berkowitz, "Photoabsorption, Photoionization and Photoelectron Spectroscopy"; (Academic, New York, 1979).
11. P. M. Dehmer and W. A. Chupka, J. Chem. Phys. 65, 2243 (1976).
12. C.-Y. Ng, "Advances in Chemical Physics, Vol. 54 (Wiley, New York, 1982), Chap. 4, in press.
13. W. A. Chupka, in Chemical Spectroscopy and Photochemistry in the Vacuum-Ultraviolet, in "NAFO-Advanced Study Institutes series C.", edited by C. Sandorf, P. J. Ausloos, and M. B. Robin (Reidel, Boston, 1973), Vol. 8, p. 433.

14. W. A. Chupka, in "Ion-Molecule Reactions", Vol. 1, edited by J. L. Franklin (Plenum Press, New York, 1972), p. 33.
15. G. V. Marr, "Photoionization Process in Gases" (Academic Press, New York, 1967).
16. For a review of molecular beams, see J. B. Anderson, in "Molecular Beams and Low Density Gas Dynamics", edited by P. P. Wegener, (Marcel Dekker, New York, 1974), Chapter 1.
17. M. G. Liverman, S. M. Beck and R. E. Smalley, J. Chem. Phys. 70, 192 (1979).
18. C. Y. Ng, Ph.D. Thesis, the University of California, Berkeley, CA (1976).
19. C. Y. Ng, D. J. Trevor, B. H. Mahan and Y. T. Lee, J. Chem. Phys. 65, 4327 (1976).
20. C. Y. Ng, D. J. Trevor, B. H. Mahan and Y. T. Lee, J. Chem. Phys. 66, 3985 (1977).
21. C. Y. Ng, P. W. Tiedemann, B. H. Mahan and Y. T. Lee, J. Chem. Phys. 66, 3985 (1977).
22. C. Y. Ng, P. W. Tiedemann, B. H. Mahan and Y. T. Lee, J. Chem. Phys. 66, 5737 (1977).
23. C. Y. Trevor, P. W. Tiedemann, S. T. Ceyer, P. L. Kronebush, B. H. Mahan, and Y. T. Lee, J. Chem. Phys. 67, 4235 (1977).
24. W. M. Trott, N. C. Blais and E. A. Walters, J. Chem. Phys. 69, 3150 (1978).

25. W. M. Trott, N. C. Blais and E. A. Walters, *J. Chem. Phys.* 71, 1692 (1979).
26. P. M. Dehmer and E. D. Poliakoff, *Chem. Phys. Lett.* 77, 326 (1981).
27. P. M. Dehmer and S. T. Pratt, *J. Chem. Phys.* 76, 843 (1982).
28. P. M. Dehmer, *J. Chem. Phys.* 76, 1263 (1982).
29. S. T. Pratt and P. M. Dehmer, *J. Chem. Phys.* 76, 3433 (1982).
30. J. Berkowitz and W. A. Chupka, *J. Chem. Phys.* 45, 1287 (1966).
31. J. Berkowitz and C. Lifshitz, *J. Chem. Phys.* 48, 3246 (1968).
32. J. Berkowitz and T. A. Walter, *J. Chem. Phys.* 49, 1184 (1968).
33. J. Berkowitz and W. A. Chupka, *J. Chem. Phys.* 50, 4245 (1969).
34. J. Berkowitz, *J. Chem. Phys.* 50, 3503 (1969).
35. J. Berkowitz, *Adv. High Temp. Chem.* 3, 123 (1971).
36. O. F. Hagen, in "Molecular Beams and Low Density Gas Dynamics", edited by P. P. Wegener (Marcel Dekker, New York, 1974), Chapter 2.
37. M. Meot-Ner and F. H. Field, *J. Chem. Phys.* 66, 4527 (1977).
38. J. J. Solomon, M. Meot-Ner, and H. F. Field, *J. Am. Chem. Soc.* 96, 3727 (1974).
39. M. Meot-Ner and F. H. Field, *J. Chem. Phys.* 61, 3742 (1974).
40. Y. Ono, S. H. Linn, H. F. Prest, M. E. Gress, and C. Y. Ng, *J. Chem. Phys.* 73, 2523 (1980).
41. Y. Ono, E. A. Osuch, and C. Y. Ng, *J. Chem. Phys.* 73, 1645 (1981).
42. M. E. Gress, S. H. Linn, Y. Ono, H. F. Prest, and C. Y. Ng, *J. Chem. Phys.* 72, 4242 (1980).
43. Y. Ono and C. Y. Ng, Iowa State University, Ames, IA, to be published.

44. Y. Ono, Ph.D. Thesis, Iowa State University, Ames, IA (1982).
45. N. R. Daly, Rev. Sci. Instrum. 31, 264 (1960).
46. U. Fano, Nuovo Cimento 12, 156 (1935).
47. U. Fano, Phys. Rev. 124, 1866 (1961).
48. A. F. Starace, Phys. Rev. A 16, 231 (1977).
49. J. H. D. Eland, J. Berkowitz, and J. E. Monahan, J. Chem. Phys. 72, 253 (1980).
50. B. W. Shore, J. Opt. Soc. Am. 57, 881 (1967).
51. R. S. Mulliken, J. Am. Chem. Soc. 86, 3183 (1964).

ACKNOWLEDGMENTS

I would like to thank Dr. C. Y. Ng for his help and encouragement during my studies with him. I sincerely thank him for his concern for me as his student. His insight and personal expertise were invaluable to me as I was learning. I want to especially thank him for his patience. His example and inspiration have aided me in my own maturation in ways I could never adequately express.

I would further like to thank my fellow graduate students for their help and companionship. I would especially like to thank Chung-Lin Liao, Wen-Bih Tseng, Harry F. Prest, Yoshi Ono, and J. D. Shao for their contributions to my experiences, and for their help and discussions without which this work would have been extremely difficult.

Sincere thanks to the members of the many service groups at Ames Laboratory, and my special thanks to E. Ness, G. Steinbrenner and J. Sauke of the Chemistry Department Machine Shop.

To Roy and Evelyn Key, Rich and Sharon Joens, C. J. Quinn, Gaylon Decious, Wihden Aise, Engly Ioanis, Tom and Holly Ross, Scott and Susan Hurd, and many others I extend my thanks for making my life especially rich and meaningful. In the same vein I would like to single out Dave and Betty Evans and thank them for the special friendship, encouragement, and love they have given to me.

Lastly I would like to thank my wife Jane who has spent so many evenings and nights alone through the completion of my studies. Her faithful friendship, support, and love have been one of the major influences and strengths of my life.